T H E U N I V E R S I T Y O F M I C H I G A N

COLLEGE OF ENGINEERING
Department of Aerospace Engineering

Interim Technical Report

AUTOROTATING WINGS: AN EXPERIMENTAL INVESTIGATION

Edmund H. Smith

ORA Project 01954

under contract with:

DEPARTMENT OF THE ARMY
U. S. ARMY RESEARCH OFFICE--DURHAM
CONTRACT NO. DAHC0-4-68C-0027, PROJECT NO. 5590-E
DURHAM, NORTH CAROLINA

administered through:

OFFICE OF RESEARCH ADMINISTRATION ANN ARBOR

July 1970

ACKNOWLEDGEMENTS

The author would like to thank those people who made this research possible. In particular, he wishes to thank the chairman of his doctoral committee, Professor William W. Willmarth, and the other members of his committee. The financial support of the United States Army under AROD Contract DAHCO-4-68C-0027 is also gratefully acknowledged.

The author also wishes to thank Mr. Harold Hogan, Mr. Francis Donovan, Mr. Gerald Davenport and Mr. Cletus Iott for their technical assistance, and secretaries Mrs. Eunice Sherbrook and Mrs. Jacqueline Biggers for their work in preparing the manuscript. Finally, the author wishes to thank Dr. D. Coles for supplying the results of his unpublished work, which appear in part in this report.

TABLE OF CONTENTS

LIST OF FIGURES

NOMENCLATURE

a	vertical spacing of shed vortices, ft
A	aspect ratio
b	horizontal spacing of shed vortices, ft
c	wing chord, ft
C	wind tunnel cross section area corrected for boundary layer thickness, ft^2
C_D	drag coefficient
C_{D_a}	average drag coefficient
C_{D_p}	peak drag coefficient
C_{D_i}	induced drag coefficient
C_{D_o}	profile drag coefficient
C_{D_s}	drag coefficient for streamlined supports
$C_{D_{us}}$	drag coefficient for unstreamlined supports
C_L	lift coefficient
C_{L_a}	average lift coefficient
C_{L_p}	peak lift coefficient
C_M	pitching moment coefficient about c/4
C_p	power coefficient, $P/(1/2\rho V^3 s)$
C_T	torque coefficient, $T/1/2\rho V^2 sc)$
C_{L_α}	lift curve slope, per radian
$C_{L_{\alpha_o}}$	lift curve slope for infinte aspect ratio, per radian
d	fence location, see Fig. 32, ft
D	drag, lb.
D_a	average drag, lb.
e	span efficiency factor
F	resultant force on wing, lb.
h	fence height, ft

I	wing inertia, slug-ft^2
I^*	wing non - dimensional moment of inertia, $I/(\rho\pi c^5 A/32)$
ℓ	distance to center of pressure from mid-chord, ft
L	lift, lb.
L_a	average lift, lb.
m	mass, slugs
n	wing rotation rate, hz
P	power ft-lbs/sec
q	dynamic pressure, lb/ft^2
Re	Reynolds Number
s	wing area, ft^2
S	Strouhal number
t	time, sec
T	torque, ft-lbs
U	vortex velocity, relative to free stream, ft/sec
V	free stream velocity, ft/sec
w	wing rotation rate, rad/sec
W	weight, lb.
$\ddot{x}$	acceleration parallel to glide path, ft/sec^2
$\ddot{y}$	acceleration perpendicular to glide path ft/sec^2
α	angle of attack, degrees
$\dot{\alpha}$	instaneous angular velocity, rad/sec
$\ddot{\alpha}$	angular acceleration, rad/sec^2
$\ddot{\alpha}_p$	peak angular acceleration, rad/sec^2
Γ	circulation, ft^2/sec
ϵ	blocking factor
θ	instantaneous glide angle, degrees
λ	average glide angle, degrees

μ	viscosity, slugs/ft-sec
ρ	fluid density, slugs/ft^3
ϕ	angle of lift vector, measured from horizontal, degrees

ABSTRACT

The autorotation of a flat plate about its spanwise axis was experimentally studied. Most of the work was done with a wing mounted in The University of Michigan 5 x 7 ft low speed wind tunnel. The measurements consisted of the unsteady lift, drag, and angular acceleration and the wing rotation rate. The flow pattern was studied by means of smoke, tufts, and a small model in a water tunnel.

The flow pattern was very different from that over a static wing. The wing did not stall until it was nearly perpendicular to the free stream, and the flow did not reattach to the lower surface until the wing had rotated well past zero angle of attack.

The maximum and average lift, drag, and angular acceleration were measured for Reynolds numbers from 25,000 to 250,000. At Re = 240,000, the maximum lift coefficient was 4.50 with an average value of 2.20, while the maximum drag coefficient was 4.30 with an average value of 1.60. The angular acceleration was small; the wing rotated at an almost constant angular velocity. The nondimensional wing rotation rate was measured for Reynolds numbers from 1,300 to 280,000 and approached an asymptotic limit at 0.35 for sufficiently high Reynolds numbers.

The effect of applying driving and retarding torques to the wing was studied. As the rotation rate was increased above the free autorotation rate, the lift and drag increased. When the rotation rate was reduced by a retarding torque, they all decreased. The power developed by the rotating wing was considerably less than for a windmill of the same frontal area.

A variety of wing configurations were tested, including different airfoils and aspect ratios and spoilers mounted at various locations on the wing. However, except for spoilers that were so large that they prevented autorotation, none of these changes caused a major effect on the gross properties of the autorotation phenomenon.

Freely falling wings were also studied. For Reynolds numbers above 4,000 the average lift and drag coefficients were comparable to those observed in the fixed axis tests, and it appeared that the flow pattern was similar.

I. INTRODUCTION

Autorotation is the continuous rotation, without external power, of a body exposed to an air stream. Some familiar examples of this are the windmill and the cup anemometer.

The subject of this investigation is the autorotation of a wing about its spanwise axis when it is exposed to an air stream perpendicular to that axis. This phenomenon can occur either for a freely falling wing or for a wing autorotating about a fixed axis. An example of freely falling autorotation is the steady tumbling which results when a rectangular piece of stiff paper is dropped.

Recently, there has been interest in the autorotating wing problem for a number of reasons. It offers insight into the problem of dynamic stall, which is of interest in high performance helicopters and in compressor stall in turbine engines; considerable effort has been devoted to this problem recently by Ham[1], Moore[2], and others. Autorotation occurs in a number of other problems, such as the dropping of leaflets and the motion of panels separated from aircraft or spacecraft. Also, an autorotating wing could serve as a drag production device or as a steerable gliding parachute.

The autorotating wing problem was studied as early as 1897, when Ahlborn[3] observed the rotation of a falling plate. In 1909, Riabouchinsky[4] tested models with one, three and four vanes and found that

the greatest lift force existed for a model with one vane autorotating about its longest axis. In 1957, Crabtree[5] measured the average lift for both autorotating and mechanically driven wings, and also measured the rotation rate for autorotating wings with several different airfoils. Also in 1957, a group of students working under Coles[6] studied both fixed-axis and freely falling autorotation. For fixed-axis autorotation, they measured the rotation rate and average lift. For falling autorotating wings, they photographed the wing motion and measured the lift to drag ratio as a function of aspect ratio. In 1969, Sandia laboratories[7] measured the rotation rate for wings of various aspect ratio and for a disk. They also measured the average drag for some falling plates and studied autorotation at hypersonic speeds.

From this work, the order of magnitude of the average lift and drag coefficients and rotation rate were known, but there was still virtually nothing known about the flow field around the wing or the aerodynamic cause of autorotation. It was known that autorotation is caused by lift hysteresis resulting from unsteady aerodynamic effects, since steady flow theory would give equal positive and negative lift and hence, no net lift (assuming constant rotation speed).

Since it is impossible at present to compute the flow over an autorotating wing, an experimental investigation was required. The first step in understanding the phenomenon was to determine the flow pattern over the wing and its relation to the aerodynamic forces on the wing

(Sec. IV). In Section V, the aerodynamic forces on the wing are discussed, while the wing rotation rate is discussed in Section VI. In Section VII, the drag caused by the vortices shed from the wing is calculated by means of Von Karman's calculations for the drag of a bluff body that produces a vortex street. To gain a further understanding of the flow pattern and the cause of the aerodynamic forces, fences were mounted on the wing at various locations and the effects on the flow pattern, lift and rotation rate observed (Sec. VIII).

Several other topics were also investigated. In Section IX, the effect of a retarding torque on the wing is discussed. In Section X, the behavior of a freely falling wing is compared to the observations for fixed-axis autorotation and some reasons for the differences are given. Also, the boundaries of wing inertia and Reynolds number for which autorotation is possible are discussed. In Section XI, sphere and cylinder autorotation was investigated and found not to exist, at least at subcritical Reynolds numbers.

II. EXPERIMENTAL APPARATUS

A. INTRODUCTION

The experimental apparatus consisted of four systems. Small non-instrumented wings were mounted in The University of Michigan 2 x 2 ft low speed wind tunnel. A larger wing, instrumented for measurement of rotation rate, lift, drag, and angular acceleration, was mounted in The University of Michigan 5 x 7 ft low speed wind tunnel. The Wallis water tunnel was used for flow visualization with illuminated aluminum particles. In the drop tests, a variety of wings were dropped in various fluids and their fall observed and timed.

B. PRELIMINARY TESTS

1. Wind Tunnel Facility

The University of Michigan 2 x 2 ft low speed wind tunnel is of the open circuit type, with the fan located downstream of the test section. It has a contraction ratio of 16:1 and a test section length of 24 ft. A 10 hp Ward-Leonard drive system drives a four ft diameter fixed pitch fan. This provides a speed range of 4 to 68 ft/sec; for lower speeds, an air by-pass can be opened downstream of the test section. The turbulence level is 0.05% at 50 ft/sec free stream velocity.

2. Bearings

Two wing bearing systems were used (see Fig. 1 and 2). The first consisted of two ball bearings mounted on the upper and lower walls of the tunnel. These were suitable for both axial and radial loads, and carried the weight of the wing on the lower bearing. This arrangement proved unsatisfactory because the wings flexed enough to cause binding in the bearings. To cure this, the upper bearing was replaced with a loose fitting metal collar which retained the upper end of the wing shaft. This relatively crude arrangement worked satisfactorally for preliminary tests, but was not used in the final data.

The second bearing system consisted of two needles mounted on the wing axis, with the lower one running in a conical hole in a piece of steel and the tip of the upper one running in a 1/16 in. I. D. metal collar. When this system was adjusted so that only about 0. 05 in. of the upper needle was in the collar, it gave very low friction, and this system was used for all of the final data taken in the 2 x 2 ft tunnel. For Reynolds numbers below 1500, a different mount was used to support a smaller wing. This had a similar needle bearing system (see Fig. 3). It should be noted that the upper bearing did not press the lower needle into the hole in either system; it was held in the hole only by the weight of the wing. At a sufficiently high speed, the needle

would jump out of the hole, but this did not happen for the desired range of speeds. If the system was adjusted so that the needles were clamped in place, the friction was considerably increased.

3. Wings

The wings were from 0.02 to 0.04c thick with aspect ratios of 6.4 and 1.33c diameter tip plates. All of the wings had square edges 0.02c thick, except for the tests for Reynolds numbers below 1500, in which they were 0.031c thick. All of the wings were built of sheet balsa with spruce or metal center spars except for the wing used for Reynolds numbers below 1500, which had no spar, and a wing used for I* below four, which was built of balsa strips and covered with light tissue. The moments of inertia of the wings were determined by weighing each part as the wings were built and calculating its moment of inertia, then summing up the inertia of the parts to get the moment of inertia of the complete wing.

4. Instrumentation

The free stream velocity was measured with a pitot static tube and a plastic propeller of the type furnished with small rubber powered model airplanes. The propeller was calibrated against the pitot static tube for speeds greater than five ft/sec by measuring its rotation rate with a strobe lamp*, which had been calibrated against a

---

*General Radio Corporation Strobotac Model 1531-A.

digital counter*. For lower speeds, the propeller was calibrated by carrying it at a known speed and counting the revolutions, with the propeller on a 36 in. shaft to reduce interference effects from the person carrying it.

Neither of these arrangements was very satisfactory. The manometer bank used for the pitot static tube was not too sensitive at low speeds. The calibration obtained by carrying the propeller was not too good, since there was some flow interference from the person carrying it and it was impossible to walk at a perfectly steady speed. Hence, the propeller was later re-calibrated against the propeller anemometer described below in Part 7 of Section C, and this calibration was used in all of the final data.

The rotation rate of the wing was measured at low speeds by counting its revolutions and timing them with a stop watch. At higher speeds, the strobe lamp described above was used.

C. INSTRUMENTED WING

The instrumented wing was used for most of the data, including all of the fixed-axis lift, drag, and angular acceleration data. This was installed in The University of Michigan 5 x 7 ft low speed wind tunnel.

---

*Beckman Model 7360A Universal Eput and Timer.

1. Wind Tunnel Facility

The University of Michigan low speed wind tunnel is a closed circuit, single return tunnel. It has a 5 x 7 ft test section with the corners filleted 8 in. up each wall to produce an octagonal cross section. It has a contraction ratio of 15:1 and the test section is 25 ft long. The tunnel is powered by an 1100 hp Ward-Leonard drive system, which drives a 12. 6 ft diameter fixed pitch fan. The speed range is from about one to 300 ft/sec, and the turbulence level is about 0. 03% in the current configuration with four settling chamber screens.

2. Configuration Tests

A series of preliminary tests to determine the best wing configuration were run in the 5 x 7 ft tunnel. Three variables, airfoil, aspect ratio, and tip plate geometery, were studied. For these tests, the wings were mounted 4. 6c from the tunnel wall, and the needle bearing system described in Part 2 of Section A was used (see Fig. 4).

For the airfoil tests, the wings were built in the manner of a model airplane wing and covered with sheet balsa. All were of 20 in. span with aspect ratios of 6. 4 and 1. 33c diameter tip plates. For the aspect ratio tests, the wings were built of sheet balsa with spruce center spars in all except the wing with an aspect ratio of 1. 33. They were all 0. 04c thick and had 1. 30c diameter tip plates. The tip plate

tests were performed on the wing with an aspect ratio of 2. 60; a low aspect ratio was chosen because the Strouhal number would be more sensitive to changes in the tip plates.

3. Wing Mounting Frame

The bearings were mounted on a heavy steel frame, which was bolted to the wind tunnel floor (see Fig. 5). The base of the frame consisted of two 4 x 1. 68 in. steel channel side rails joined by two 4 x 2. 66 in. steel I-beams, forming a shape like the letter "H". The vertical supports that carried the bearings were one inch thick steel plates bolted to the side channels. However, the wing was mounted too close to the tunnel wall for minimum wall effects, so the side plates were extended with steel channel. This was planned as a temporary solution only, but it proved satisfactory and was used throughout the tests. To improve the flow in the wind tunnel, the base was streamlined with a piece of cardboard which faired the cross braces into the floor.

4. Air Bearing System

The first wing bearings were a pair of spherical air bearings (see Fig. 6). This system was chosen, despite its complexity and high cost, because it gave very low friction and freedom from vibration. The spherical bearings were more difficult to make than cylindrical bearings, but they were far simpler to install and use, since

they were self-aligning and required only an axial adjustment. Flexing of the wing or mounting frame would not interfere with their operation unless it appreciably changed the axial position of the outer bearings. These bearings were fabricated in The University of Michigan instrument shop and the design was based on work by Laub[8].

The bearings consisted of two basic parts: the inner bearing, which was bolted to the wing spar and whose surface was the outer portion of a sphere of 4.000 in. diameter, and the outer bearing, which was bolted to the wing supporting frame, and whose inner surface was a spherical surface of 4.004 in. diameter. The outer bearing contained a plenum chamber from which three rows of 48 1/32 in. diameter holes were drilled to the spherical surface. The desired hole size was 0.004 in., but this size hole could not be drilled through the aluminum at a reasonable cost. Therefore, the inner wall of the plenum chamber was covered with 0.001 in. shim brass attached with double surfaced tape* and the holes were punched into this with 0.004 in. diameter music wire. The bearings were connected to the building air supply, which maintained the plenum chambers at about 70 psi.

Unfortunately, this system did not work. When the plenum chambers were pressurized sufficiently to support the inner bearings, they oscillated rapidly in the outer bearings, hitting them and emitting

---

*Scotch Double Stick Tape, 3M Company.

a loud shrieking sound. A variety of orifice sizes were tried with no improvement. A study of the literature[9, 10] revealed that others had encountered this problem, and that it was caused by a pneumatic effect in the air in the pockets below the small orifices. The problem was that the air in the pockets below the foil took a finite time to change in pressure when the bearing clearance changed at that point. Hence, the bearing tended to continue to displace so that it was appreciably displaced when the pressure changes finally stopped it. However, then the pressure would continue to fall on the side with large clearance and to rise on the side with small clearance and the bearing would be thrust back even more violently, and a resonance would result, making the bearing inoperative and damaging its surfaces.

To correct this, the shim brass was removed and the outer rows of holes were temporarily plugged with clay and the bearings were tested with various numbers of the holes open. This eliminated the rapid oscillation, but if more than 24 holes were open, a low frequency oscillation occurred. Hence, all but every other hole in the center row were plugged with bathtub caulk*. This modification reduced the bearing efficiency, since the pressure was less uniform in the gap than if

---

*Dow Corning Silicone Rubber Bathtub Caulk, White.

the larger number of holes could have been used. However, the bearings still supported 35 lb in addition to the weight of the bearings and wing spar at 59 psi line pressure.

After this problem was solved, the bearing system proved surprisingly trouble free, even though the air supply was somewhat contaminated with oil, and only a crude filter was used. However, the load carrying ability of the bearings only allowed testing up to a Reynolds number of 170,000, so a set of mechanical bearings was used for higher speeds.

5. Mechanical Bearing System

Fafnir DSP-10 spherical ball bearings were chosen because they were self-aligning in the same manner as the air bearings (see Fig. 7). They were mounted in housings that bolted to the same supports used for the air bearings. The wing was fitted with steel shafts that mounted in the same holes used for the air bearings. One shaft had two snap rings to keep the wing in position; the other was free to slide in its bearing, so no alignment was required after assembly.

As supplied, the bearings had grease seals, which were thin rubber disks fixed to the outer race and sliding on the inner race, and they were lubricated with a fairly heavy grease. Initial tests showed prohibitive bearing friction, so the grease seals were removed and the bearings cleaned with tri-chloroethylene. This greatly reduced

friction, but the unlubricated balls clicked audibly and the vibration caused noise in the strain gauge signal for lift or drag. To correct this, the bearings were lubricated with a light oil, which eliminated the noise and caused only a slight increase in friction. However, the friction still appreciably effected the experimental results.

6. Wing

The wing was constructed of balsa and spruce around a steel center spar (see Fig. 8). It had an aspect ratio of three with a one foot chord and a 15% thick elliptical airfoil, and 1.33c diameter tip plates. The one foot chord was a compromise, since a larger chord would give a higher maximum Reynolds number, but also a greater flow blockage. An aspect ratio of three was chosen because a lower aspect ratio gives less flow blockage for a given chord, and the aspect ratio tests (Fig. 29) showed that the Strouhal number was nearly independent of aspect ratio for aspect ratios greater than 2.60. The airfoil was a 15% thick ellipse, symmetric both fore and aft and with respect to the chord line. It was chosen because it provided adequate thickness for structure and was a well known shape.

The structure was designed to have a low moment of inertia so that the angular acceleration would be as large as possible. Since structure near the axis has a low moment of inertia, the wing was built around a central steel tubular spar of 1.625 in. O.D. and

0.065 in. wall. Wing bending was negligible, since the calculated deflection of the spar was only 0.008 in. at the maximum load. The remainder of the wing was supported by three steel ribs brazed to the spar at each tip and the mid-span; a spruce leading edge was bolted to these. To support the balsa wing skin, balsa ribs were glued to the spar and leading edge with epoxy cement. The leading edges were balsa, hollowed out to reduce weight. The tip plates were constructed of 1/8 in. sheet balsa.

The calculated moment of inertia including the rotating part of the air bearings was 0.00584 slug-ft^2. An experimental check was performed by hanging the wing on a metal rod as a torsional pendulum and timing its oscillations; this yielded a moment of inertia of 0.00583 slug-ft^2.

7. Instrumentation

Lift and drag were measured by strain gauges mounted on a 0.8 in. wide flexure on one of the bearing supports. L. T. Bean BAE-13-125AA-120 strain gauges were attached with L. T. Bean BAP-1 cement and protected with L. T. Bean Gage-Coat No. 4 after wiring. The system was sensitive to bending only, and measured half the drag when mounted vertically and half the lift when mounted horizontally; the readings were doubled to get the full lift and drag. The natural frequency of the flexure was 200 hz with the wing installed, while the maximum frequency of the lift or drag cycle was 26 hz. Therefore,

no corrections were needed for phase shift or amplitude in the lift and drag data except for a few runs when the amplifier filter was set at 100 hz (see below).

The circuit was a Wheatstone bridge circuit with a balancing network added (see Fig. 9). A dual power supply*, with the center tap grounded, provided eight volts across the bridge. The output was amplified with a gain of 1000 by a differential amplifier** and then displayed on an oscilloscope†. The amplifier had an adjustable low pass filter; the cut-off frequency was set at 100 hz, slightly above the frequency at which phase shift and attenutation were negligible.

At lift cycle frequencies (twice the wing rotation frequency) of about 20 hz, the strain gauge signal became badly distorted. This was traced to a natural frequency of the vertical member of the wing supporting frame of about 20 hz. To correct this, a diagonal brace was added to the frame (see Fig. 5). However, at a lift cycle frequency of 26 hz, the signal again became distorted because the wind tunnel walls were vibrating and exciting the flexure. Since it was also felt that the structural limits of the wing were being approached, this was accepted as the limit on running speed, and all data for which

---

* Trygon Dual Lab Supply Model DL 40-1.

** Dana Model 3520 D. C. Amplifier.

† Tektronix Model 544 Oscilloscope or Model 502A Dual Beam Oscilloscope.

the signal was seriously distorted were discarded. For the last few runs, the amplifier low pass filter was set at 100 hz in order to reduce the error caused by the excitation of the flexure; the results were then corrected for phase shift and attenuation. The corrections were based on a calibration made with a sine wave, which closely approximated the lift and acceleration signals and was a fair approximation to the drag.

The angular acceleration was measured with an optical torquemeter* fitted with a flywheel to convert it into an angular accelerometer. The torquemeter had two slotted disks on a shaft with a necked down portion in the shaft between them. Two lamps were mounted at one end and two photocells at the other. Hence, as the shaft was twisted, the amount of light hitting the photocell was increased or decreased, so that the output of the photocell varied in proportion to the amount of shaft twist, which was proportional to the torque. The main advantage of this system was that no slip rings were needed and the unit caused a very small retarding torque on the wing.

The shaft stiffness was fairly low, but it was possible to get a natural frequency of five times the lift cycle frequency. Three flywheels were built, so that the flywheel size could be increased for lower speeds where a lower natural frequency was acceptable, to take full advantage of the available sensitivity. The torquemeter output

---

*Vibrac Model TQ-32 Torque Transducer, Vibrac Corporation.

was amplified with a gain of 200 or 1000 using the same type of amplifier used for the strain gauges and displayed on the same oscilloscope. The amplifier filter was set at 100 hz to minimize distortion of the signal owing to excitation of the relatively low natural frequency of the unit. The data were corrected for phase shift and attenuation caused by the filter using the calibration procedure described above. The data were also corrected for the phase shift and attenuation caused by the low natural frequency of the torquemeter, but these corrections were small. To further improve the signal quality, it was fed into a Waveform Eductor*, which used a bank of capacitors to average the signal over many cycles. This improved the signal somewhat, but was not used for all of the data.

When the torquemeter was first mounted, a large extraneous signal occurred because of bending of the torquemeter shaft. This was caused by a distortion in the wing spar, which caused a run-out in the inner bearing. Since the torquemeter was fixed in its mount, this bent the torquemeter shaft as the wing rotated. To correct the problem, the alignment system shown in Fig. 6 was installed. This system consisted of two disks, with the outer one holding the torquemeter shaft. The first disk was bolted to the bearing with oversize holes so that the disk could be centered on the axis of rotation of the wing. The second disk was bolted to this with three bolts. There was

---

*Princeton Applied Research Waveform Eductor, Model TDH-9.

a set screw next to each bolt, so that by loosening the bolts and adjusting the set screws, the axis of the hole for the shaft in the fitting could be made parallel to the axis of rotation of the wing. After careful adjustment, the extraneous signal was nearly eliminated. Two of these alignment systems were built; the other one was used to mount the torque application pulley (see Part 9 of this section).

The wing rotation rate was measured with a photocell system in which a six volt flashlight bulb was mounted on one side of one of the tip plates and a photocell on the other. One or more slots were cut in the plate and the photocell gave a pulse as each slot passed it. The pulsating signal was amplified by a single F. E. T. transistor amplifier. This pulsating signal was fed into the digital counter described in Part 4 of Section B and the counter reading gave the wing rotation rate. The signal was also displayed on the oscilloscope to provide a position reference for the lift, drag, and angular acceleration data, and was used to trigger the Waveform Eductor.

The free stream velocity was measured with the pitot-static tube permanently installed in the wind tunnel and also with a propeller anemometer*. This consisted of a 9 in. diameter styrofoam propeller driving a small D. C. motor, which generated a voltage that was

---

*Gill Propeller Anemometer, Model 27100, R. M. Young, Co.

read on a D. C. voltmeter*. The main advantage of the anemometer was that it could be read more accurately than the pitot tube, especially at low speeds.

8. Flow Visualization Equipment

The flow pattern was investigated in the 5 x 7 ft tunnel with tufts attached to the wing surface and with titanium oxide smoke. The tufts furnished information about the flow pattern for higher Reynolds numbers and were viewed by "stopping" the wing with the strobe lamp described in Part 4 of Section B. The titanium oxide smoke could only be used at very low free stream velocities, but it gave a better view of the flow. It was released from a rod covered with liquid titanium tetrachloride** mounted in front of the wing and also from a liquid film of titanium tetrachloride on the wing surface.

9. Torque Application Equipment

Retarding and driving torques were applied to the wing by attaching a pulley to the end of one of the rotating parts of the air bearings and having the wing raise or lower a weight on a nylon thread wrapped around the pulley. To give more running time, the weight was suspended below the wind tunnel floor with the thread passing through a

---

* Simpson Volt-Ohm Milliammeter, Model 263.

** This substance decomposes into a dense white smoke that is a mixture of titanium oxide and Hydrogen Chloride upon exposure to moist air.

hole in the floor. However, the run time was still fairly short, and the system was practical only for Reynolds numbers below 100,000. A tubular cardboard shield was placed over the thread to prevent the air stream from deflecting it and causing it to hit the edge of the hole in the floor.

10. Low Inertia Wing

Some very light wings were built to determine the minimum moment of inertia for fixed-axis autorotation. These had an aspect ratio of three and had a nine inch wing span. They had 15% thick elliptical airfoils, although the airfoil was not as accurate as on the other wings. They had full depth balsa spars at the mid-chord, with the rest of the structure built up of 1/32 in. square balsa. They were covered with microfilm* and ran on the needle bearings described in Part 2 of Section A.

D. WATER TUNNEL

1. Water Tunnel Facility

Most of the flow visualization work was done in the Wallis water tunnel (see Fig. 10). This is a small closed circuit single return tunnel. It has a five inch square test section, 13 in. long and a 2.5:1 contraction ratio, with four settling chamber screens. It is

---

*Microdyne Formula B, Microdyne Precision Products.

powered by a 1/10 hp constant speed electric motor driving a variable pitch fan, and has a speed range of 0. 25 to 1. 0 ft/sec.

The flow pattern is made visible by a plane of light which illuminates aluminum particles suspended in the water. The plane of light is parallel to the flow direction and perpendicular to the wing so that it illuminates a two-dimensional plane in the flow over the wing.

2. Model

A wing with a four inch span and aspect ratio of two was built of 1/16 in. thick Plexiglas. It had 2. 67 in. diameter Plexiglas tip plates, but one was removed because it interfered with the photography. Since bearing friction would have been prohibitive in water (to get an adequate I*, a very heavy wing would be required), the wing did not actually autorotate, but was driven by an electric motor. Power to the motor was supplied by an auto transformer to allow variation of the rotation rate.

3. Photographic Equipment

The still photographs were taken with a Polaroid camera* using ASA speed 3000 film** at f/4. 7 lens setting and 1/60 sec shutter speed.

---

* Polaroid Land Camera, Model 110A.

**Polaroid Roll Film, Type 47.

A movie was taken by G. Davenport using a conventional movie camera* and ASA speed 160 film**.

E. WALL CORRECTIONS

Wind tunnel tests must be corrected for the finite size of the test section. These corrections include an effective increase in the dynamic pressure caused by the reduction in test section area owing to the blockage of the model and wake, effects from pressure gradients that may exist in the wind tunnel, and changes in the streamline curvature and downwash.

The blockage correction was by far the largest correction for the autorotation tests. This correction was calculated by the method of Maskell for bluff bodies[11]. His method uses the momentum equation to calculate the change in the dynamic pressure for a given blockage. The equation proposed by Maskell is

$$\frac{\Delta q}{q} = 1/2(s/C)(C_{D_s} + C_{D_o}) + \epsilon(s/C)(C_D - C_{D_i} - C_{D_o}) \quad ,$$

where ϵ is a function of aspect ratio, which Maskell determined experimentally. Since some parts of the supports were unstreamlined, it was necessary to add another term ot the right hand side of the

---

* Kodak Cine Special with f/1. 4 lens.

** Kodak Tri-X 16 mm Reversal Film Type 7278.

equation, $\epsilon(s/C)(C_{D_{us}})$ to account for them. It should be noted that C_{D_s} and $C_{D_{us}}$ are based on the wing area, not the frontal area of the component in question. The drag coefficients for the supports were obtained from published data [12] and corrected to the reference area s. The parasite drag was also taken from published data[12]. The blockage caused by the supporting structure was about 28% of the total blockage. The induced drag also had to be estimated, and it was assumed that the steady state formula $C_{D_i} = C_L^2/\pi Ae$ could be used, with C_L^2 being averaged over a cycle. This probably caused some error in the results, since the use of the steady state formula was certainly an approximation, and the calculated induced drag was from 23 to 48% of the total wing drag. Also, Maskell's method was derived for a steady wake, while the wing drag fluctuated as the wing rotated. Hence, the method had to be assumed valid for the fluctuating wake of the wing, using the average drag coefficient, C_D, in the equation. This assumption was probably fairly good, since the wing rotated rapidly enough that the irregularities in the wake were quite closely spaced. Also, they were observed in the smoke tests to quickly merge into a wake of relatively uniform size with rather random eddies. The resulting value of $\Delta q/q$ in the 5 x 7 ft tunnel increased from 0.317 at Re = 16,300 to 0.326 at Re = 250,000; the corresponding values of $\Delta V/V$ increased from 0.148 to 0.155. In the 2 x 2 ft tunnel, $\Delta V/V$ was 0.09 for the 20 in. span wings.

The downwash and streamline curvature corrections were very small compared to the blockage corrections, and the buoyancy corrections were negligible. These corrections were made only for the 5 x 7 ft tunnel, since they did not effect Strouhal number data, which was the only data taken in the 2 x 2 ft tunnel. Pope and Harper[13] give the correction for streamline curvature as

$$\Delta C_L = -\tau_2 \delta (s/C)(C_L)(C_{L_\alpha}) \quad ,$$

where C_{L_α} is the lift curve slope and τ_2 and δ are given for various conditions. The lift curve slope was calculated from the steady state formula:

$$C_{L_\alpha} = C_{L_{\alpha_o}} / (1 + C_{L_{\alpha_o}} / A)$$

From thin airfoil theory, $C_{L_{\alpha_o}}$ was assumed to equal 2π. This resulted in the correction $\Delta C_L = 0.0038\, C_L$. Pope and Harper[13] also give the formula

$$\Delta C_D = \delta (s/C) C_L^{\,2}$$

for the downwash correction. This yielded $\Delta C_D = 0.0107\, C_L^{\,2}$. These corrections were assumed valid for both the peak and average lift and drag, with the peak and average values of C_L and $C_L^{\,2}$ used.

Another correction was needed to account for drag on the fixed outer part of the bearing unit, which was exposed to the free stream. This gave the correction $\Delta C_D = 0.0065$, based on s. The drag of the tip plates was included in the wing drag data and was not corrected for.

The wall corrections were checked in two ways. The wing was stopped perpendicular to the flow and the drag was measured, corrected, and compared with data in Hoerner[12]. The measured drag coefficient was 1.29, compared with 1.21 from Hoerner, quite good agreement. This suggests that the correction for the drag of the wing supporting frame is fairly accurate, but it proves nothing about the assumptions used for the unsteady flow. The second check was furnished by the Strouhal number tests. In the 5 x 7 ft tunnel, the small wings had velocity corrections of only about 1%, compared to about 15% for the large wing, and both sets of data converged well for Reynolds numbers below the supposed transition range (see Fig. 24).

In summary, the wall corrections were larger than desirable and required some assumptions that could cause appreciable errors. However, in view of the checks described above, it seems probable that they are at least moderately accurate.

F. DROP TESTS

Two types of drop tests were performed. In the first, some of the balsa wings described in Part 2 of Section C were dropped in air

in order to compare data for fixed-axis and freely falling autorotation. In the second, wings were dropped into a variety of fluids to determine the range of Reynolds number and I* for different types of motion.

The second series of tests were performed in air, water and a water-glycerol mixture with 83% glycerol. The water tests were done in a 18 x 15 in. basin with 12 in. depth for wings with no more than 4 in. span and in The University of Michigan ship model towing tank, which is 20 x 360 ft and had an 82 in. depth at the time of the tests. The water-glycerol tests were done in the towing channel facility built by Roos[14], which is 2 x 32 ft with a 2 ft depth. For the air and water tests, μ and ρ were determined by measuring the temperature and using published data[15]. For the water-glycerol mixture, the temperature was measured and an experimentally obtained table prepared by Roos[16] was used.

The wings were all smooth, square edged, flat plates with aspect ratios of 2.5 except as noted in Fig. 46. None of the models had tip plates. For the water and water-glycerol tests, the wings were made of aluminum, brass and lead with chords of 0.4 to 7.35 in. The wings were less than 0.032c thick for I* below 0.10, but for higher I*, the thickness was as great at 0.1c, and for one test, at I* = 2.04 and Re = 94.6, it was 0.30c. For the drops in air, the wings were made

of various weights of paper with chords of 0.08 to 0.3 in. They were less than 0.032c thick, except for one test, at $I^* = 46$ and $Re = 115$, for which the wing was 0.065c thick.

The only instrumentation used in the drop tests was a stop watch for timing the descent of the wings and a thermometer for measuring the fluid temperature. For all of the non-autorotating wings, the Reynolds numbers and Strouhal numbers were calculated using the average vertical velocity, that is, the vertical distance fallen divided by the time required to fall. For tests in which the wings autorotated with an appreciable glide angle, this angle was estimated, and the average velocity along this path was used; it was easily calculated from the average vertical velocity and glide angle.

G. SPHERE AND CYLINDER AUTOROTATION

The sphere and cylinder autorotation tests were performed in the 5 x 7 ft tunnel. The flow velocity was measured with the propeller anemometer described in Part 7 of Section C.

1. Models

Two spheres were used, a four inch diameter styrofoam sphere and a 1.50 in. diameter ping-pong ball. The styrofoam sphere had a moderately rough surface, since the styrofoam had an average cell size of about 0.05 in. diameter, and no finish was applied. It was carefully centered and had less than 0.03 in. run out. The ping-pong

ball had a very smooth surface with no noticeable seams, and was also carefully centered. The cylinder was a cardboard tube of two inch diameter and 16 in. length, with four inch diameter tip plates on each end. It was covered with paper to give a smooth surface, and had less than 0. 02 in. run out.

2. Bearings

Both the large sphere and cylinder were mounted on the needle bearings described in Part 2 of Section A. The ping-pong ball was mounted on a slightly different arrangement, in which the needles were fixed and ran in small depressions in the surface of the ball.

III. EXPERIMENTAL TECHNIQUE

A. PRELIMINARY TESTS

The tunnel was started and set at a low speed. Then, the wing was started by reaching through an open panel and spinning it by hand. This was necessary because the wing was statically stable when it was perpendicular to the flow (see Part A of Chapter IV). The panel was then closed, and the tunnel set at the desired speed. After allowing one to two minutes for the speed to become steady, the rotation rate of the wing and propeller were read and the pitot-static tube was read if it was in use.

B. INSTRUMENTED WING

Although the apparatus was complex, operation was simple. The electronic equipment was turned on and allowed at least a half hour to warm up. Then, the strain gauges were calibrated by hanging a known weight from the flexure. The torquemeter was set to read zero at zero torque, which automatically adjusted the calibration. Then, the air supply to the air bearings was turned on if they were in use, and the wind tunnel started at a low speed. The wing was started by hand and the wind tunnel door closed, and the speed adjusted as desired. After waiting one or two minutes for the speed to become steady, the data, except for the Strouhal number data, were either read off the face of the oscilloscope and recorded, or photographed with a

Polaroid camera. The Strouhal number data were read from the digital counter. The flow velocity was read from the anemometer meter both before and after the other data were taken; if it changed appreciably during the run, the data were discarded and the run repeated.

C. WATER TUNNEL

First, the fan pitch was adjusted to give the desired flow velocity and the water temperature was measured. Then, new aluminum particles were added to replace those that had settled out of the flow*. The tunnel lights were turned on, the motor driving the wing started and the transformer adjusted to give the desired rotation rate. Then, all room lights were turned out and the tunnel motor started, first forward, then reverse, then forward again to help stir up the aluminum particles. After allowing about ten seconds for the flow to become steady, the camera was triggered.

D. DROP TESTS

The wings were released from a height of 6 to 14 ft with as close to the steady state rotation speed as possible. Their descent was timed with a stop watch and the distance along the floor measured.

---

*The aluminum particles were mixed with glycerine to facilitate adding them to the water; the change in viscosity caused by the small amount of glycerine was neglected.

To minimize errors from the launch, a number of drops were made, and the results averaged. The tests were made on days in which there were no appreciable drafts in the room used; this was checked by dropping one of the microfilm wings and observing its fall.

IV. THE AUTOROTATION PHENOMENON

A. INTRODUCTION

The unsteady flow pattern observed during autorotation is extremely complicated. It can perhaps be more readily understood if one first considers the quasi-steady flow over a slowly rotating airfoil. The differences between the steady and unsteady flow will then become apparent, and the unsteady aerodynamic phenomena responsible for autorotation will be revealed.

Let us consider a slowly rotating airfoil, with fore and aft symmetry, that rotates clockwise about its mid-chord point from zero angle of attack through one hundred and eighty degrees (180^{o}), at which point the former leading edge is now the trailing edge and the cycle repeats itself. At zero angle of attack, no lift force, no torque about the mid-chord and only a small drag force are developed. As the angle of attack increases slowly, a lift force, which acts at the quarter chord point, is developed; this also produces a clockwise torque about the axis of rotation. The profile drag increases slightly. This situation remains essentially unchanged until the flow over the upper surface begins to separate, and stall begins. During the stalling process the lift reaches a maximum and then decreases and eventually vanishes when the airfoil chord is normal to the free stream. The torque about the axis of rotation also reaches a maximum, near

the point of maximum lift, and decreases monotonically to zero when the airfoil chord is normal to the free stream. During a slow rotation from $\alpha = 90^{o}$ to $\alpha = 180^{o}$ the above process is repeated in reverse order and with reversed sign on the moment and lift.

It is apparent that the quasi-steady sequence of events described above (in which the average torque during one cycle is zero) could not result in autorotation because rotational friction and aerodynamic damping would remove rotational energy from the rotating wing. The fact that autorotation does occur means that the aerodynamic forces on the airfoil are modified by unsteady flow effects. In practice we have observed that an airfoil released from rest at an angular position in which the flow was stalled will eventually (after a number of oscillations) come to rest in a statically stable position with the airfoil chord normal to the free stream. If the airfoil is released from rest when the flow is not stalled (at a small angle of attack) autorotation usually occurs and the direction of rotation corresponds to the initial direction of rotation when the airfoil was released.

It is apparent from this description of the observed behavior that the retarding moment produced by aerodynamic damping and friction is overcome by the rotation energy gained before and after

stall when the lift is still large. If the airfoil moment of inertia was not large enough to store angular momentum sufficient to overcome the retarding moment of friction, aerodynamic damping, and the stabilizing moment near $\alpha = 90^{o}$, autorotation was not observed.

The requirements for autorotation are therefore low bearing friction, large enough moment of inertia to store angular momentum sufficient to overcome damping and friction, and the proper initial conditions (i. e., angular position or velocity).

As explained above, the wing could not autorotate if the flow behaved as in the quasi-static case. Therefore, the flow pattern must differ from the static case in such a manner that the wing can gain energy during the part of the cycle when the lift is large. This was found to occur; the wing stalled much later than in the static case and the flow reattached later to the lower surface. Thus, the positive lift and moment produced by lift were increased and the negative lift and retarding moment were reduced. This caused the wing to further increase its angular velocity until a steady speed was reached, at which the average torque was reduced to zero by aerodynamic damping effects. The cause of the later stall is that the boundary layer on the upper (suction) surface of the airfoil takes time to thicken and separate when the angle of attack is rapidly increasing, so that the wing stalls at a higher angle of attack. Likewise, the flow takes time

to reattach to the lower surface, so the wing is well below the static stall angle before the flow is fully attached. The cause of the aerodynamic damping that ultimately limits the angular velocity of the autorotating airfoil is not fully understood. It was observed that the lift vector acted much closer to the mid-chord when the lift was large, and far ahead of it during a large part of the time when the wing was stalled. (See Fig. 13 and 14 and Part B of this chapter.)

B. FLOW PATTERN

The flow pattern was studied by means of tufts, smoke, and illuminated aluminum particles in the water tunnel. Although no local velocity data were taken, the flow pattern was quite clear. Figure 11 shows it for various angles of attack. Each sketch shows the instantaneous streamlines for the given angle of attack. *

The lift and drag forces were also measured as a function of angle of attack, with strain gauges. Since the autorotation problem involves an unsteady flow field, the lift is not directly proportional to the circulation. The usual formula $L = \rho V\Gamma$ is derived for potential flow with the unsteady term neglected in the equations of motion. However, it seems probable that the lift and circulation are still related in that when the circulation is large, the lift is large and when

---

* The streamlines very near the body where viscous effects dominate and the no slip condition is important were not studied.

the circulation is small, the lift is small. Comparison of the lift data and the flow pattern confirmed this, as the circulation was clearly large when the lift was maximum and small when it was minimum (Fig. 12).

The description of the flow pattern is begun at the minimum lift point. At $\alpha = -80^{o}$, the flow field had separated over the rear of the wing, and the forward flow was almost stagnation flow, probably with a small net counter-clockwise circulation (for flow from left to right with clockwise wing rotation). The lift was slightly negative and the drag was fairly high. As the wing rotated, the forward stagnation point moved toward the advancing edge, with the flow becoming faster over the retreating edge and counter-clockwise vorticity being shed from the advancing edge. As this happened, the negative lift vanished and it became positive as the clockwise circulation built up. The drag decreased as the flow became faster over the retreating edge and the pressure decreased there. At $\alpha = -50^{o}$, the drag vanished and then became negative, while the lift continued to increase. The drag reached its negative peak at about $\alpha = -30^{o}$, and then decreased and vanished again at $\alpha = -10^{o}$. At $\alpha = 20^{o}$, the flow finally began to attach to the lower surface, with the stagnation point slightly behind the leading edge. The lift leveled off as the shedding of counter-clockwise vorticity stopped. As the angle of attack continued to increase, the flow over the upper surface remained attached, while the stagnation point moved away from the leading edge on the lower surface. The drag increased rapidly, since the resultant

force on the wing remained approximately constant and its rearward component became much larger. At about 80^{o} angle of attack, depending on the Reynolds number, the flow began to separate and a large clockwise eddy began to form at the leading edge and a smaller counter-clockwise eddy at the trailing edge. There was probably an unsteady vortex-induced loading just as they were shed, which caused the sharp peak in the drag that was observed*. As these vortices, which contained the vorticity which had been producing part of the lift when it resided in the boundary layer, grew and were shed, the lift and drag decreased rapidly, and at about $\alpha = 80^{o}$, the lift again became slightly negative, to complete the cycle. Because of the rapid rotation of the wing, some of the vorticity shed from the leading edge before flow attachment did not have time to be carried away and was trapped in the stagnation flow to be swept forward and upward, and eventually carried away above the wing.

The exact distribution of the lift and drag forces on the airfoil surface is not known because the pressure distribution was not measured. However, it can be roughly estimated from the flow pattern, and the resulting estimate of the torque as a function of angle of attack agreed with the measured angular acceleration data.

---

*N. Ham[1] observed large lift peaks due to vortex-induced loading in the dynamic stall of a wing at $\alpha = 20^{o}$ to 30^{o} at Strouhal numbers from 0.03 to 0.12. In the autorotation tests the peak should appear as a drag peak since the stalling angle was nearly 90^{o} because of the much higher Strouhal number.

The angular acceleration was zero at zero angle of attack, corresponding to the lift vector acting through the mid-chord (see Fig. 12 - 14). As the angle of attack increased, the forward stagnation point moved from the leading edge onto the lower surface and created a high pressure area there, while the flow became faster over the upper surface of the leading edge, causing a lower pressure there. This produced a driving moment and positive angular acceleration, although the resultant force still acted less than 0. 12c from the mid-chord. The angular acceleration reached its maximum at $\alpha = 35^{o}$, and then began to decrease as the forward stagnation point moved toward the mid-chord. The angular acceleration vanished at $\alpha = 95^{o}$, and then became negative. As the wing continued to rotate, the forward stagnation point moved toward the advancing edge and the flow became faster over the retreating edge*. This produced a couple on the wing, which produced a large retarding moment, even though the resultant force on the wing was small at the time (the resultant force actually acted ahead of the leading edge at $\alpha = -60^{o}$). The retarding moment reached its maximum at $\alpha = -45^{o}$, and then decreased to zero again at zero angle of attack to complete the cycle.

---

*The pressure at the stagnation point may have been considerably above the total pressure, since the advancing edge was moving rapidly forward.

C. INFLUENCE OF STROUHAL NUMBER AND REYNOLDS NUMBER

The Strouhal number and Reynolds number were primary parameters for the flow pattern. For free autorotation, the Reynolds number determines the Strouhal number. However, in the water tunnel tests, the Strouhal number could be varied independently of the Reynolds number (see Part D of Chapter II), so the effect of the two parameters could be studied separately. It is also possible for the Strouhal number to vary independently of the Reynolds number because of differences in bearing friction.

The Strouhal number had a strong influence on the flow pattern. As it was increased at a given Reynolds number the wing stalled later and the flow reattached to the lower surface later with the stagnation point further from the leading edge at attachment (see Fig. 15). At low Strouhal numbers, the leading edge eddy was shed well before the trailing edge eddy, but as the Strouhal number increased (at the same Reynolds number) the trailing edge eddy was shed sooner relative to the leading edge eddy, and for Strouhal numbers greater than 0. 25, they were shed nearly simultaneously*. As the Strouhal number was

---

*N. Ham[1] studied dynamic stall and also observed strong vortex shedding from the leading edge, with the trailing edge vortex shed later as the leading edge vortex moved back. His observations, however, were at much lower angles of attack and Strouhal numbers than in the autorotation tests. He observed a small vortex shed from the trailing edge just as the leading edge vortex was shed. This was not observed in the autorotation tests.

increased beyond the autorotation range, the eddy shed from the leading edge became smaller and eventually disappeared. At a high enough Strouhal number, the flow never attached to the wing as on a static wing, but the streamlines around the wing became closed and the flow pattern away from the wing resembled that over a rotating cylinder.

The Reynolds number had a much smaller influence on the flow pattern than the Strouhal number. The flow pattern was observed for Reynolds numbers from 5000 to 90,000, and was qualitatively unchanged. However, the wing stalled at slightly lower angles of attack for a given Strouhal number at lower Reynolds numbers. At Re = 90,000, in the 5 x 7 ft tunnel, the flow began to separate at $\alpha = 80^{\circ}$ at a Strouhal number of 0.30, compared to 67° for Re = 5000 and a Strouhal number of 0.35 in the water tunnel. Separation would, of course, occur still sooner at a Strouhal number of 0.30.

D. INFLUENCE OF AIRFOIL SHAPE

It should be noted that the airfoil in the water tunnel was a flat plate airfoil, while the wing in the 5 x 7 ft tunnel was of elliptical airfoil. The flow patterns over these airfoils were similar and both stalled at about the same angle of attack for the same Strouhal number and Reynolds number. Thus, it appears that the difference in stalling angles mentioned above was caused primarily by the Reynolds

number difference. There was one difference observed in the flow patterns over the two airfoils. For the flat plate, the stagnation point moved to the advancing edge at $\alpha = -20^{o}$; while it did not reach the advancing edge until $\alpha = 25^{o}$ for the elliptical airfoil but remained slightly behind it on the lower surface (see Fig. 16). Balsa strips of . 083c width were mounted on the elliptical airfoil to produce a sharp edge; the stagnation point then moved to the edge at about zero angle of attack.

V. AERODYNAMIC FORCES

A. INTRODUCTION

In Chapter IV, the flow pattern was described and the relationship between the flow pattern and the unsteady aerodynamic forces was explained. This chapter discusses the magnitude of these forces and the influence of Reynolds number on them. All of the aerodynamic force data discussed in this chapter was obtained with the large wing described in Part C of Chapter II.

B. LIFT AND DRAG FORCES

The unsteady aerodynamic effects (discussed in Chapter IV) caused the lift and drag to be much larger than for a conventional wing in steady flow (see Fig. 17-20). The peak lift coefficient was 4. 5 at Re = 240, 000, with an average value of 2. 2, while the peak drag coefficient was 4. 3 with an average value of 1. 60. The minimum drag was also fairly large, but the minimum lift was very small, only about 8% of the maximum positive lift at the same Reynolds number.

The average and maximum lift and drag coefficients increased with increasing Reynolds number, and were still increasing at the maximum Reynolds number tested. Presumably, they should eventually approach an asymptotic limit at a sufficiently high Reynolds number, but this limit is unknown at present. Unfortunately, it was impossible to measure the lift and drag in the range of Reynolds numbers where the

Strouhal number had its maximum and following minimum. At these Reynolds numbers, the dynamic pressure was very low and the strain gauges were not sensitive enough to measure the very small lift and drag forces. However, it seems probable that the lift and drag coefficients would also show a similar maximum and following minimum.

Although the magnitude of the peak and average lift and drag coefficients changed considerably for different Reynolds numbers, the curves of lift and drag vs angle of attack were qualitatively unchanged. The only significant changes were that the maximum drag and minimum lift occurred slightly later and the minimum drag occurred slightly earlier at higher Reynolds numbers (see Fig. 21). The cause of the later maximum drag and minimum lift was that the wing stalled later at higher Reynolds numbers, primarily because of the higher Strouhal number*. Since the wing stalled later, the vortex induced loading that caused the drag peak occurred later. The vortices were then shed later, so the lift decreased to a minimum later. The reason the minimum drag came earlier in the cycle at higher Reynolds numbers is not known.

Because the drag was so large, the lift to drag ratio of the wing was much less than for a conventional wing (see Fig. 22). The lift to

---

* The stall angle also increased slightly at higher Reynolds numbers for the same Strouhal number (see Part C of Chapter IV).

drag ratio increased with increasing Reynolds number and approached an asymptotic limit. With the air bearings, this limit was reached at about Re = 100,000. With the mechanical bearings, the lift to drag ratio was lower, but appeared to approach the same limit at a higher Reynolds number.

C. ANGULAR ACCELERATION

The peak angular acceleration was much less than if the peak lift had acted through the quarter chord as in the static case, and corresponded to a very small fluctuation in the angular velocity. The curve of angular acceleration was very nearly sinusoidal with the peak angular acceleration at 35^{o} angle of attack and minimum angular acceleration at -45^{o} angle of attack (see Fig. 12). The shape of the curve was unchanged over the range of Reynolds numbers tested. No shift in peak locations was observed at higher Reynolds numbers. However, a small shift might not have been noticed since the signal to noise ratio was poorer than for the lift and drag data.

The angular acceleration was nondimensionalized by dividing it by w^2. The resulting quantity $\ddot{\alpha}_p/w^2$ is approximately proportional to the angular velocity fluctuation; it would be exactly proportional if the angular acceleration were perfectly sinusoidal. This can be shown by letting a sine wave of the same frequency and amplitude represent the

angular acceleration and integrating it*. Since the angular acceleration was very nearly sinusoidal, this approximation was quite accurate.

The nondimensional angular acceleration is shown as a function of Reynolds number in Fig. 23. It was quite small and decreased with increasing Reynolds number. It followed the same trend, but was slightly higher when the mechanical bearings were used (see Chapter IX). The angular velocity fluctuation was calculated and was only ± 2.1% at Re = 108,000.

Because the fluctuations in angular velocity were small, the wing could be assumed to rotate at a constant angular velocity. This greatly simplified analysis of the motion, since it was then necessary to know the angle of attack at only one point in a plot of a function of time. The angle of attack of any other point was given simply by $\alpha = \alpha_0 + wt$, where α_0 was the angle of attack at the known point. In the experiment the single point was obtained by the photocell position

---

*Consider the equation $\ddot{\alpha} = \ddot{\alpha}_p \sin wt$. If this is integrated and divided by w, one gets $\dot{\alpha}/w = E/w - (\ddot{\alpha}_p/w^2) \cos wt$, where $\dot{\alpha}$ is the instantaneous angular velocity and E the integration constant. However $\dot{\alpha}$ averaged over a cycle equals w, so $\dot{\alpha}/w = 1 - \ddot{\alpha}_p/w^2 \cos wt$.

measuring system. The error caused by the assumption of constant angular velocity was calculated and was only 0. 61^{o} maximum at Re = 108,000. Hence, this assumption was used throughout the tests*.

It should be noted that for a wing with a much lower I or Reynolds number, or with a large retarding torque (see Chapter IX), the angular velocity fluctuations would become larger and the assumption of constant angular velocity might not be satisfactory.

VI. STROUHAL NUMBER

A. INTRODUCTION

The nondimensional frequency of a periodic phenomenon, nc/V is defined as the Strouhal number. This number can be interpreted as the ratio of the time for the flow to travel one body chord length at the free stream velocity, c/V, to the time required for the phenomenon to complete one period, 1/n. For an autorotating wing, the flow cycle repeats itself twice per wing revolution. Hence, the Strouhal number should actually be 2 nc/V, but the usual definition nc/V was used to avoid confusion. The ratio of edge speed to free stream velocity is given by πS, and this ratio is sometimes given instead of the Strouhal number.

B. INFLUENCE OF REYNOLDS NUMBER

The Strouhal number was measured over a wide range of Reynolds numbers for a 15% thick elliptical airfoil, which was symmetric both fore and aft and vertically (see Fig. 24). The Strouhal number increased when the Reynolds number increased up to Re = 7500 for needle bearings and Re = 13,000 for air bearings, then decreased to a minimum*. Following the minimum, it increased and approached an asymptotic limit of S = 0.35.

A group of students working under Coles[6] observed a similar peak for a flat plate in fixed axis autorotation with I = 55.6.

The probable reason for the increase in Strouhal numbers at higher Reynolds numbers (above the local maximum and following minimum) is the later stall of the wing at higher Reynolds numbers for a given Strouhal number (see Part C of Chapter IV). Because of the later stall, the lift pulse lasts longer and reaches a higher maximum. This increases the driving moment on the wing, and thus, the rotation rate. The increased rotation rate further increases the stall angle, so that the lift and rotation rate are increased still more. Thus, the Strouhal number is quite sensitive to changes in the Reynolds number.

The cause of the peak in the Strouhal number at Re = 7500 to 13,000 is not known, but it may be the result of transition to a turbulent boundary layer on the suction side of the wing. In view of the large difference in the location of the peak and following minimum for the needle and air bearings, it would appear that the peak location is quite sensitive to changes in the Strouhal number. When the Strouhal number of the flat plate airfoil (see below) was reduced by increased bearing friction or lower I*, the peak occurred at still lower Reynolds numbers (see Fig. 25).

C. INFLUENCE OF AIRFOIL SECTION

Three other airfoils, a flat plate, a 15% thick ellipse with its edges blunted, and a 15% thick symmetrical wedge, were also tested over a

smaller range of Reynolds number (see Fig. 26). All of these airfoils were symmetric both fore and aft as well as vertically. These airfoils all gave similar results, with the Strouhal number behaving in the same manner as for the elliptical airfoil. However, the flat plate and blunt edged ellipse gave somewhat higher Strouhal numbers than the elliptical airfoils, while the wedge airfoil gave lower values. The cause of the higher Strouhal numbers for the flat plate and blunt edged ellipse is unknown. The wedge airfoil probably gave lower Strouhal numbers because its airfoil caused premature separation at the sharp mid-chord ridge.

D. INFLUENCE OF MOMENT OF INERTIA

As explained in Part A of Chapter IV, an autorotating wing must have sufficient inertia in order to be able to overcome the retarding torque that exists during part of its cycle. As the inertia is further increased, the Strouhal number increases because the wing is slowed less during the stalled portion of its cycle. A wing with lower inertia does not get a corresponding gain during the unstalled portion of its cycle, since its speed is limited by the flow velocity. Thus, the Strouhal number increases with increasing inertia and asymptotically approaches a limiting value at which the wing would attain a constant angular velocity.

The moment of inertia required for autorotation is quite low. The minimum I* for fixed axis autorotation was only 0. 623 with tip plates at Re = 1800 and 1. 20 without them at Re = 5130. At I* = 10, the angular velocity was already quite close to the limiting value, as can be seen in Fig. 27 and 28. The angular velocity has also become nearly constant, with fluctuations of $\pm$ 2. 1% for I* = 8. 47 and Re = 108, 000.

E. INFLUENCE OF ASPECT RATIO

The influence of the aspect ratio of the wing onthe Strouhal number was small. The Strouhal number was higher for higher aspect ratios and approached an asymptotic limit (see Fig. 29)*. The decrease in Strouhal number for lower aspect ratios was probably caused by loss of lift at the tips, as with conventional wings of finite aspect ratio.

Because of their finite aspect ratios, the wings had to shed tip vortices in addition to those shed from the wing edges as the lift fluctuated, although their exact behavior is unknown. The tip vortices were probably at least partially responsible for the rapid disintegration of the vortices shed from the leading and trailing edges (see Part C of Section VII).

---

* The bearings used for the tests of the influence of the aspect ratio and tip plate configuration on the Strouhal number were inferior to those used for the tests of the influence of the Reynolds number, described above. Therefore, the Strouhal numbers are somewhat lower.

F. INFLUENCE OF TIP PLATE CONFIGURATION

The modest effect of the aspect ratio on the Strouhal number shows that the tip plates of 1.33c diameter were fairly effective in reducing tip losses. The tuft tests also indicated near two dimensional flow. In these tests, there was no noticeable difference in the behavior of the tufts at different positions along the span, even for the tufts only one inch from the tip plates.

A number of tip plate configurations were tested (see Fig. 30). The smaller tip plates probably gave lower Strouhal numbers because they allowed excessive tip losses. The larger plates also gave lower Strouhal numbers, probably because they caused excess drag, which more than cancelled the gain from increased wing tip efficiency.

Fixed tip plates were much less effective than rotating plates attached to the wing. Their effectiveness decreased when the gap between the wing and tip plates was enlarged (see Fig. 31). A larger set of fixed tip plates of approximately tear drop shape was also tested and gave lower Strouhal numbers than the round plates for the same gap. There appear to be two primary reasons for the poor performance of the fixed tip plates. The first is the loss of lift because of air leakage through the gap, shown by the rapid decrease in the Strouhal number when the gap was enlarged. The other is the retarding torque on the

wing resulting from its having to plow through the thick boundary layer on the fixed tip plates, shown by the poorer results with larger tip plates. However, all of the tip plate configurations tested were at least slightly better than no tip plates.

VII. THEORETICAL ESTIMATE OF DRAG

A. INTRODUCTION

Since an autorotating wing sheds vorticity of alternate sign periodically in a manner similar to the Von Karman vortex street formed behind a circular cylinder at certain Reynolds numbers, it was thought that the drag calculation done by Von Karman[17] for a circular cylinder shedding periodic vortices could be at least approximately applied to the autorotating wing.

B. DRAG CALCULATION

Von Karman's theory is based on the assumption of equally spaced vortices in two rows, of opposite signs, shed by the cylinder. For a flow from left to right, the vorticity in the upper row would be clockwise and in the lower counter-clockwise. The array of vortices induces velocities that result in both rows having a forward velocity relative to the free stream, so that the wake velocity is less than the free stream velocity when measured from the reference point of the cylinder.

In his solution, Von Karman used a control volume, which was large compared to the cylinder. It moved with the vortices and passed between them, so that the control volume never passed through a vortex. This was necessary because the ideal vortex model used had an infinite velocity at its center. He then calculated the average drag by means of the momentum equation, taking into account both the momentum

passing through the boundaries and that being created as the cylinder shed additional vortices. To get the average drag, the part contributed by the new vortices was integrated over a period and averaged. However, conditions at the boundaries of the control volume were assumed steady for the calculation of the momentum flux and pressure forces. This gave the formula:

$$D = 2\pi \Gamma \rho \frac{b}{a} (V - 2U) + \frac{2\pi \Gamma^2 \rho}{a}$$

and the vortex velocity

$$U = \frac{\Gamma \pi}{a} \tanh \pi \frac{b}{a} \quad ,$$

where a is the vertical spacing of the vortices, b is the horizontal spacing, and U is the vortex velocity relative to the free stream. Von Karman also performed a stability analysis by considering small perturbations in the vortex locations and found that the vertical spacing of the vortices must be 0. 281 of the horizontal spacing for stability of the flow configuration.

This theory gives the drag provided the vertical or horizontal spacing of the vortices and either the velocity of the vortices or their circulation is known. For the autorotating wing, the circulation was not known, since in an unsteady flow, the equation $L = \rho V \Gamma$ is not valid (see Part B of Chapter IV). Hence, an experimental measurement was needed. Since the vortex velocity was much easier to

measure than the circulation, this was measured, along with the vortex spacing, by means of titanium oxide smoke. Titanium tetrachloride was painted on the wing edges and made the vortices clearly visible as it was carried away and oxidized. The wake was initially about one chord length wide, but spread to two to three chord lengths far downstream. Also, it disintegrated into rather random turbulence within about ten chord lengths, probably at least partly because of three dimensional effects (the wing had an aspect ratio of 4. 94). The average speed of the vortices was timed and was 0. 86 of the free stream velocity, which corresponds to $U = 0.14V$. Using this value in Von Karman's equation for the drag, along with the observed vertical spacing of the vortices (approximately 1. 5c), the computed drag coefficient was 0. 51 for a Reynolds number of 1000. This estimate of the drag does not, of course, include the induced drag caused by the finite aspect ratio of the wing. Although the wing had tip plates, these were of finite size, and did not fully eliminate the tip losses.

C. DISCUSSION OF RESULTS

This calculation was only an approximation for a variety of reasons. It is assumed in the Von Karman theory that the vorticity is in discreet vortices of uniform spacing and that they have the stable ratio of vertical to horizontal spacing of 0. 281. Also, two dimensional flow is assumed, with viscous effects neglected. For the actual flow, the vortex

shed when the flow collapsed was shed as a single discreet vortex, but the vorticity shed as the lift built up was shed in several vortices. The spacing of the vortices was determined by the wing rotation rate and the ratio of the vertical to horizontal spacing was not necessarily 0. 281, though it was of this magnitude. It was thought that it might tend to hold this value, but this did not occur. Also, the wake spread downstream of the model instead of being of constant width, and disintegrated rather rapidly.

However, the flow did initially resemble the Von Karman vortex street, so the calculation should give a satisfactory estimate of the order of magnitude of the drag. The measured drag data appear to confirm this. While no drag data were taken for a Reynolds number of 1000, the drag was measured at higher Reynolds numbers. For fixed-axis autorotation at Re = 25, 000, the average drag coefficient was 0. 81 after subtracting the estimated induced drag of 0. 26*. A drop test at Re = 2020 showed a similar result, with an average drag coefficient of 0. 69 after subtracting the estimated induced drag of 0.05**.

---

* It was estimated as described in Part E of Chapter II.

** The induced drag was less in this test because the wing had a higher aspect ratio and lower lift coefficient.

Hence, it is probably impossible to obtain a high lift to drag ratio for an autorotating wing because of the energy lost in the large vortices that are periodically shed. Even if the induced drag from a finite aspect ratio could be avoided, there would still be a large amount of drag from the vortices shed as the lift fluctuated.

VIII. FENCE TESTS

A. INTRODUCTION

To gain a further understanding of the autorotation phenomenon, spanwise fences were mounted on the instrumented wing discussed in Part C of Chapter II. The peak lift and rotation rate were measured with a pair of 0.083c high fences at various positions along the chord and for fences of various heights at the mid-chord. Although only the peak lift was measured, the lift vs angle of attack curve remained roughly sinusoidal for all fence positions. Therefore, the average lift was still about half of the peak lift, as with no fences.

B. INFLUENCE OF FENCE POSITION

The flow over the wing was investigated with titanium oxide smoke, and the cause of the changes in the peak lift coefficient and Strouhal number for different fence positions was clear (see Fig. 33-35). With the fences on the lower surface of the leading edge and upper surface of the trailing edge (d/c = 0)*, the Strouhal number and lift coefficient were greater than with no fences. At this position, the leading edge fence gave camber during the lift portion of the cycle. The other fence probably disturbed the flow over the upper (suction) surface somewhat, but did not cause premature separation.

---

*Figure 32 defines d/c.

When the fences were moved back from the edges, the peak lift coefficient and Strouhal number decreased. This happened because the camber effect was lost and the other fence began to cause early separation of the flow on the upper surface. A vortex formed behind the fence on the upper surface and was shed at a quite low angle of attack. At the mid-chord fence position, this vortex was shed at about $\alpha = 30^{o}$, with another one of about the same size shed from the leading edge at about $\alpha = 90^{o}$, along with the usual one from the trailing edge.

To further study the early separation, the lift was observed with a fence on only one side of the wing at the mid-chord. The peak lift coefficient was greater for the lift cycle with the fence on the upper surface because of a sharp peak just as the vortex was shed. This was probably a vortex-induced load, as observed by Ham[1], and described in the footnote on page 37.

As the fences were moved past the mid-chord (d/c increasing), the Strouhal number and peak lift coefficient suddenly increased sharply at d/c = 0.64. This happened because the fence no longer caused early separation. The flow remained attached to the upper surface up to a fairly high angle of attack, and then separated in the same manner as observed with no fences.

When the fences were moved further toward the edges (d/c approaching one), the advancing fence began to form a negative camber, and the Strouhal number decreased rapidly. However, the peak lift coefficient continued to increase, although it was still less than for d/c = 0. A possible reason for this is that the fence at the leading edge disturbed the flow over the upper surface less than when it was further back. This would increase the peak lift coefficient, and evidently more than compensated for the negative camber and reduced Strouhal number.

C. INFLUENCE OF FENCE HEIGHT

The peak lift coefficient and Strouhal number decreased as the height of a pair of mid-chord fences was increased (see Fig. 36 and 37). Although the flow pattern was not studied for fence heights other than 0.083c, it was probably similar for all of the fence heights tested. The higher fences probably caused a greater decrease in the peak lift coefficient and Strouhal number because they affected the flow in the boundary layer to a greater extent with the result that the flow separated at the fence at a lower angle of attack. At a fence height of 0.25c, the wing could no longer autorotate. The lift was so greatly reduced that the wing could not gain enough angular momentum to pass through the stalled protion of its cycle.

The peak lift coefficient and Strouhal number were both nearly independent of Reynolds number. This is in sharp contrast to the results obtained with no fences; the peak lift coefficient and Strouhal number increased rapidly with increasing Reynolds number for the same range of Reynolds numbers. The probable reason for the different behavior is that the boundary layer was thinner at higher Reynolds numbers, so that the fences were effectively higher. This increased the loss of lift caused by the fences, and apparently more than cancelled the gain that would otherwise result from the higher Reynolds number.

IX. AUTOROTATION WITH RETARDING TORQUE

A. INTRODUCTION

As explained in Chapter IV, when an autorotating wing is started, it experiences a large net driving torque. This increases its angular velocity until the average torque is reduced to zero by aerodynamic damping. Hence, a wing can autorotate more slowly than its free autorotation rate, and extract energy from the air stream in the manner of a windmill. As the torque is increased, the rotation rate decreases. Eventually, at a sufficiently high retarding torque, the wing is no longer able to pass through the stalled portion of its cycle, and autorotation becomes impossible.

To study this phenomenon, the wing was fitted with a pulley and allowed to raise a weight hanging from a thread wrapped around the pulley. The weight applied a constant known torque to the wing (see Part C of Chapter II).

B. STROUHAL NUMBER

The Strouhal number decreased monotonically when the retarding torque increased, and was very sensitive to retarding torque at low torques. Hence, even a small amount of bearing friction would appreciably slow the wing. This was observed when the air bearings were replaced with mechanical bearings, and the Strouhal number was considerably reduced (see Fig. 24).

The Strouhal number increased at higher Reynolds numbers for a given torque coefficient (non-dimensional torque, C_T), as expected. Also, the wing was able to withstand a greater torque coefficient before it stopped autorotating at higher Reynolds numbers. At higher Reynolds numbers the wing developed a higher peak lift coefficient, even for the same Strouhal number. Hence, the wing could produce a greater driving torque.

C. AERODYNAMIC FORCES

The peak lift coefficient also decreased when the retarding torque was increased, but was less sensitive than the Strouhal number (see Fig. 39). For a given torque coefficient, the peak lift coefficient increased at higher Reynolds numbers, as was observed with no torque. The curve of lift vs angle of attack was also similar to that observed with no torque. Hence, the average lift coefficients were still about half the peak lift coefficients.

The peak drag coefficient was much less sensitive to retarding torque than the peak lift coefficient and Strouhal number. However, it did decrease slightly when the retarding torque increased (see Fig. 40). It was probably less sensitive because a large part of the drag was produced by the blockage of the wing. This existed regardless of the Strouhal number, while almost all of the lift was produced by effects depending upon wing rotation.

For a given torque coefficient, the peak drag coefficient increased with increasing Reynolds number. The behavior was similar to the case with zero retarding torque. However, the curve of the drag vs angle of attack was different. The negative drag became smaller compared to the positive drag and vanished for torque coefficients greater than 0. 10. This increased the average drag coefficient, so that it was probably about 0. 4 to 0. 5 of the peak drag coefficient.

The angular acceleration decreased with increasing retarding torque. However, the angular acceleration non-dimensionalized over w^2 increased rapidly because the decrease in w^2 was much greater than the decrease in $\ddot{\alpha}_p$ (see Fig. 41 and 42 and Part C of Chapter V). This indicates a greater fluctuation in angular velocity, and was expected since at a sufficiently high torque, the angular velocity became almost zero just as the wing passed through zero angle of attack.

D. POWER OUTPUT

The power output from the wing was obtained by multiplying the retarding torque and wing rotation rate together. It was then non-dimensionalized to yield the power coefficient, C_p (see Fig. 43). As the retarding torque was increased, the power coefficient increased until it reached a maximum. Then, the decreasing Strouhal number began to outweigh the increasing torque, and the power coefficient

decreased somewhat. The power coefficient increased at higher Reynolds numbers because the Strouhal number was higher for a given torque coefficient.

The maximum power coefficient was 0. 094 at Re = 94, 500, compared to 0. 145 to 0. 425 for various types of windmills*[18]. Although the power coefficient for the autorotating wing increased at higher Reynolds numbers, it seems doubtful that it will ever become as efficient as a well designed windmill.

E. EFFECT OF DRIVING TORQUE

Since reducing the Strouhal number of the wing reduced the peak and average lift and drag coefficients, it seemed probable that increasing the Strouhal number should increase them. This was found to be true, but detailed measurements were not made, because the apparatus did not allow sufficient running time. Crabtree[5] studied powered rotating wings and measured an average lift coefficient of 12. 5 at a Strouhal number of 3. 2. He did not measure the drag, but it was probably also very large.

---

*Power coefficient for a windmill is based on its disc area; for the autorotating wing, it is based on the wing area.

X. DROP TESTS

A. INTRODUCTION

The motion of a freely falling autorotating wing differs from that of a wing autorotating about a fixed axis in that it has six degrees of freedom instead of one. This problem can be simplified if the wing is assumed not to sideslip and the spanwise axis of rotation is assumed not to rotate about a horizontal or vertical axis. This means that the wing motion is two-dimensional and reduces the number of degrees of freedom to three. Two-dimensional motion is observed for a large aspect ratio wing autorotating in a stable manner. The two additional degrees of freedom allow the wing to rise and fall about its average path and to change speed along its path, in effect changing the free stream velocity and Strouhal number. There is, of course, a coupling between the wing motion and the forces causing it.

B. EXPERIMENTAL RESULTS

A group of students working under Coles [6] studied the motion of falling autorotating wings by photographing their flight. A strobe lamp flashed every 1/180 second and provided a series of images that showed the path and angular position as a function of time. They found that the lift to drag ratio increased from 0.78 for an aspect ratio of

1. 13 to 1. 40 for an aspect ratio of nine (see Fig. 44). The average lift coefficient, based on the average velocity of the wing along its path, was 1. 69 for an aspect ratio of nine.

Our work also included some drop tests. A number of wings were dropped and their lift to drag ratios and lift coefficients measured. Our tests showed results similar to those of Coles[6], but the lift to drag ratios and average lift coefficients were somewhat higher for a given aspect ratio. A wing with an aspect ratio of 1. 33 had a lift to drag ratio of 1. 24 and an average lift coefficient of 1. 61 (again based on its average speed along its path). For a wing with an aspect ratio of four, the lift to drag ratio increased to 1. 58 and the average lift coefficient was 2. 09.

Our tests probably gave higher lift coefficients and lift to drag ratios because of higher Reynolds numbers and larger tip plates. Our wings had 1. 33c diameter tip plates and Reynolds numbers of about 10, 000, compared to 1. 0c diameter tip plates and Reynolds numbers of about 4500 for the tests of Coles. The I* were also different, I* = 9. 0 in our tests and I* = 4. 0 in Coles' tests, but the effect of this difference was probably small. The influence of I* on the average lift coefficient and lift to drag ratio was not studied in detail. However, the lift to drag ratio was not changed appreciably by even very large changes in I* provided I* was greater than one.

In all of the drop tests described above, as well as the fixed axis tests, the wings were symmetric both fore and aft and vertically. It seemed possible that a properly cambered airfoil might give substantially more lift. To investigate this, an S-shaped airfoil formed from two circular arcs of 1.0c radius was built. This did give a considerably greater Strouhal number in both drop tests and fixed axis autorotation. However, in drop tests, the average lift coefficient and lift to drag ratio were not significantly changed. When the wing was rotated against its camber (i.e., with the forward half of the wing cambered negatively), the Strouhal number decreased to well below that obtained with a flat plate. However, the lift to drag ratio decreased only slightly, and the average lift coefficient was still almost unchanged. It appears that a cambered wing offers no advantages except that it has a preferred direction of rotation. In some tests with an aluminum foil wing, a camber of about 0.5c radius was sufficient to ensure that the wing would always rotate toward its camber when it was dropped, regardless of how it was dropped or initially spun.

C. DISCUSSION

The flow pattern for a freely falling autorotating wing is probably qualitatively similar to that for autorotation about a fixed axis, at least when I* is high enough to insure reasonably rapid rotation. For

the tests of Coles with $I^* = 4.0$, the maximum deviation from the mean path of the wing was about 0.05c, the maximum slope of the path relative to the mean path was about 10^o, and the maximum fluctuation in the velocity was about ± 10%. The fluctuation in angular velocity was ± 6.7%, comparable to that observed in fixed-axis autorotation, which was ±3.3% at Re = 40,000 and $I^* = 8.46$, and increased when the Reynolds number or I^* was decreased. Hence, the wing motion was similar to that of a fixed-axis autorotating wing viewed from a reference point moving at the free stream velocity, and the flow patterns should be similar. If so, the aerodynamic forces should be approximately the same functions of angle of attack. This was found to occur. The Reynolds numbers were different, about 90,000 for the fixed-axis tests, vs 4500 for the drop tests, but the flow pattern was not observed to change much over this range of Reynolds number in the fixed-axis tests (see Part C of Chapter IV).

The angular velocity was maximum at $\alpha = 67^o$ and minimum at $\alpha = -16^o$, compared to a maximum at $\alpha = 95^o$ and a minimum at 0^o for fixed-axis autorotation. The expected peak locations for the velocity parallel and perpendicular to the mean path can be roughly estimated from the measured lift and drag data for the fixed-axis tests and should agree with those observed in the drop tests of Coles if the

aerodynamic forces are similar functions of angle of attack. For a falling wing, its weight is balanced by inertial and aerodynamic forces. Using D'Alembert's principle, the balance is (see Fig. 45):

$$W \sin \theta = D - m\ddot{x}$$

$$W \cos \theta = L - m\ddot{y}$$

The equations for the average motion can also be written:

$$W \sin \lambda = D_a$$

$$W \cos \lambda = L_a$$

Since $\theta \cong \lambda$, the equations can be combined to yield

$$D - D_a = m\ddot{x}$$

$$L - L_a = m\ddot{y}$$

From this, one can see that when the drag is less than the average drag, the wing will accelerate until the drag reaches the average drag. Then it will deaccelerate until the drag decreases to the average drag again, and then begin to accelerate again as the cycle repeats itself. Thus, the velocity should be maximum just as the drag passes through the average drag and becomes less than it. This calculation predicted a maximum velocity at $\alpha = 23^{\circ}$ and a minimum at $\alpha = -40^{\circ}$, while the drop tests showed a maximum at $\alpha = 40^{\circ}$ and a minimum at $\alpha = -50^{\circ}$.

The point of maximum velocity perpendicular to the mean path for the drop tests were determined from inspection of the photograph of wing position vs time obtained by Coles[6]. The points of maximum slope were fairly clear, and these were the points of maximum velocity perpendicular to the mean path (neglecting the variation in velocity parallel to the path). This gave a maximum at $\alpha = 45^{o}$ and a minimum at $\alpha = -30^{o}$. The location of the maximum and minimum velocity perpendicular to the mean path can also be estimated from the fixed-axis lift data, as was done for the drag. This gave a maximum at $\alpha = 60^{o}$ and a minimum at $\alpha = -30^{o}$ for Re = 78,000, again quite good agreement.

Comparison of the data for falling wings to that for fixed-axis autorotation showed that the freely falling wings had higher lift to drag ratios and average lift coefficients (based on their average speed along their path). The Reynolds numbers were lower than for the fixed-axis autorotation lift data, but the average lift coefficient and lift to drag ratio of the falling wings would probably be still higher at higher Reynolds numbers. The Strouhal number was also higher, 0.306 vs 0.215 for fixed-axis autorotation for the same I* and Reynolds number* The reasons for this are probably the fluctuation in velocity and in displacement

---

* The aspect ratios were slightly different, 9.0 in the drop test, compared to 6.42 for fixed-axis autorotation. However, our tests showed the Strouhal number to be insensitive to aspect ratio for aspect ratios greater than three (see Part E of Chapter VI).

perpendicular to the average path. The velocity was greatest at about $\alpha = 40^{o}$, near the maximum lift point shown in fixed-axis tests, while it was lowest at about $\alpha = -50^{o}$, near the minimum lift point. Hence, the average lift coefficient was increased substantially, since the velocity was about 10% higher when the lift was maximum. The instantaneous drag and velocity fluctuations were less well in phase, since the peak drag was not reached until $\alpha = 80^{o}$ in the fixed-axis tests. Hence, the drag was probably increased less. Although the change in angle of attack caused by the fluctuation in displacement perpendicular to the average path was small, the maximum upward velocity occurred at $\alpha = 45^{o}$, which reduced the true angle of attack and probably delayed the stall somewhat. Also, the peak downward velocity occurred at $\alpha = -30^{o}$ and then reduced the true negative angle of attack, so the lift could begin to increase sooner. Hence, the average lift was probably further increased. The longer lift cycle would also tend to increase the Strouhal number, which was observed to be greater. Some of the increase in the Strouhal number was, of course, caused by the absence of bearing friction, but it seems doubtful that bearing friction could account for all of the difference.

D. RANGE OF REYNOLDS NUMBER AND I* FOR DIFFERENT TYPES OF WING MOTION

For sufficiently low Reynolds numbers or I*, falling wings did not autorotate, but fell in a stable manner or with a rocking motion. The boundaries of Reynolds number and I* were found by dropping wings of various size and I* into various fluids (see Fig. 46).

For Reynolds numbers less than 50 to 85, depending on I*, the wings fell steadily perpendicular to the flow without any sort of periodic motion and would move to a position perpendicular to the flow if dropped in some other position*. For higher Reynolds numbers, the wings fell with a slight rocking motion that became more severe at higher Reynolds numbers. At sufficiently high Reynolds numbers and I*, the wings began to autorotate. For I* less than 0. 20, the wings did not autorotate even at high Reynolds numbers, but the oscillations became a periodic gliding type of motion with large horizontal displacements. For the periodic rocking motion, the Strouhal number decreased when I* increased, for a given Reynolds number (see Fig. 47).

---

*On page 199 of Ref. 19, it is reported that for Reynolds numbers less than one, a body with three mutually perpendicular planes of symmetry will not orient itself but will remain in its initial position.

The flow pattern was not studied, but this is well discussed by Willmarth, Hawk, and Harvey[19] for falling disks, which behave in the same manner and probably have very similar flow patterns. The basic mechanism is that for sufficiently low Reynolds numbers, the wake behind the disk or wing is stable with no periodic vortex shedding, and therefore, no pitching moments on the model. As the Reynolds number increases, the wake becomes unstable and the model begins to oscillate and to shed periodic vortices. At higher Reynolds numbers and I*, the model oscillates more and more violently after release until it overturns and begins to autorotate.

The boundary locations for the three types of motion were similar for the disk and flat plate, except that for the flat plate, a much higher I* was required for autorotation for a given Reynolds number (see Fig. 46). The Strouhal numbers were also higher in rocking motion for the flat plate than for the disk for a given Reynolds number and I* (see Fig. 47). For both the disk and flat plate, the Strouhal number decreased when I* increased, for a given Reynolds number.

The reason that the flat plate required a higher I* for autorotation is probably that the disk could autorotate without turning directly over. That is, it could rotate to an angle of attack of

perhaps 45^{o}, then fall over by rotating about an axis at an angle to the horizontal. This is the cause of the very random tumbling of a disk[19]. In contrast, a rectangular plate with an aspect ratio much greater than one can not do this readily because of the stabilizing effect of the large aspect ratio, and it must therefore rotate directly over, which requires more angular momentum.

XI. AUTOROTATION OF SPHERES AND CIRCULAR CYLINDERS

A. INTRODUCTION

It was thought that a sphere or circular cylinder might also autorotate. It is well known[20] that when a circular cylinder with its axis perpendicular to the flow is rotated that the separation line moves much further rearward on the upper side (for flow from left to right with clockwise rotation) and that there is a net clockwise circulation and upward lift. The rearward location of the separation line should produce a torque in the direction of rotation, since there is an appreciable shearing stress in that direction over a larger area than in the opposite direction on the lower surface. However, the rotation of the sphere or cylinder will decrease the relative velocity between the flow and the body surface on the upper surface and increase it on the lower surface; this will produce a torque opposing the rotation. It was thought that a balance between these forces might result at some rotational speed other than zero and the model would autorotate, once started.

B. EXPERIMENTAL RESULTS

There was no evidence of autorotation. The range of Reynolds numbers was from 940 to 16,800 for the circular cylinder and from 2,400 to 43,900 for the sphere. However, the sphere autorotated readily

when the wind tunnel door was left open, which produced a non-uniform flow. In another test, the sphere was mounted partially in the boundary layer on the wind tunnel wall to produce a non-uniform flow, but the flow non-uniformity was not great enough to cause autorotation.

The sphere also autorotated when an obstruction was placed near the sphere. As the obstruction was brought near the sphere, the flow became faster through the gap. This increased the skin friction on the side nearest the obstruction and caused the sphere to autorotate with the surface nearest the obstruction moving downstream. The autorotation was the same when the obstruction was upstream or downstream from the axis of the sphere. However, the sphere rotated faster with the obstacle downstream from the axis of rotation. When the obstacle was downstream from the axis of rotation, it deflected the flow toward the sphere so that the flow separated further downstream on the side near the obstruction. Thus, a larger surface area on the sphere near the obstacle was subjected to appreciable skin friction. This increased the driving torque on the sphere.

If the obstacle had a semi-circular cut-out to match the sphere, and was brought very near it, the results were different. If the obstacle was well forward of the axis of the sphere, it blocked the flow sufficiently so that the total skin friction was greater on the

unobstructed side of the sphere. It then autorotated so that the unobstructed side moved downstream. However, if the obstacle was moved downstream, with the gap still small, the sphere stopped rotating, and then began to rotate with the side nearest the obstruction moving downstream as described above.

In another test, soap bubbles were blown into the air and given an initial rotation by twisting the bubble hoop as they were released. This rotation was always quickly damped with no evidence of autorotation. The range of Reynolds numbers was from 120 to 1400. Also, a ping-pong ball was mounted on needle bearings and tested with the axis normal and parallel to the free stream and also at a 45^{o} angle to it. None of these tests showed any evidence of autorotation, with the ball either smooth or roughened with small pieces of styrofoam.

C. DISCUSSION

Shortly after these tests, we learned that Sivier and Nicholls[21] tested spheres suspended magnetically in a vertical wind tunnel at Reynolds numbers from 40 to 5000 and for both rough and smooth spheres. These tests also showed no evidence of autorotation, except that a very rough sphere autorotated about an axis parallel to the flow with a Strouhal number of 0.002.

Hence, there is no evidence for autorotation of a sphere or circular cylinder for Reynolds numbers below 40,000. No tests were performed at higher Reynolds numbers. However, spherical weather balloons show no evidence of autorotation. These are usually initially in the super-critical range of Reynolds numbers and pass through the critical Reynolds number into the sub-critical range as they rise[13]. Therefore, it seems unlikely that a sphere will autorotate at any Reynolds number. However, it is still conceivable that a circular cylinder might autorotate at or above the critical Reynolds number.

XII. CONCLUSIONS

The primary objectives of the investigation were to determine the nature of the flow pattern over an autorotating wing and to measure the rotation rate and aerodynamic forces acting on it. These objectives were successfully met. The flow pattern was determined and the variation of the aerodynamic forces with angle of attack was successfully explained in terms of the flow pattern. The rotation rate was determined as a function of Reynolds number for a variety of airfoils, aspect ratios, I*, and tip plate configurations. The lift, drag and angular acceleration were measured as a function of Reynolds number for one configuration.

The following are the main conclusions from this investigation:

1. The flow pattern was quite different from the static case, with the flow separating at a much higher angle of attack and not attaching to the lower surface until well past zero angle of attack. When the wing stalled, there was a large vortex shed from the leading edge. The flow pattern was not studied for freely falling wings, but was probably similar.
2. The maximum lift and drag coefficients and the average drag coefficients were larger than for a conventional wing in steady flow. For fixed-axis autorotation, the peak lift coefficient

was 4. 50 at Re = 240,000, with an average lift coefficient of 2. 20. The peak drag coefficient was 4. 30 at Re = 240,000, with an average value of 1. 60. For freely falling wings, the peak lift and drag coefficients were not measured, but the average lift coefficients were about 15% higher than for fixed-axis autorotation, and the average drag coefficients were comparable.

3. The maximum lift to drag ratio for fixed-axis autorotation was 1. 45, while the maximum value for freely falling wings was 1. 68. Although some increase would result for higher aspect ratios or Reynolds numbers, it appears that an autorotating wing cannot produce lift to drag ratios greater than about two because a large drag is caused by the periodic vortices shed by the wing.

4. The angular acceleration of an autorotating wing, either freely falling or fixed-axis, was very low, and the wings with I* greater than about five rotated at nearly constant angular velocity.

5. For fixed-axis autorotation, the Strouhal number was strongly effected by the Reynolds number and approached a limiting value of 0. 35 asymptotically for sufficiently high Reynolds numbers. The values measured were comparable to previously

existing data. The Strouhal number was not studied in detail for freely falling wings, but was of the same order of magnitude.

6. In fixed-axis autorotation, the Strouhal number varied relatively little for different symmetrical airfoils, except for an airfoil with a sharp ridge at the mid-chord. For a nonsymmetrical, "S"-shaped airfoil, the Strouhal number was considerably increased, in either fixed-axis or freely falling autorotation, but the average lift and drag coefficients were almost unchanged in freely falling autorotation.
7. A certain minimum I* was required for a wing to autorotate; this value was higher for fixed-axis autorotation than for freely falling wings. For fixed-axis autorotation, the Strouhal number increased when I* was increased, and approached a limiting value asymptotically.
8. The aspect ratio had little effect on the Strouhal number for aspect ratios greater than three.
9. The Strouhal number was not too sensitive to tip plate size. However for low aspect ratios, it was much lower with no tip plates or non-rotating tip plates.
10. Fences mounted on the wing surface parallel to the span reduced the lift and Strouhal number except for one location on the wing, at which they increased the Strouhal number by 30%.

11. In fixed-axis autorotation, the Strouhal number and peak lift coefficient decreased rapidly when the retarding torque on the wing increased. The angular acceleration and peak drag coefficient also decreased but less rapidly.

12. The power that could be extracted from the air stream by an autorotating wing was considerably less than for a reasonably efficient windmill with a disk area equal to the wing area.

13. For sufficiently low Reynolds numbers, wings fell with a rocking motion without autorotating. For still lower Reynolds numbers, they fell in a stable manner without rocking or autorotating.

14. There was no evidence that either a sphere or circular cylinder would autorotate at sub-critical Reynolds numbers in a uniform flow.

APPENDIX

For comparison with the autorotation data, the static lift, drag, and pitching moment were measured for the 15% thick symmetrical airfoil (see Fig. 48-50). The results were comparable to those usually obtained for standard wing sections, except that the drag was higher. The lift increased approximately linearly up to the stall, with a maximum lift coefficient of 1.03 at $\alpha = 13.5^{o}$. The drag was probably higher below the stall than for a wing with a sharp trailing edge because the flow separated from the upper and lower surfaces ahead of the trailing edge. Also, the drag of the large tip plates was included in the drag. The pitching moment about c/4 remained constant at zero until the wing stalled, when it suddenly became negative.

REFERENCES

1. Ham, N. D., "Aerodynamic Loading of a Two-Dimensional Airfoil During Dynamic Stall," AIAAJ., Vol. 6, No. 10, October 1968, pp. 1927-1934.

2. Moore, F. K., "Lift Hysteresis at Stall as an Unsteady Boundary Layer Phenomenon," NACA TN 3571, October 1955.

3. Ahlborn, F., "Der Schwebflug und die Fallbewegung Ebener Tafeln in der Luft," Abh. d Naturw. Ver., Hamburg, Vol. XV, 1897.

4. Ahlborn, F., "The Magnus Effect in Theory and Reality," NACA TM 567, May 1930.

5. Crabtree, L. F., "The Rotating Flap as a High Lift Device," Royal Aircraft Estab., TN Aero 2492, April 1957.

6. Coles, D., "Tumbling Airfoil," unpublished student project, Graduate Aeronautical Laboratory, California Institute of Technology, 1957.

7. Bustamante, A. C. and Stone, G. W., "The Autorotation Characteristics of Various Shapes for Subsonic and Hypersonic Flows," AIAA Paper 69-132, presented at AIAA 7th Aerospace Sciences Meeting, January 1969.

8. Laub, J. H. . "Externally Pressurized Journal Bearings," CIT JPL 30-14, Graduate Aeronautical Laboratory, California Institute of Technology, November 1959.

9. Grossam, N. S. and Powell, J. W. (ed), Gas Lubricated Bearings, Butterworths Scientific Publications, London, 1964, pp. 158-160.

10. Gross, W. A., Gas Film Lubrication, John Wiley and Sons, Inc., New York, 1962, pp. 374-376.

11. Maskell, E. C., "A Theory of the Blockage Effects on Bluff Bodies and Stalled Wings in a Closed Wind Tunnel," British ARC RM No. 3400, 1963.

12. Hoerner, S. F., Fluid Dynamic Drag, published by author, 148 Busteed Drive, Midland Park, New Jersey, 1965, pp. 3-16, 4-3, 6-6, 7-10.

13. Pope, A. and Harper, J., Low Speed Wind Tunnel Testing, John Wiley and Sons, Inc., New York, 1966, pp. 326-332.

14. Roos, F. W. and Willmarth, W. W., "An Experimental Investigation of the Unsteady Flows about Spheres and Disks, "University of Michigan Report No. 01954-1-T, December 1968; also Ph. D. thesis, The University of Michigan, 1968.

15. Schlicting, H., Boundary Layer Theory, McGraw-Hill Book Co., New York, 1968, p. 9.

16. Roos, F. W. and Willmarth, W. W., unpublished data, The University of Michigan, 1968.

17. Milne-Thomson, L. M., Theoretical Hydrodynamics, MacMillan and Co., Ltd., 1938, pp. 341-348.

18. Marks, L. S., Mechanical Engineer's Handbook, 4th Ed., McGraw-Hill Book Co., New York, 1941, p. 1133.

19. Willmarth, W. W., Hawk, N. E., and Harvey, R. L., "Steady and Unsteady Motions and Wakes of Freely Falling Disks," Phys. of Fluids, Vol. 7, No. 2, February 1964, pp. 197-208.

20. Prandtl, L., "Application of the Magnus Effect to the Wind Propulsion of Ships," NACA TM 367, June 1926.

21. Sivier, K. R. and Nicholls, J. A., "Subsonic Sphere Drag Measurements at Intermediate Reynolds Numbers," NASA CR 1392, 1969.

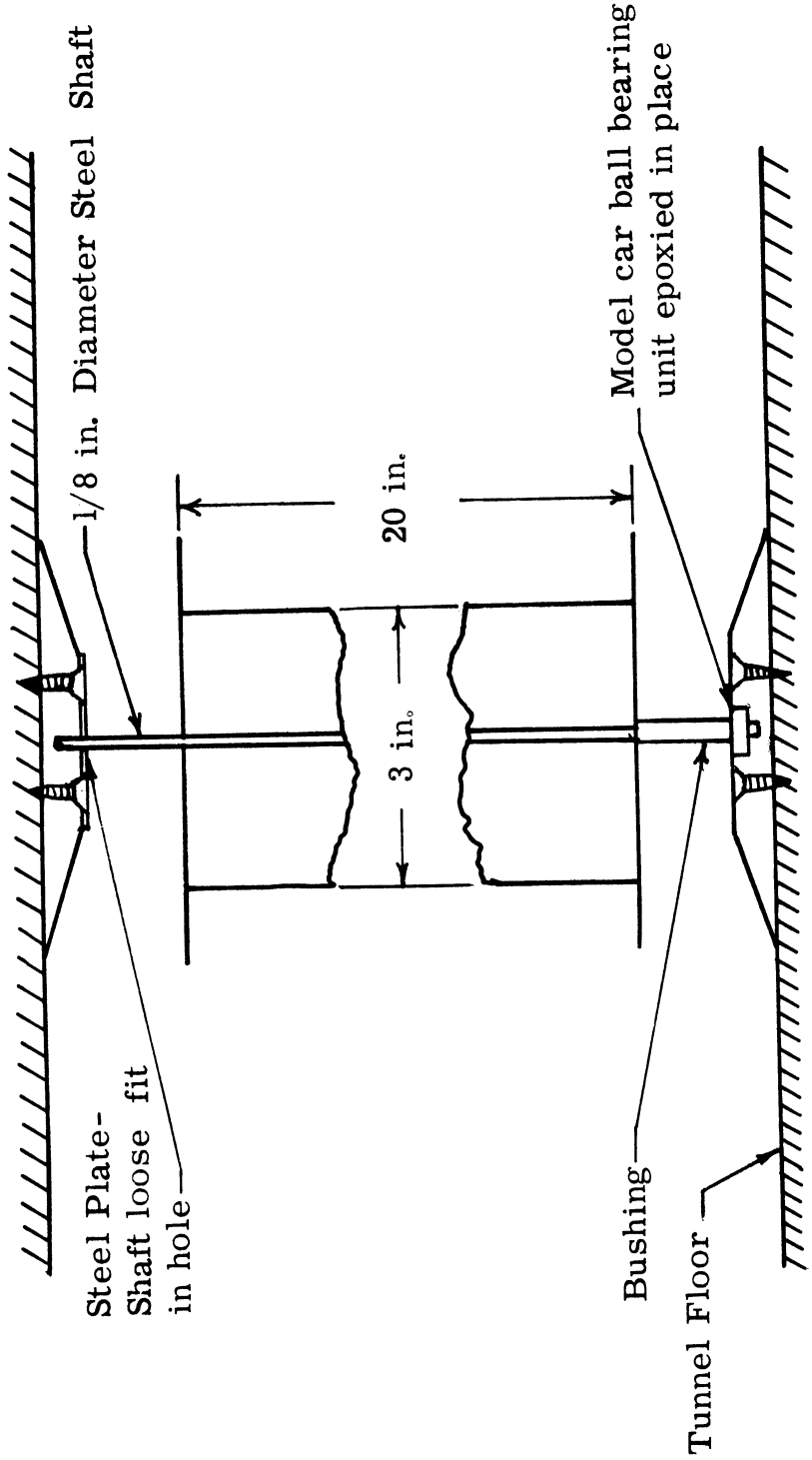

Figure 1. Ball Bearing System for Small Wings.

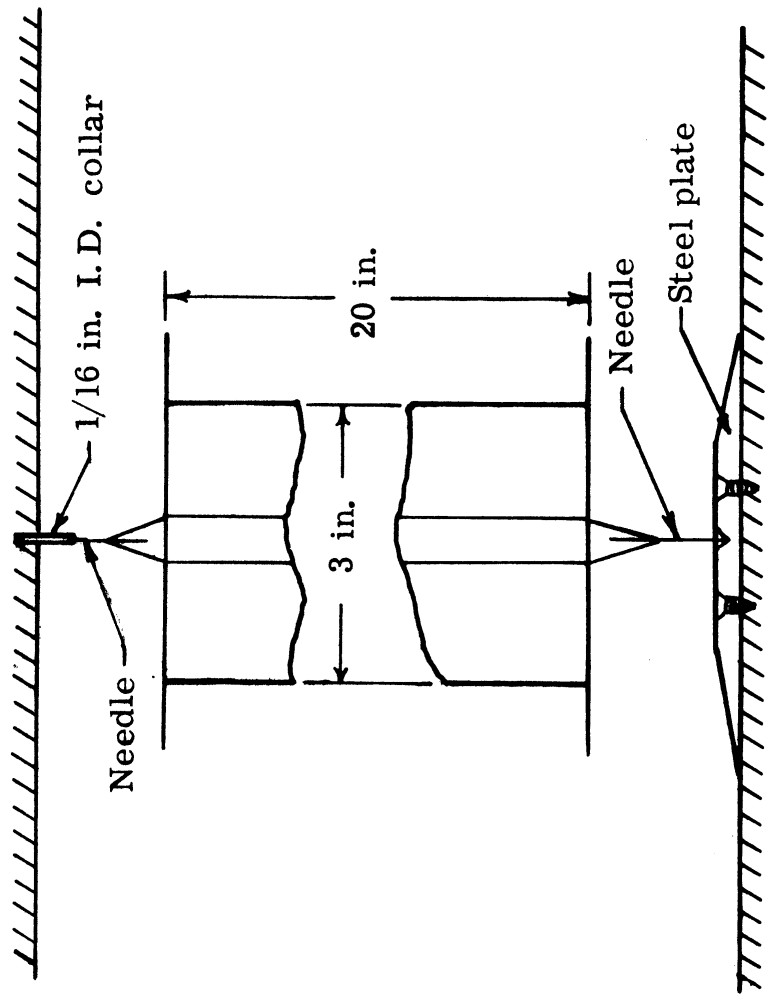

Figure 2. Needle Bearing System for Small Wings.

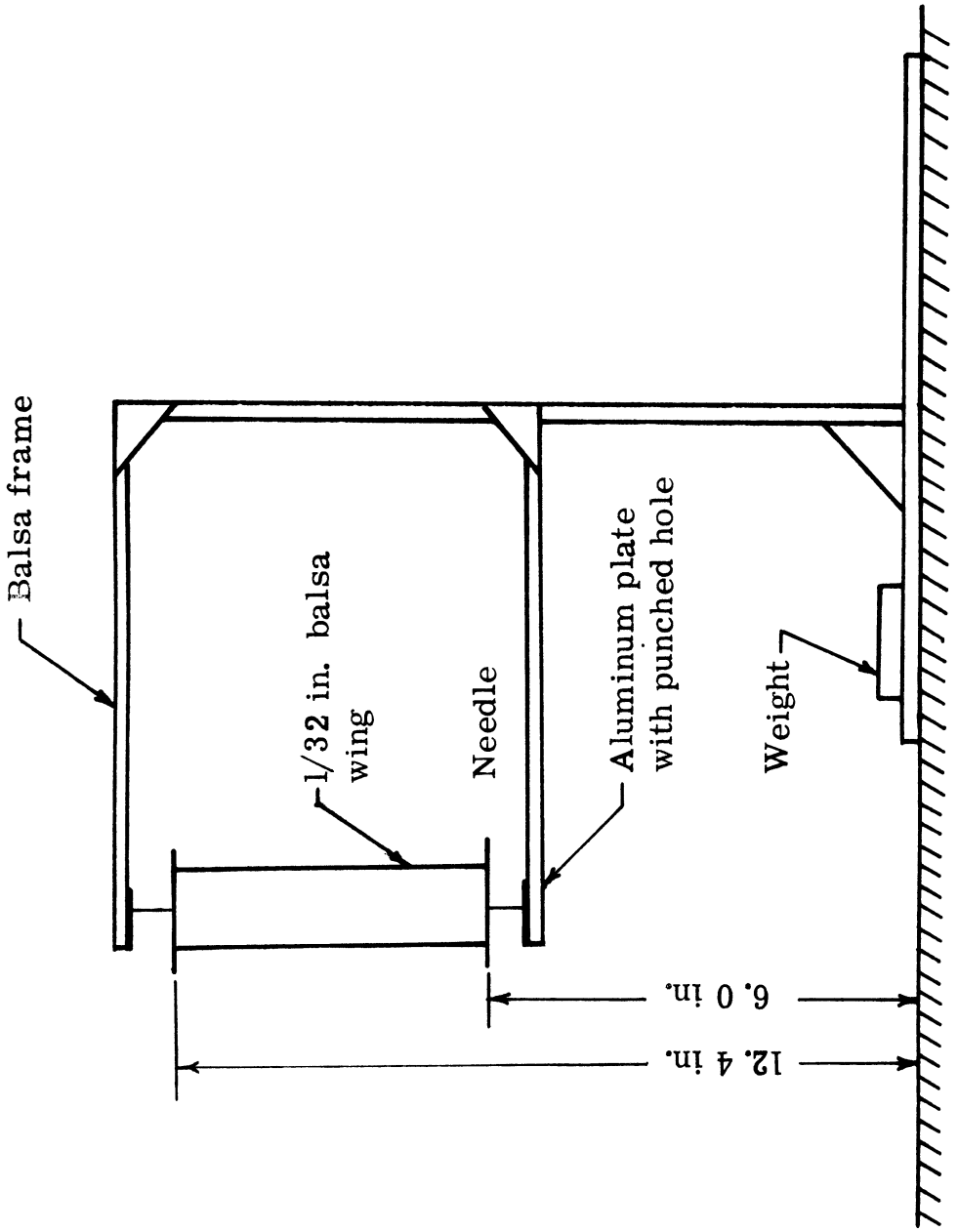

Figure 3. Wing for Reynolds Numbers Below 1500.

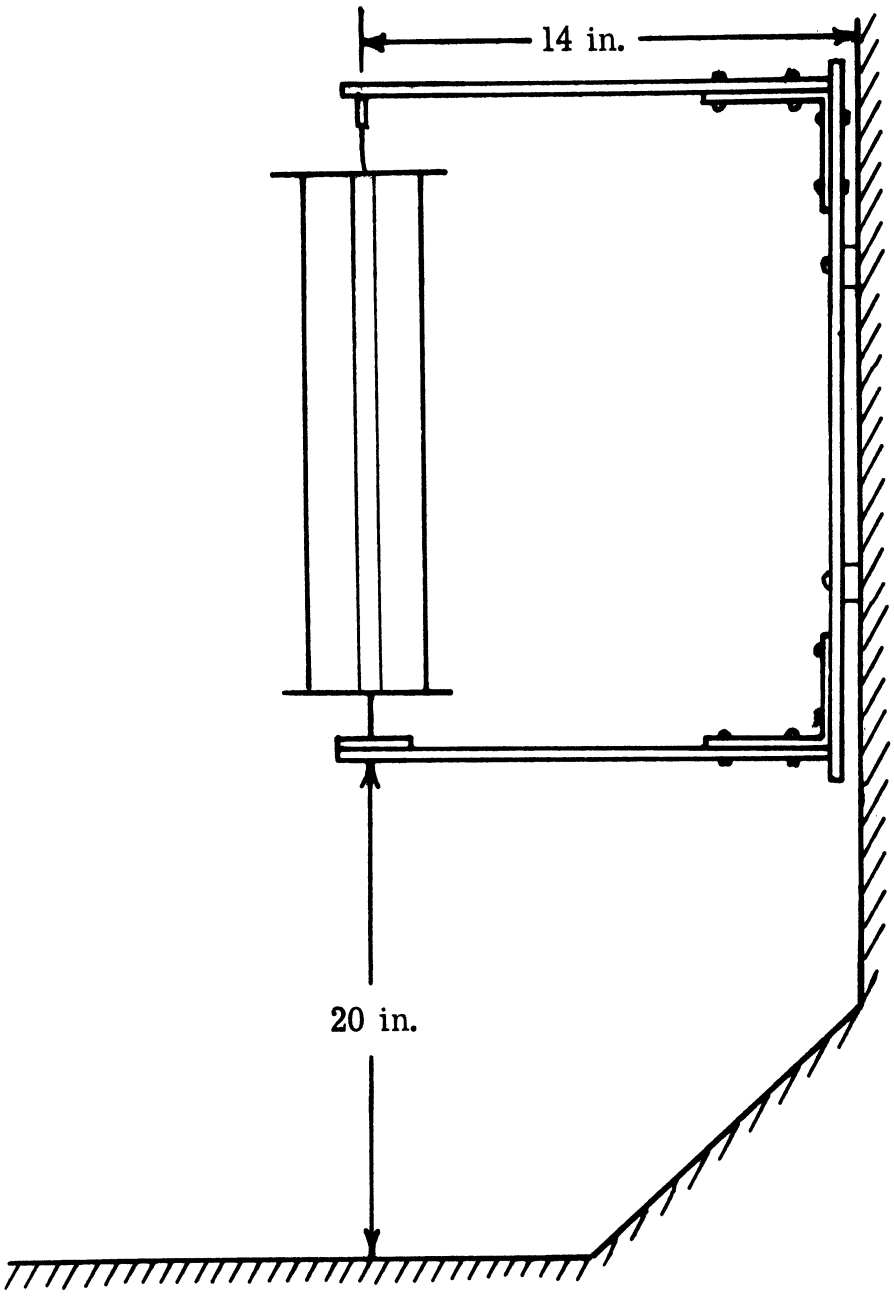

Figure 4. Small Wing Installation in 5 x 7 ft Tunnel.

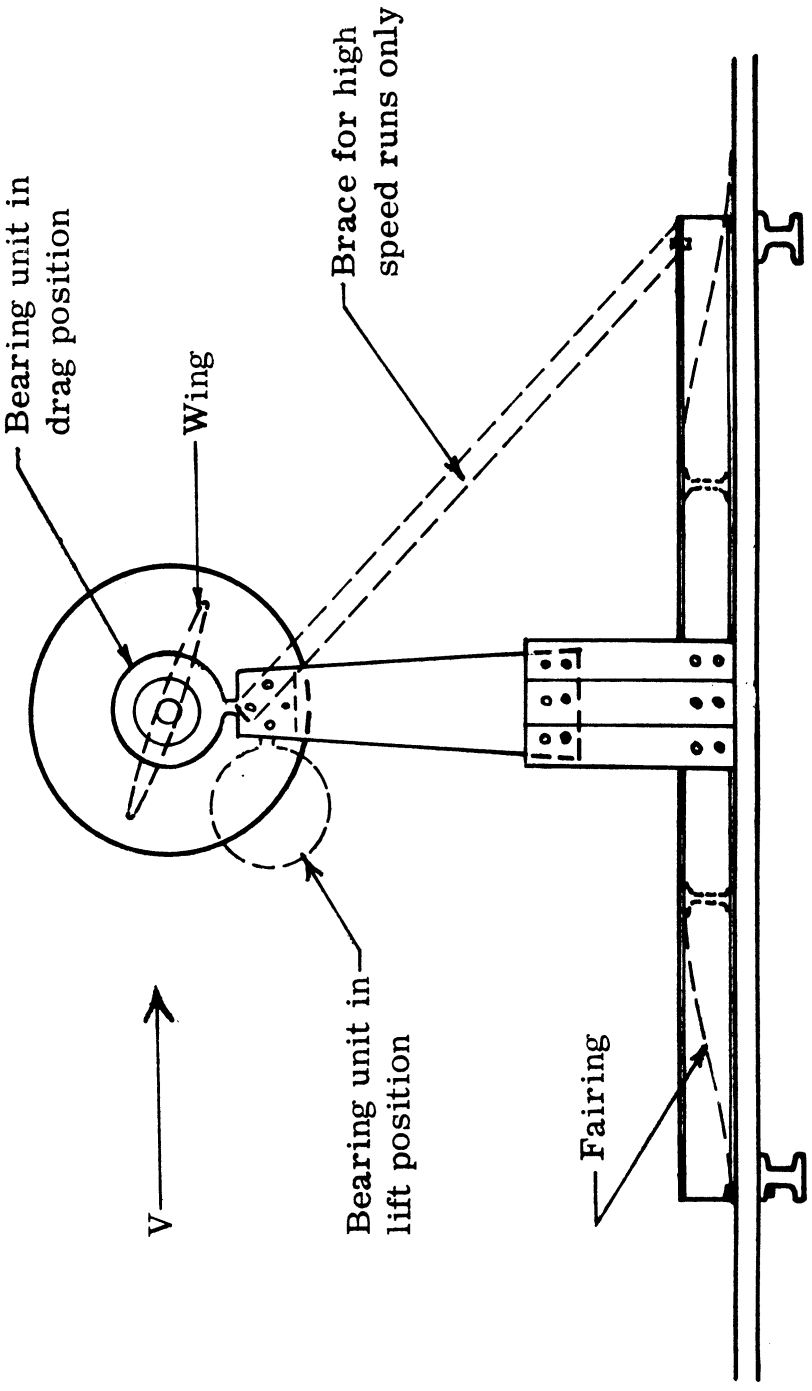

Figure 5. Instrumented Wing Apparatus in 5 x 7 ft Tunnel.

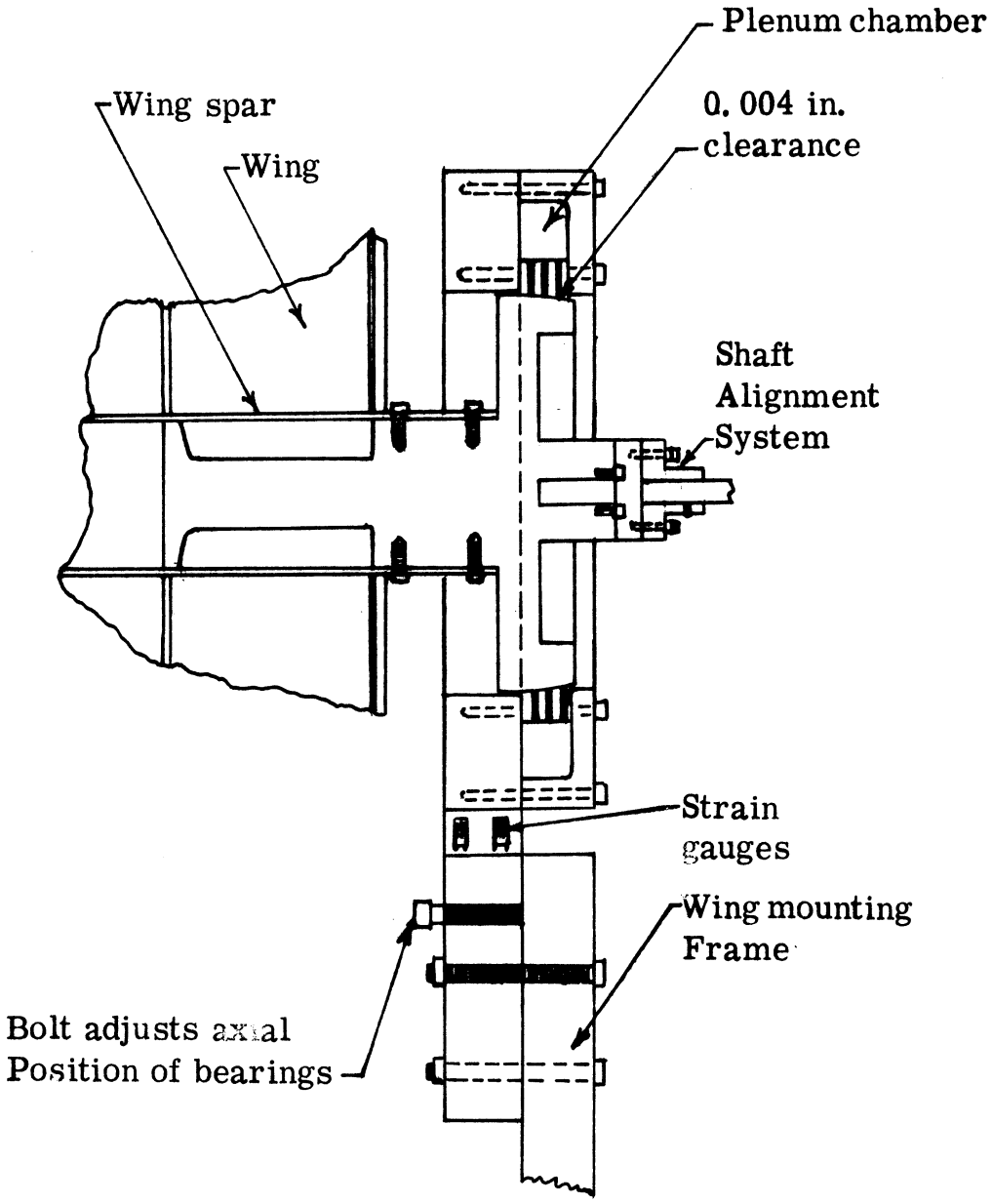

Figure 6. Air Bearing System.

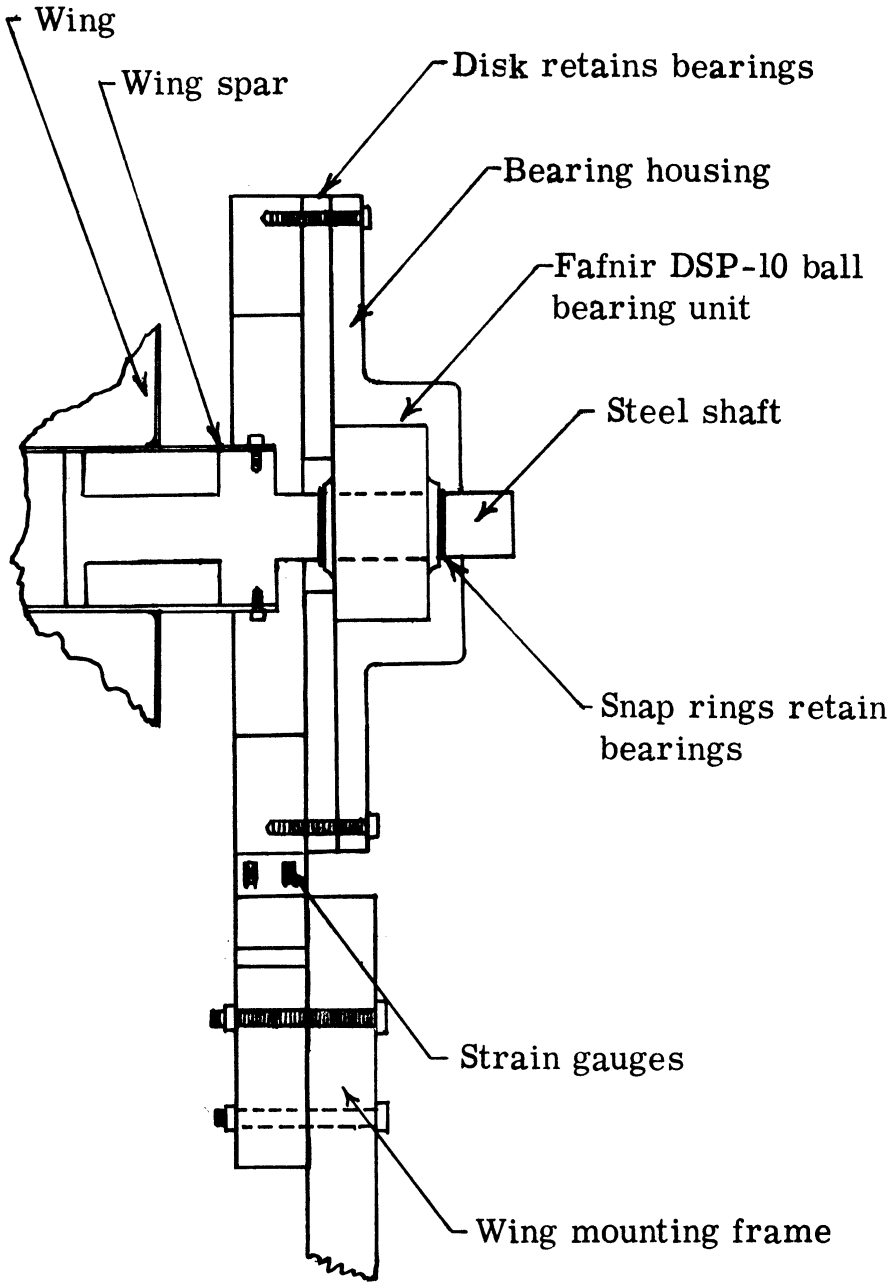

Figure 7. Mechanical Bearing System.

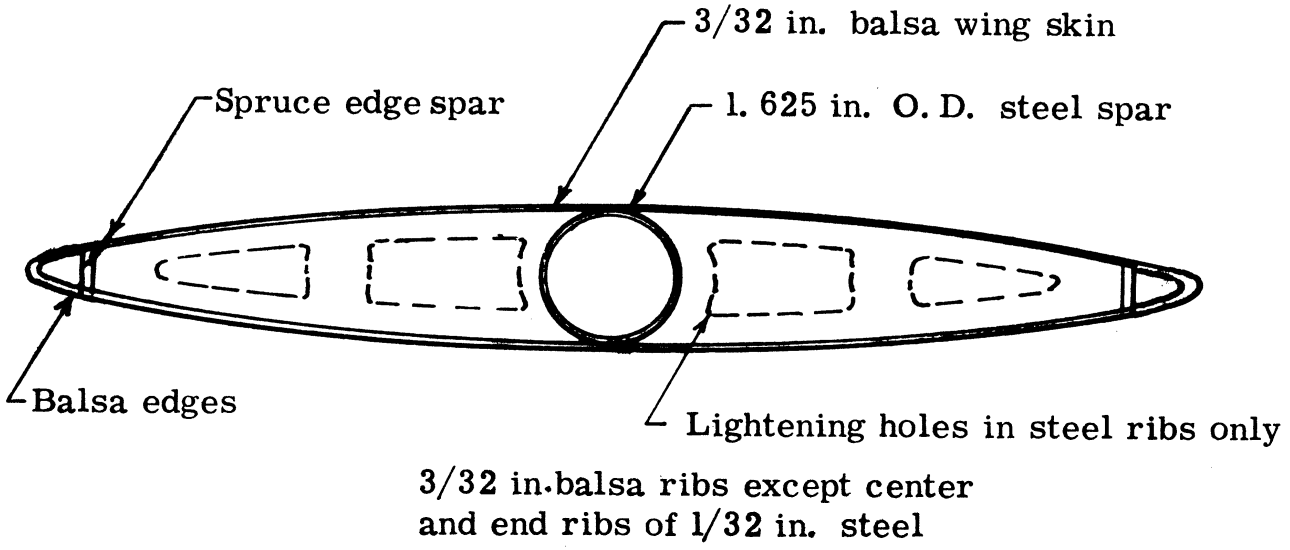

Figure 8. Construction of Instrumented Wing.

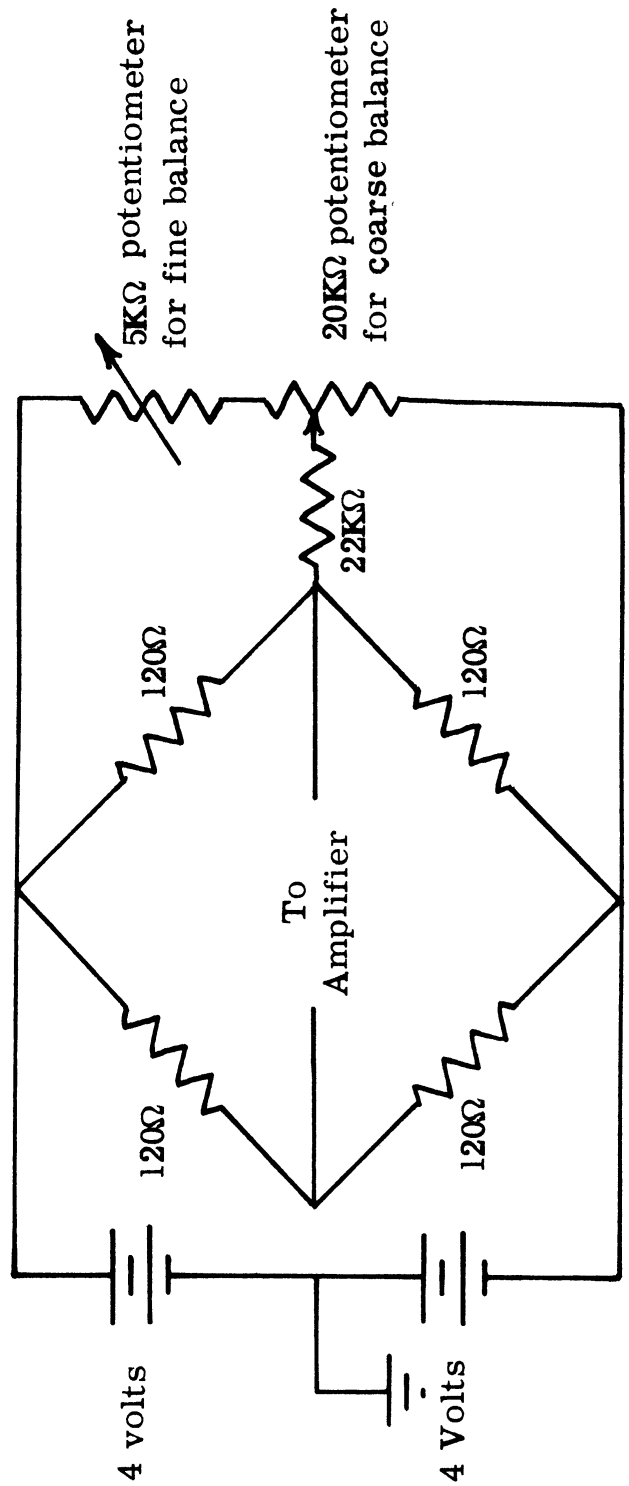

Figure 9. Strain Gauge Circuit.

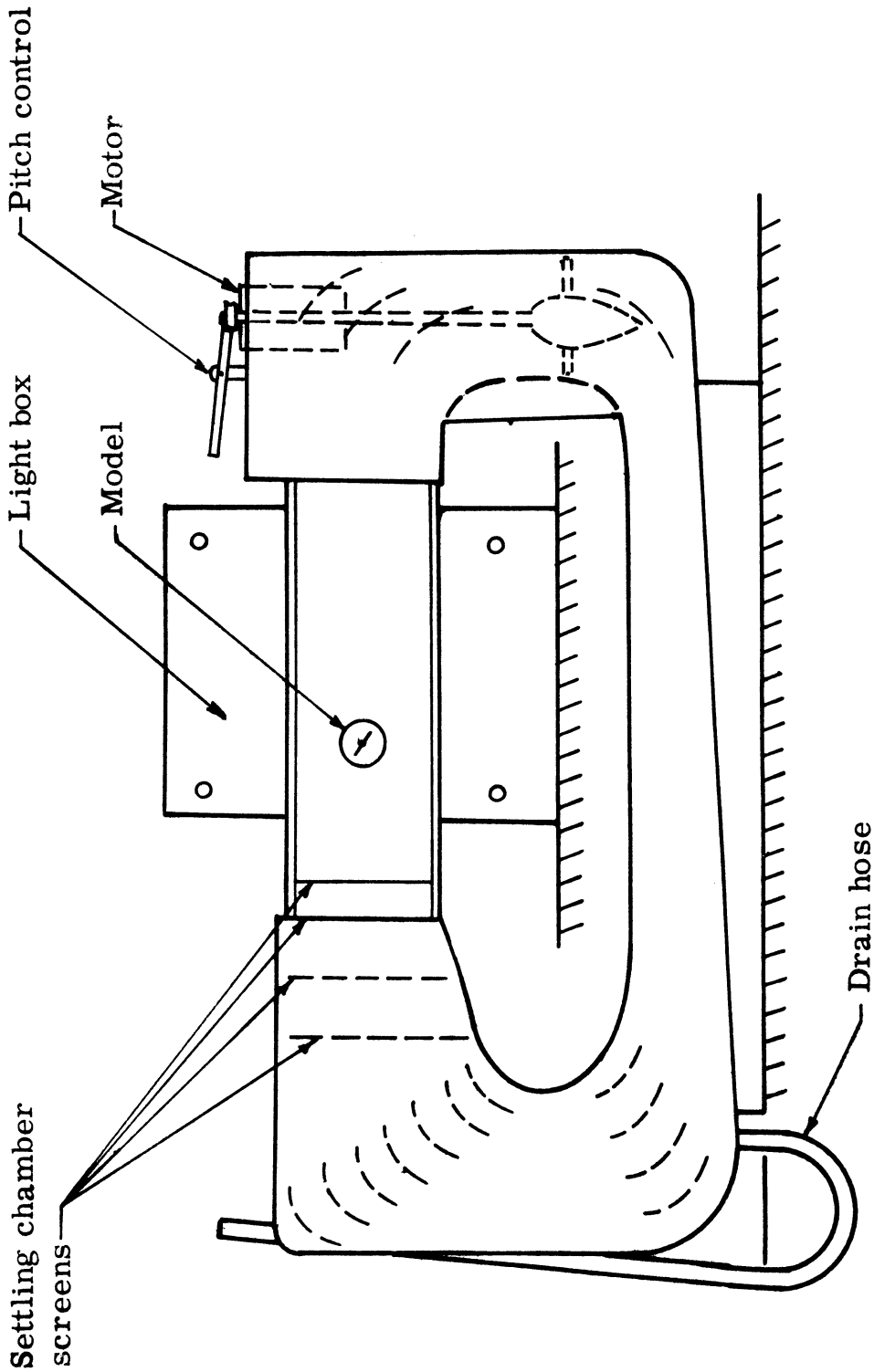

Figure 10. Wallis Water Tunnel.

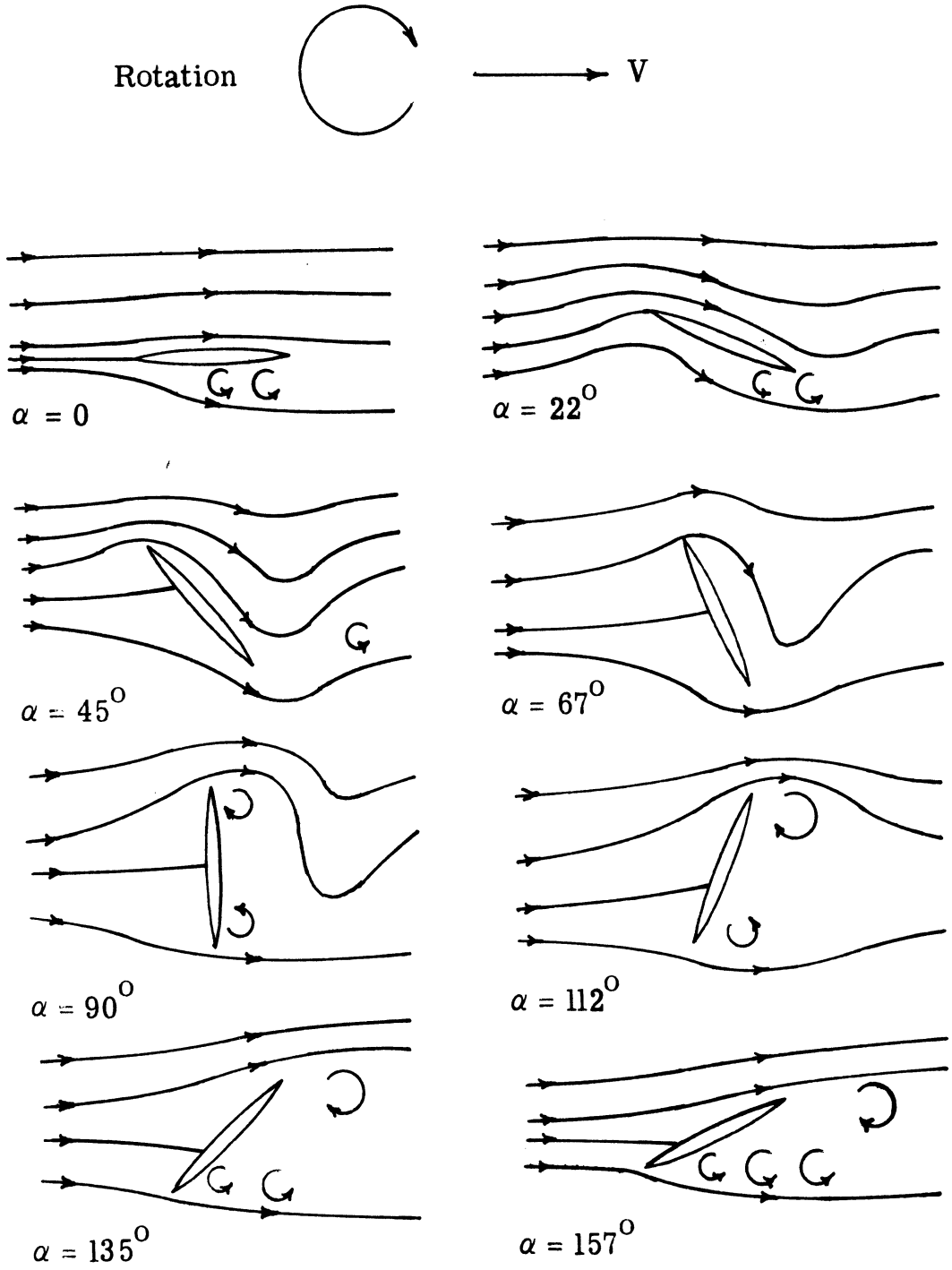

Figure 11. Flow Pattern Over Autorotating Wing at Re = 90,000.

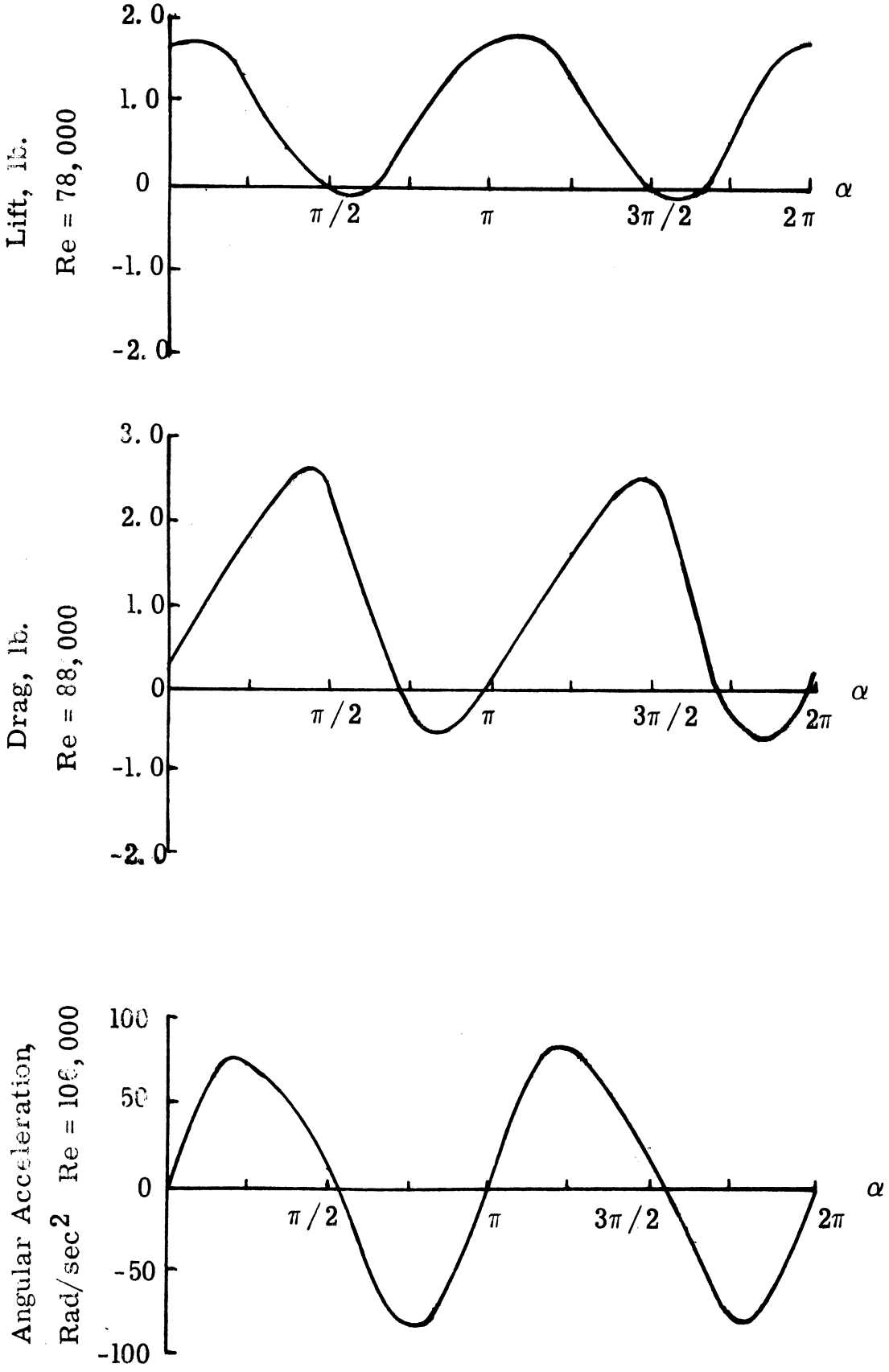

Figure 12. Aerodynamic Forces vs Angle of Attack on Auto-rotating Wing.

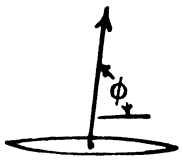

$\ell = 0$
$\phi = 81^{o}$
$\alpha = 0$

$\ell = 0.066c$
$\phi = 68^{o}$
$\alpha = 15^{o}$

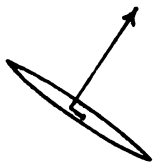

$\ell = 0.116c$
$\phi = 58^{o}$
$\alpha = 30^{o}$

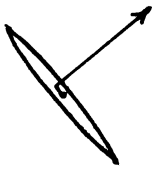

$\ell = 0.115c$
$\phi = 43^{o}$
$\alpha = 45^{o}$

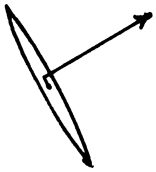

$\ell = 0.107c$
$\phi = 34^{o}$
$\alpha = 60^{o}$

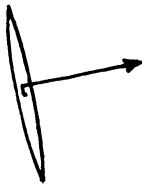

$\ell = 0.073c$
$\phi = 10^{o}$
$\alpha = 75^{o}$

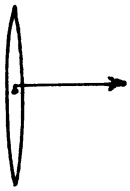

$\ell = 0.015c$
$\phi = 0$
$\alpha = 90^{o}$

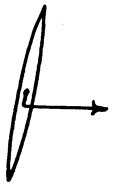

$\ell = -0.042c$
$\phi = -5.7^{o}$
$\alpha = 105^{o}$

$\ell = -0.843c$
$\phi = 22^{o}$
$\alpha = 120^{o}$

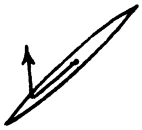

$\ell = -0.323c$
$\phi = 109^{o}$
$\alpha = 135^{o}$

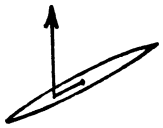

$\ell = -0.162c$
$\phi = 110^{o}$
$\alpha = 150^{o}$

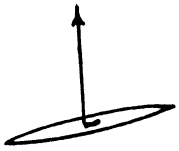

$\ell = -0.066c$
$\phi = 105^{o}$
$\alpha = 165^{o}$

Figure 13. Diagram of Resultant Force on Autorotating Wing at Re = 100,000.

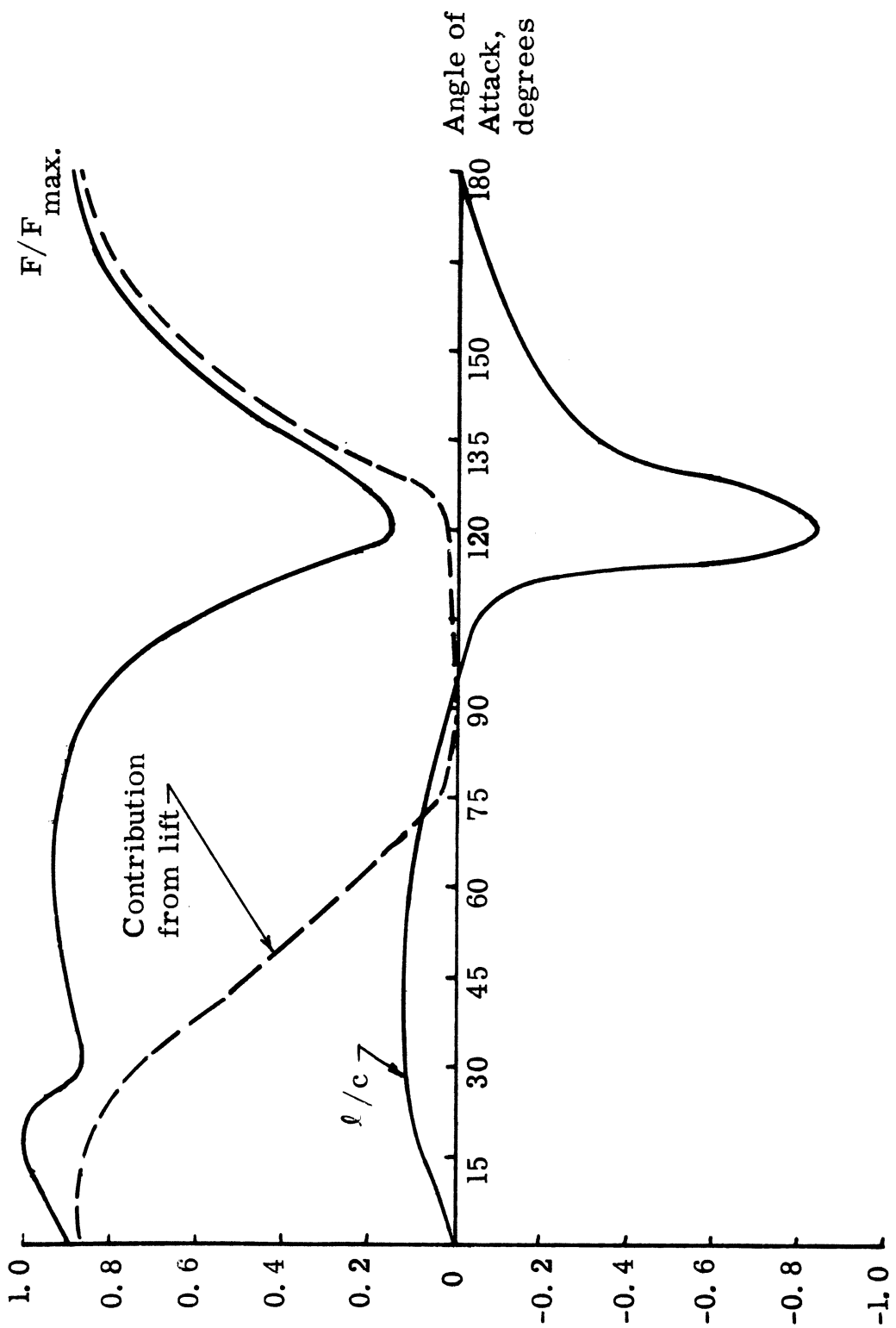

Figure 14. Resultant Force and Center of Pressure Location on Autorotating Wing at Re = 100,000.

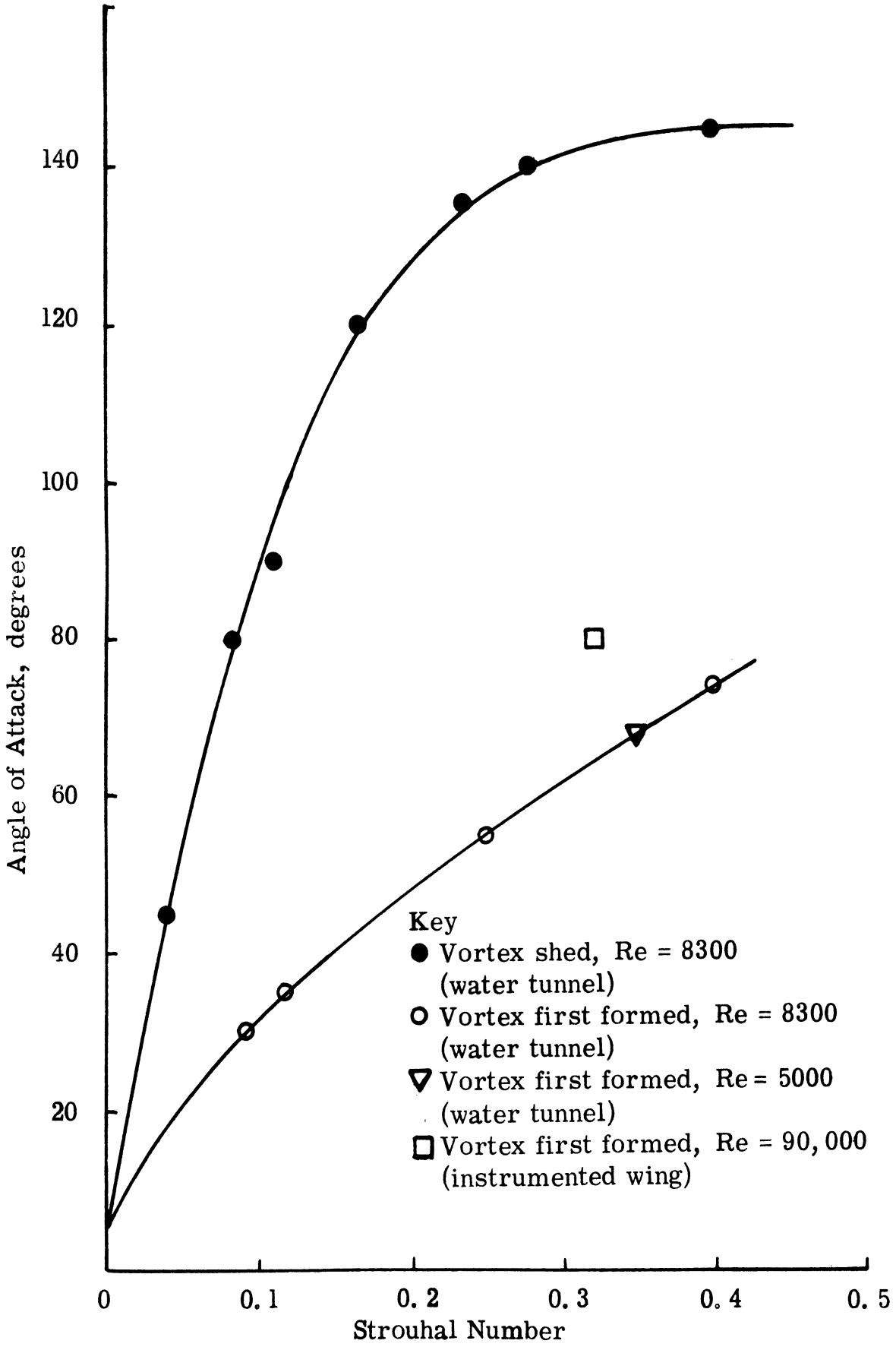

Figure 15. Stalling Angle vs Strouhal Number for Autorotating Wing.

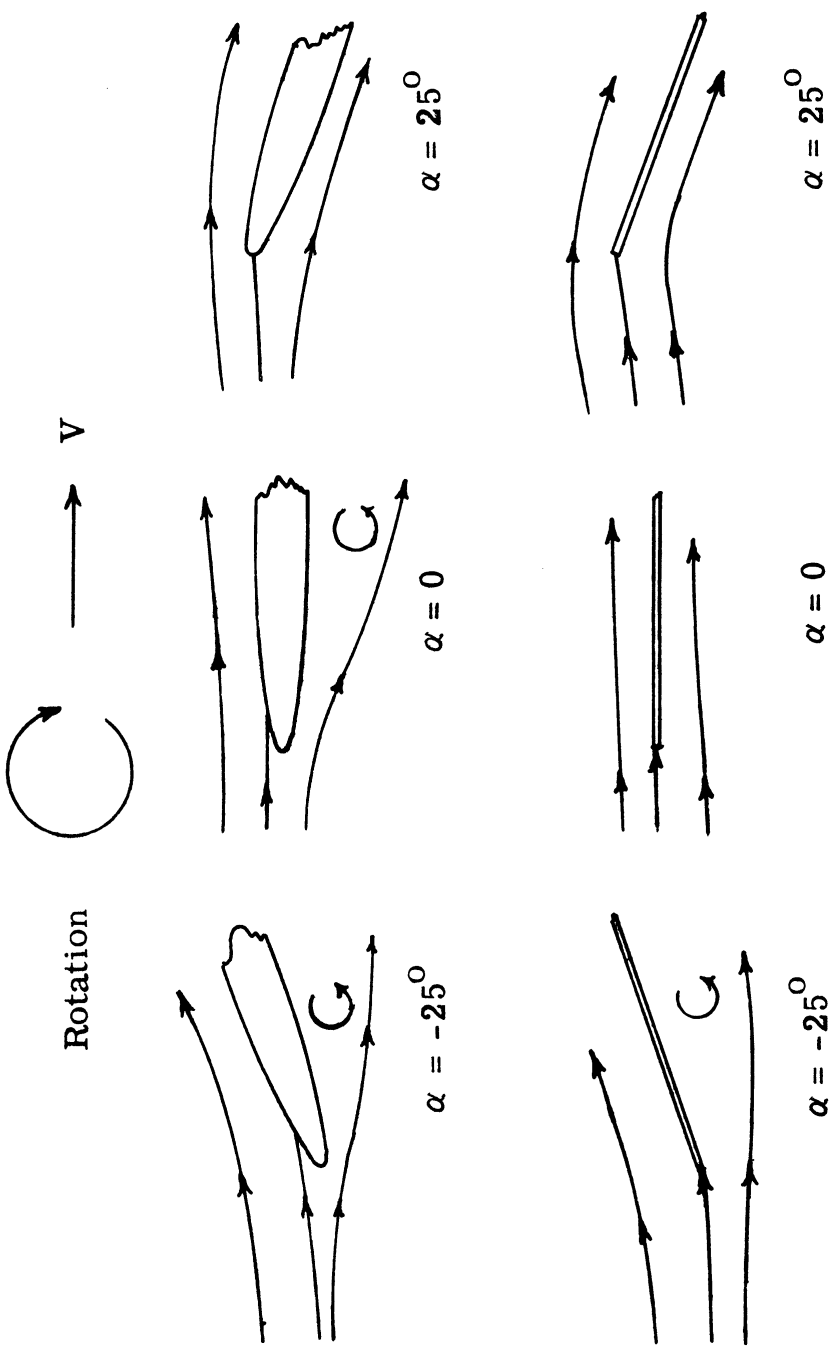

Figure 16. Flow Pattern Near Leading Edge for Flat Plate and Elliptical Airfoil.

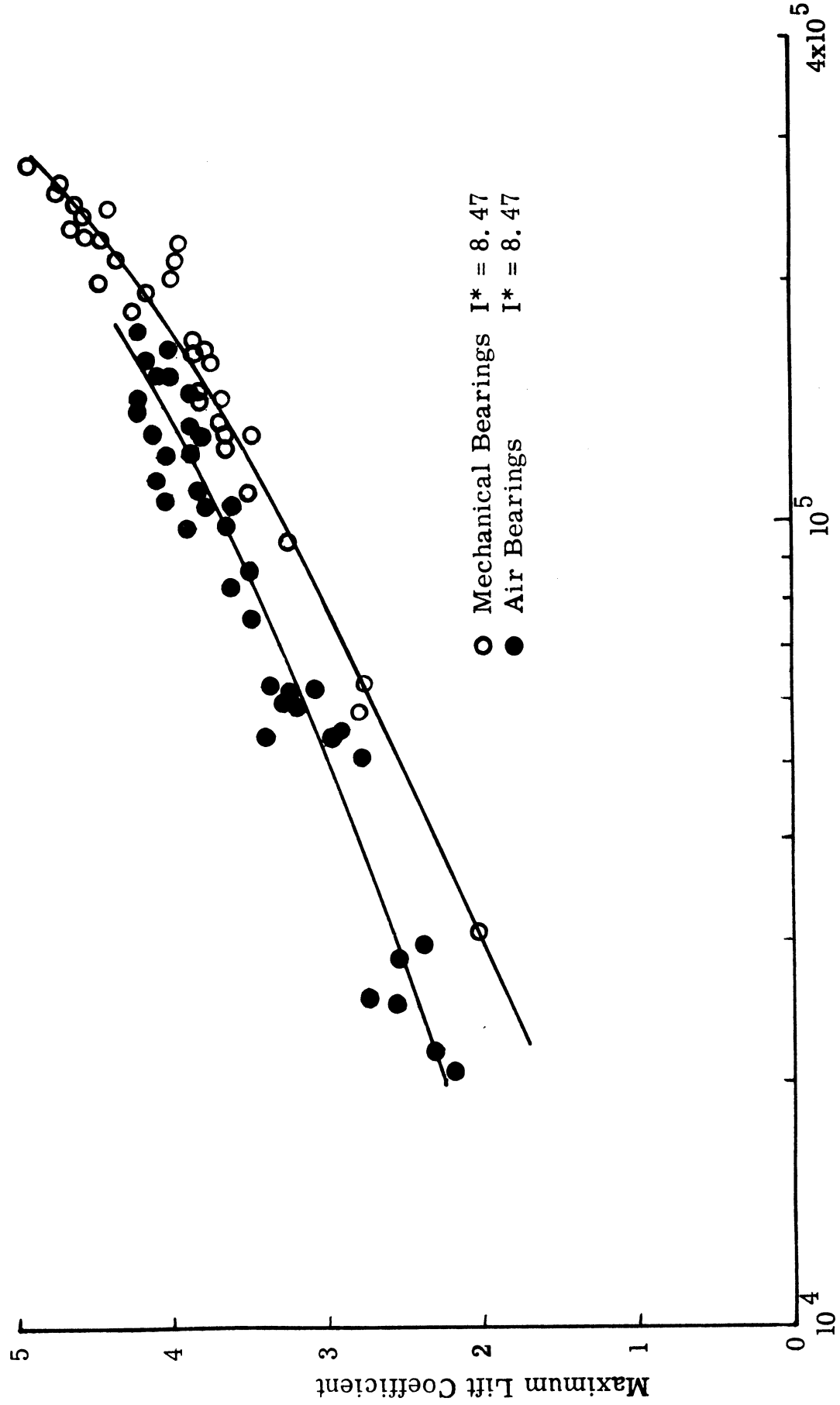

Figure 17. Maximum Lift Coefficient vs Reynolds Number.

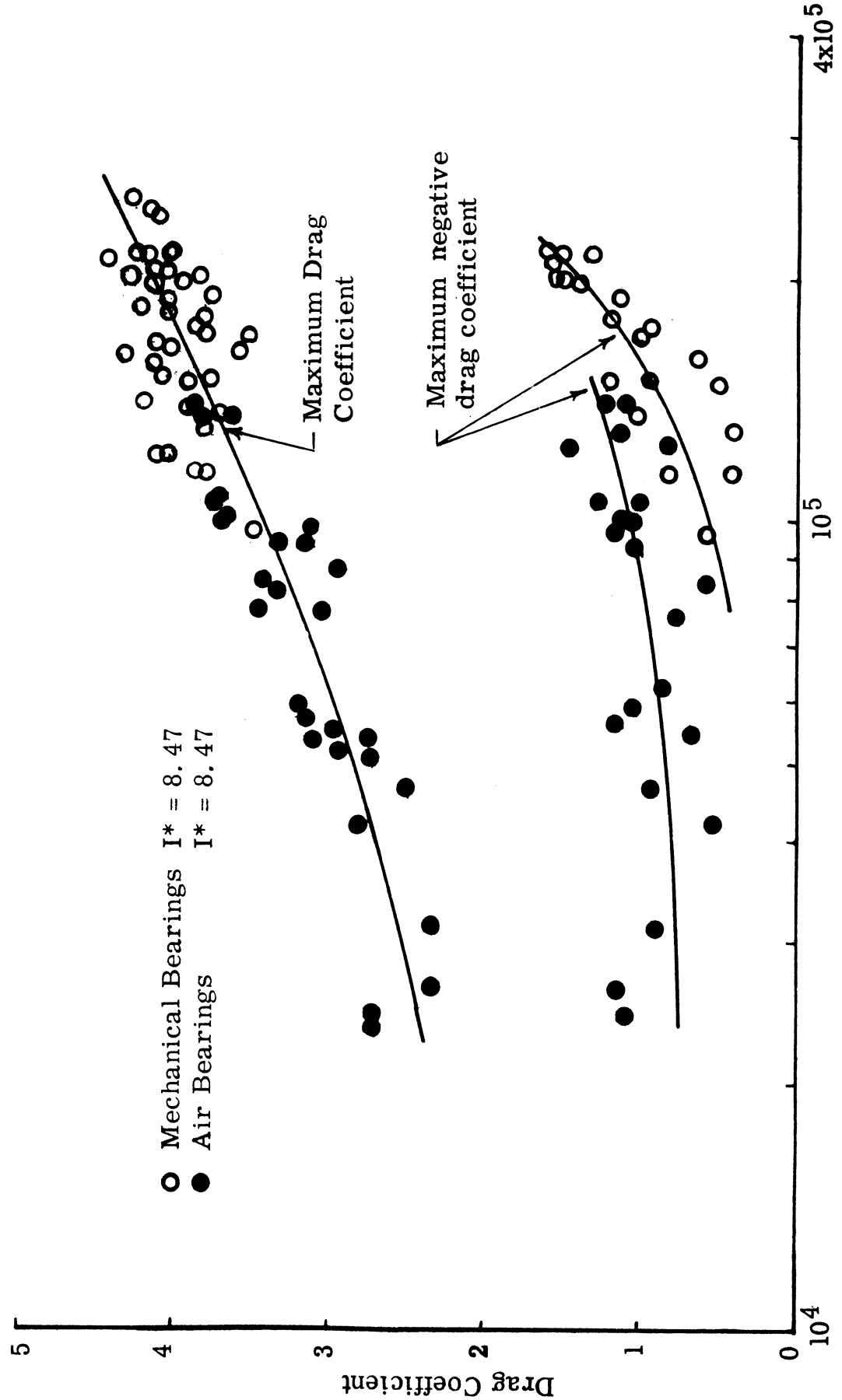

Figure 18. Maximum and Minimum Drag Coefficient vs Reynolds Number.

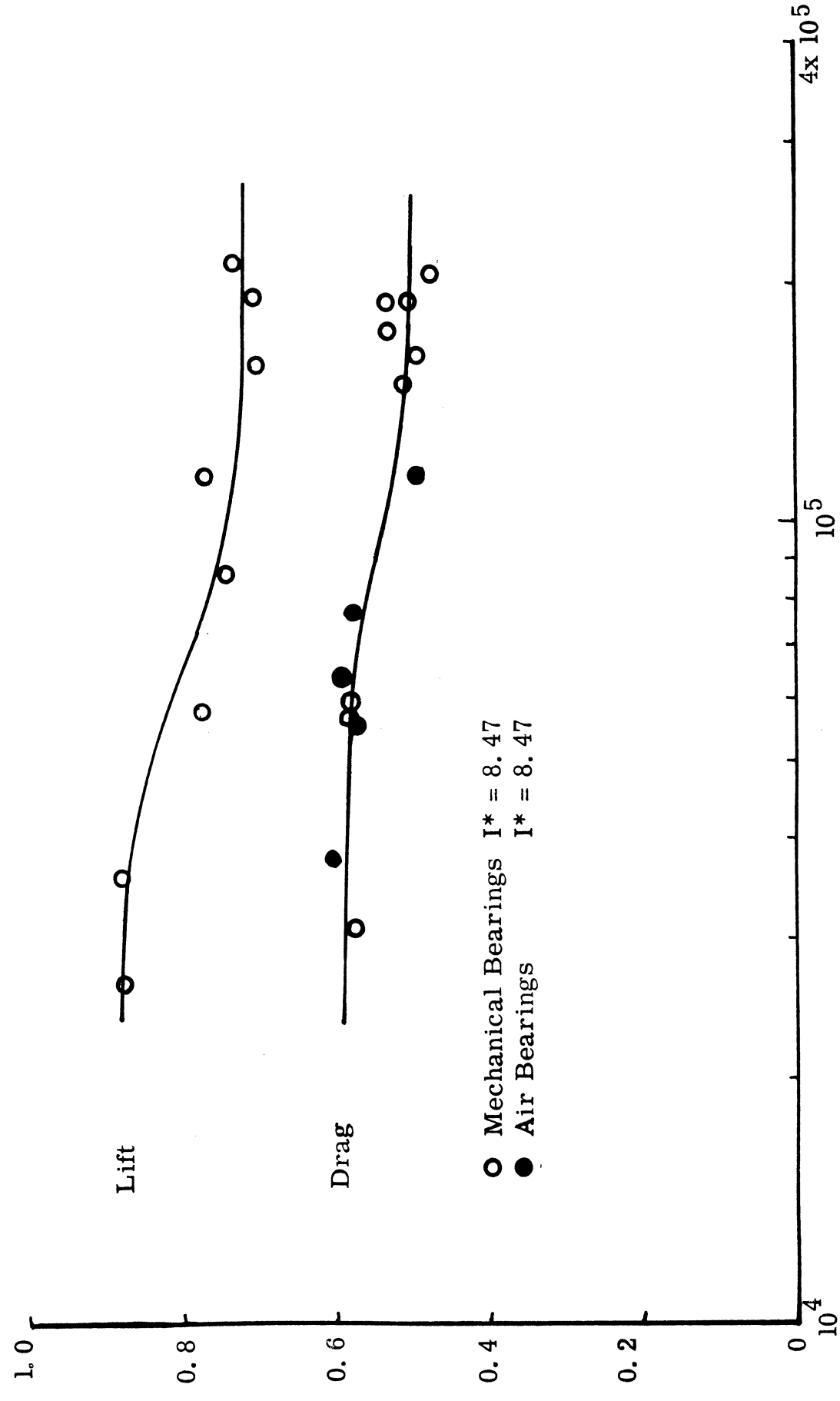

Figure 19. Ratio of Average Lift and Drag to Maximum Lift and Drag.

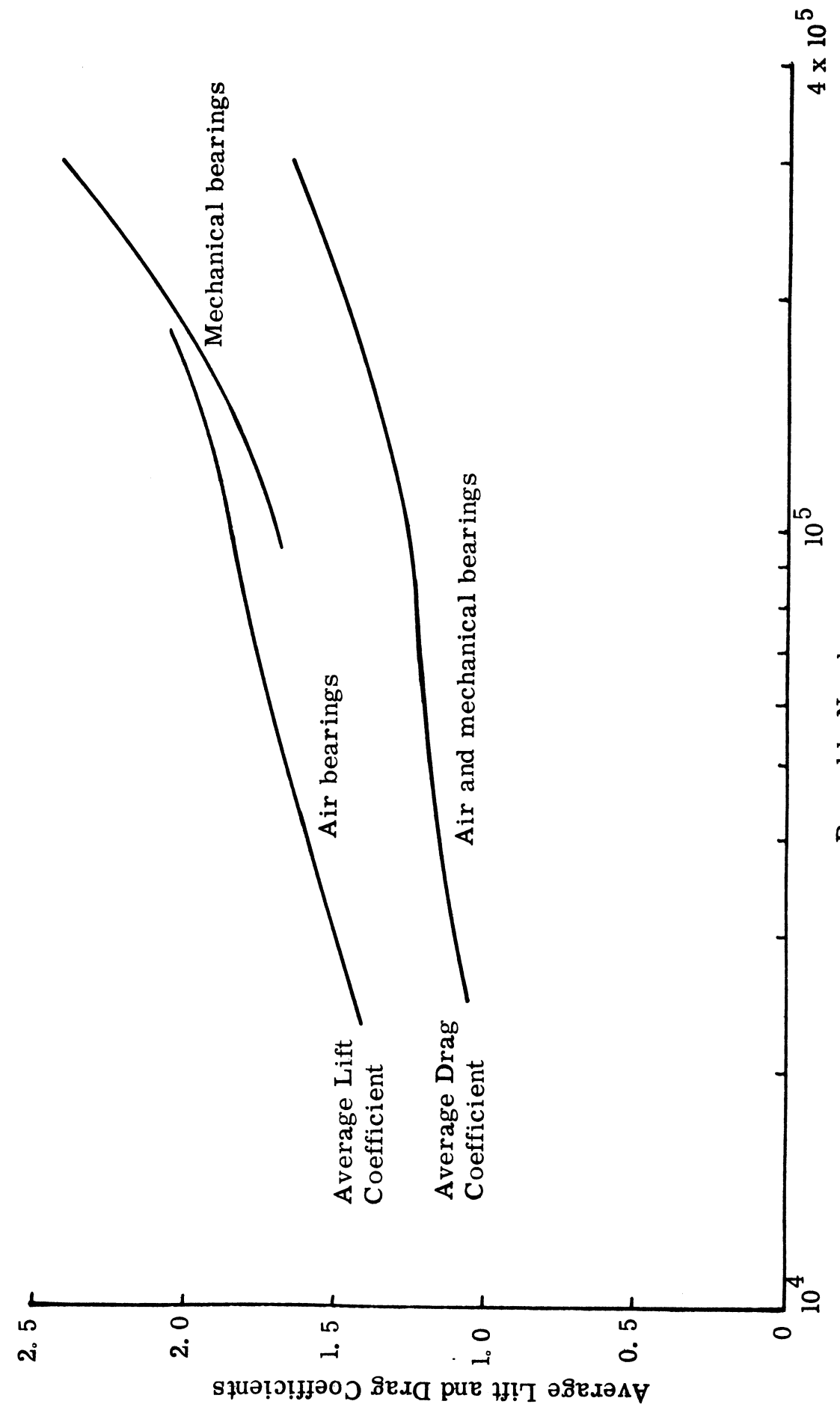

Figure 20. Average Lift and Drag Coefficients vs Reynolds Number.

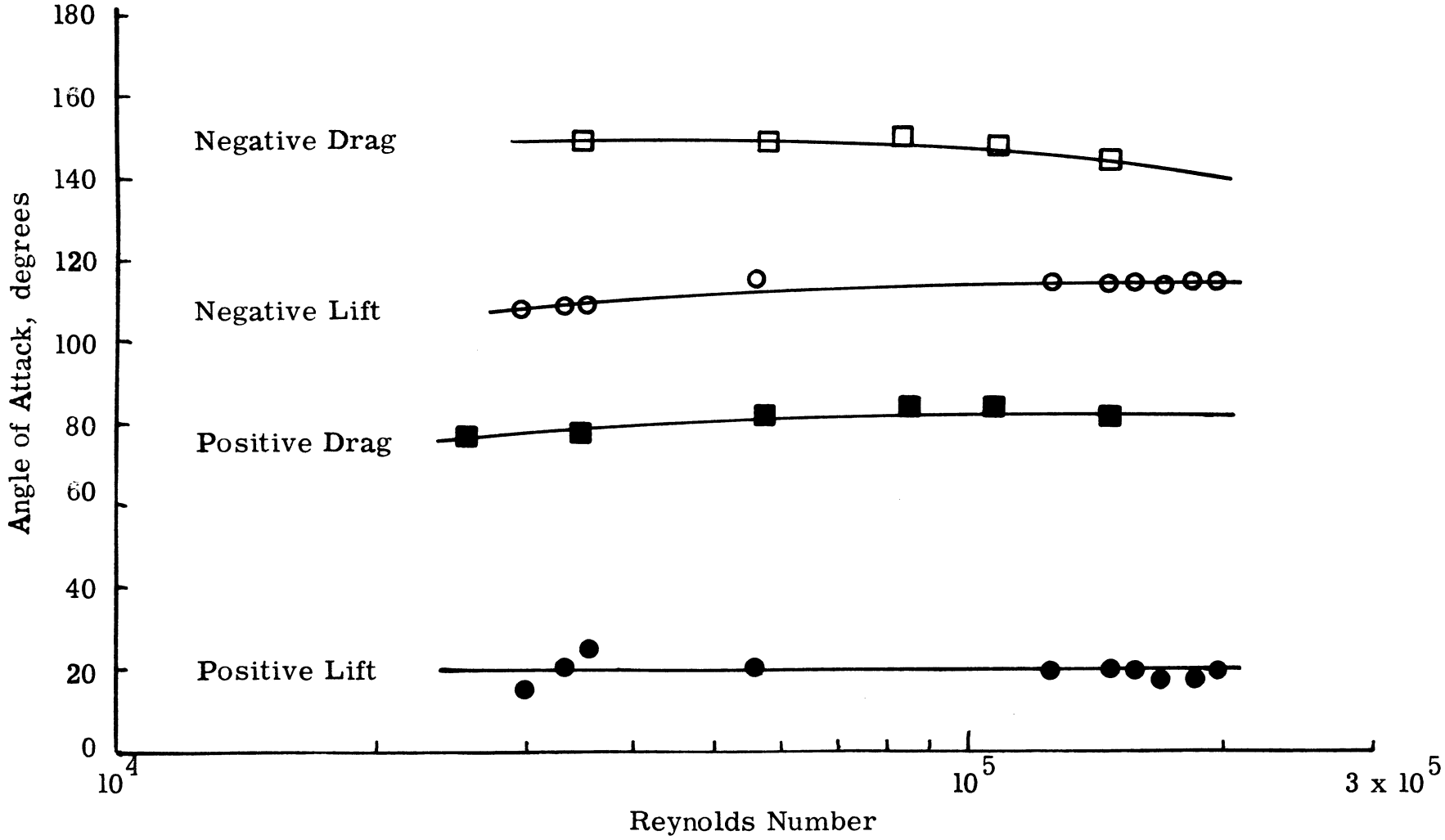

Figure 21. Location of Maximum and Minimum Lift and Drag Points.

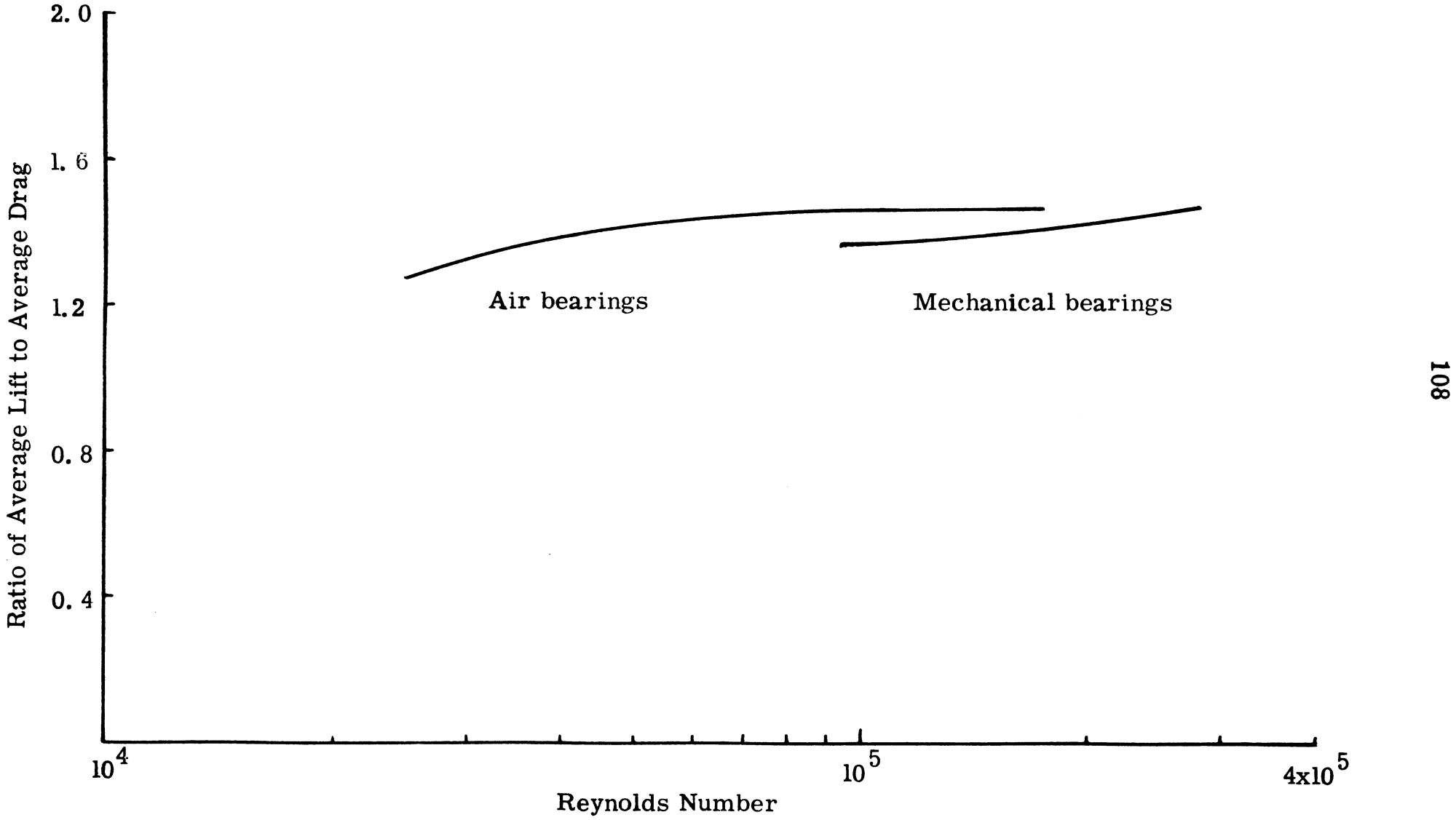

Figure 22. Ratio of Average Lift to Average Drag vs Reynolds Number

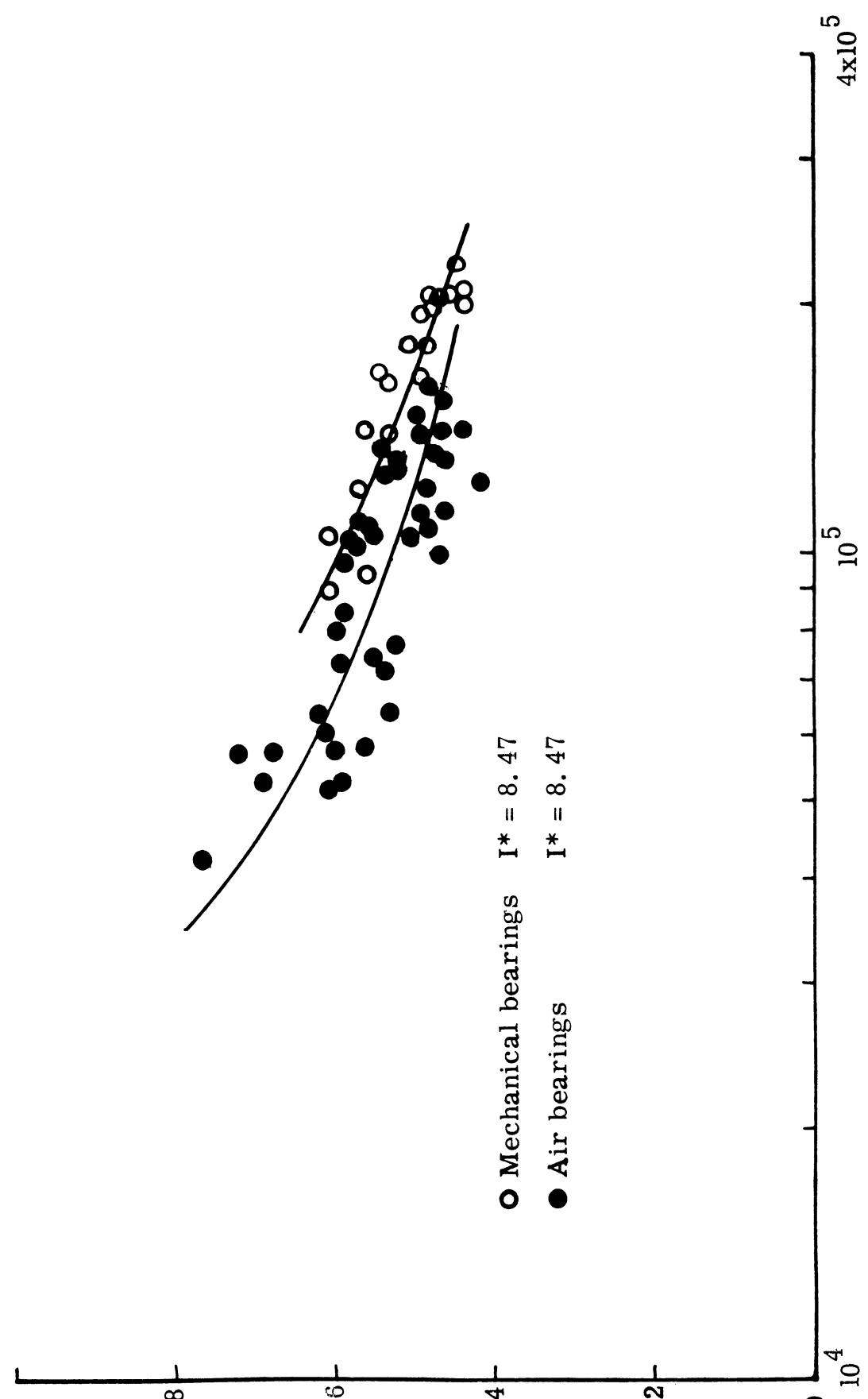

Figure 23. Maximum Angular Acceleration vs Reynolds Number.

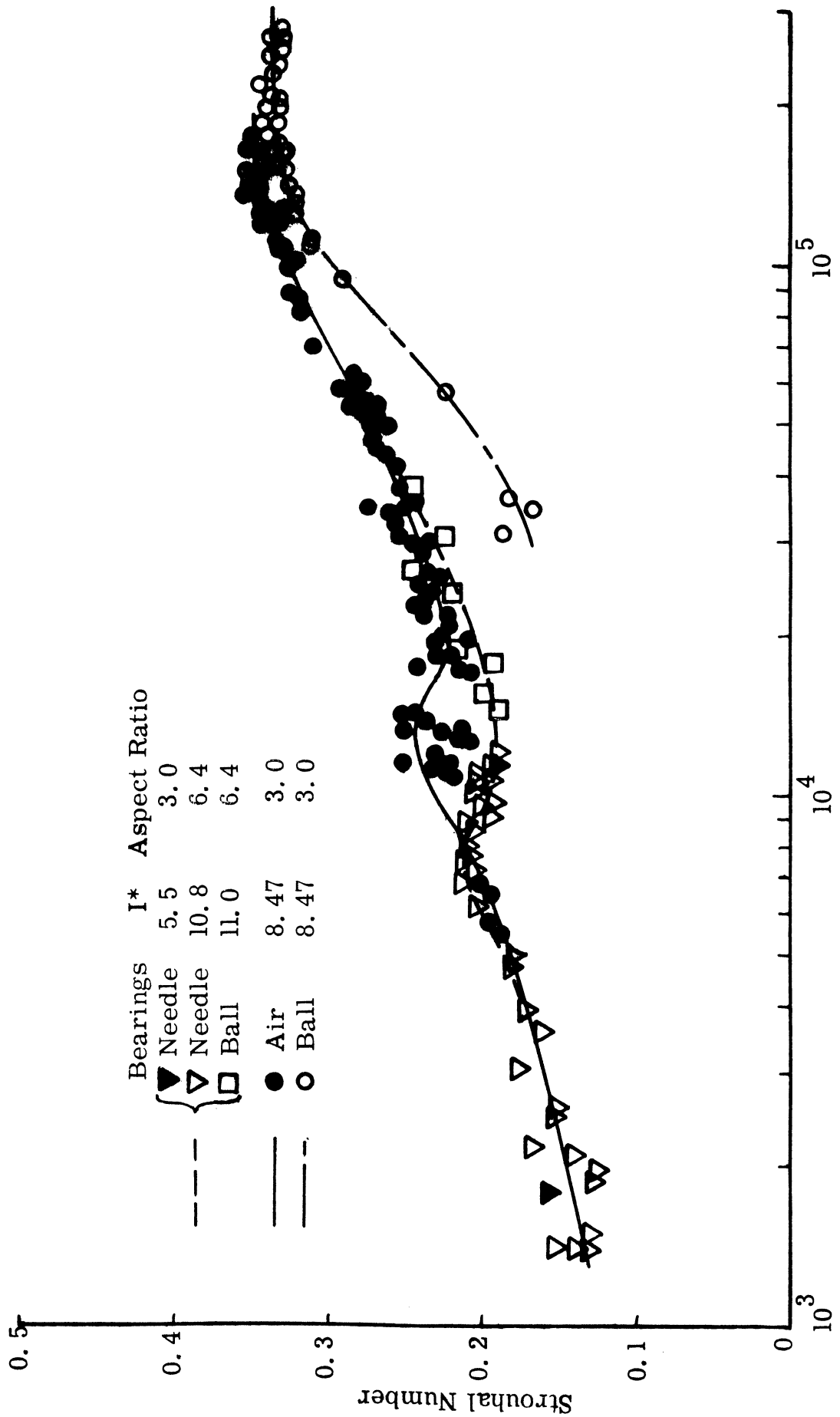

Figure 24. Strouhal Number vs Reynolds Number for Elliptical Airfoil.

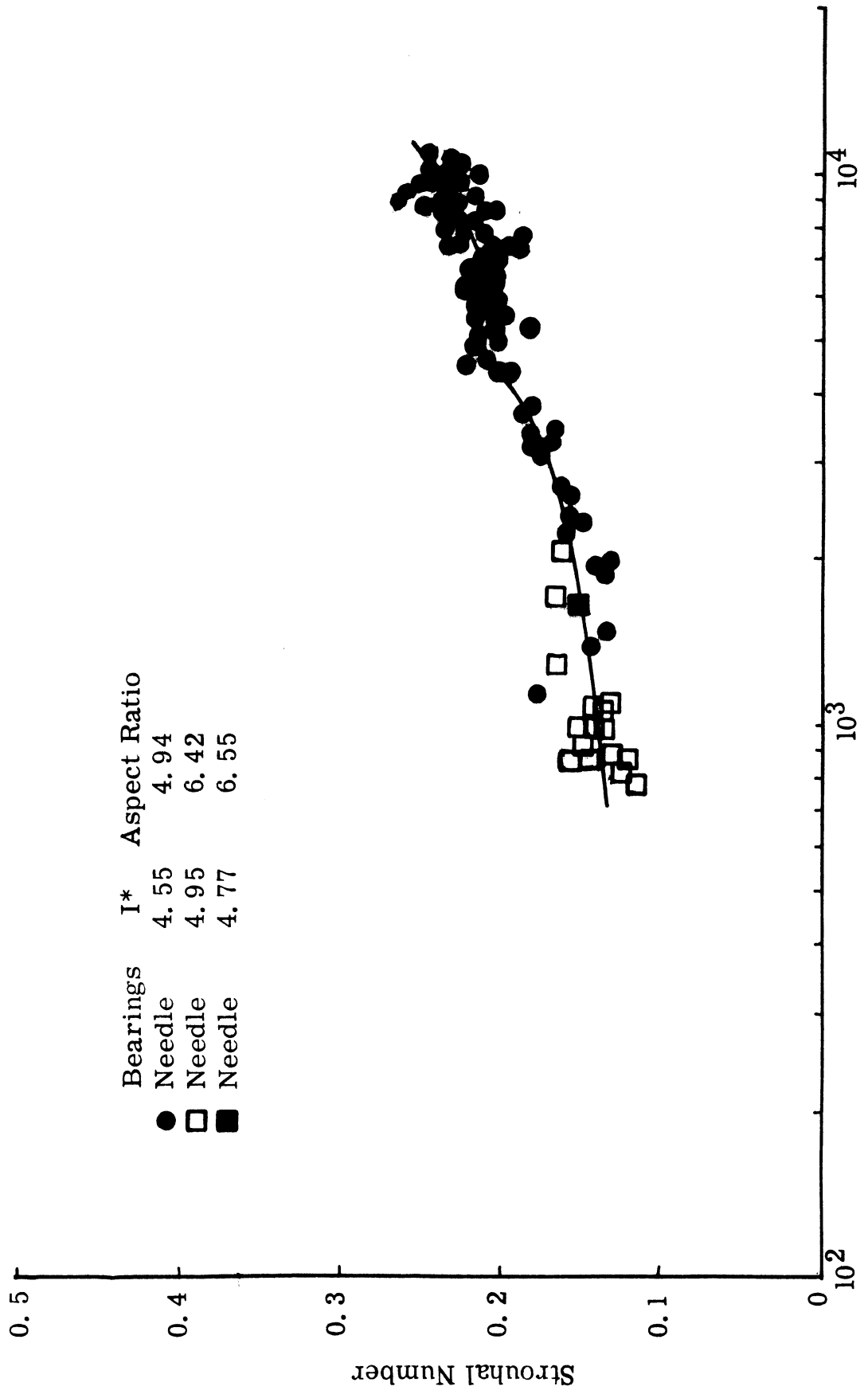

Figure 25. Strouhal Number vs Reynolds Number for Flat Plate.

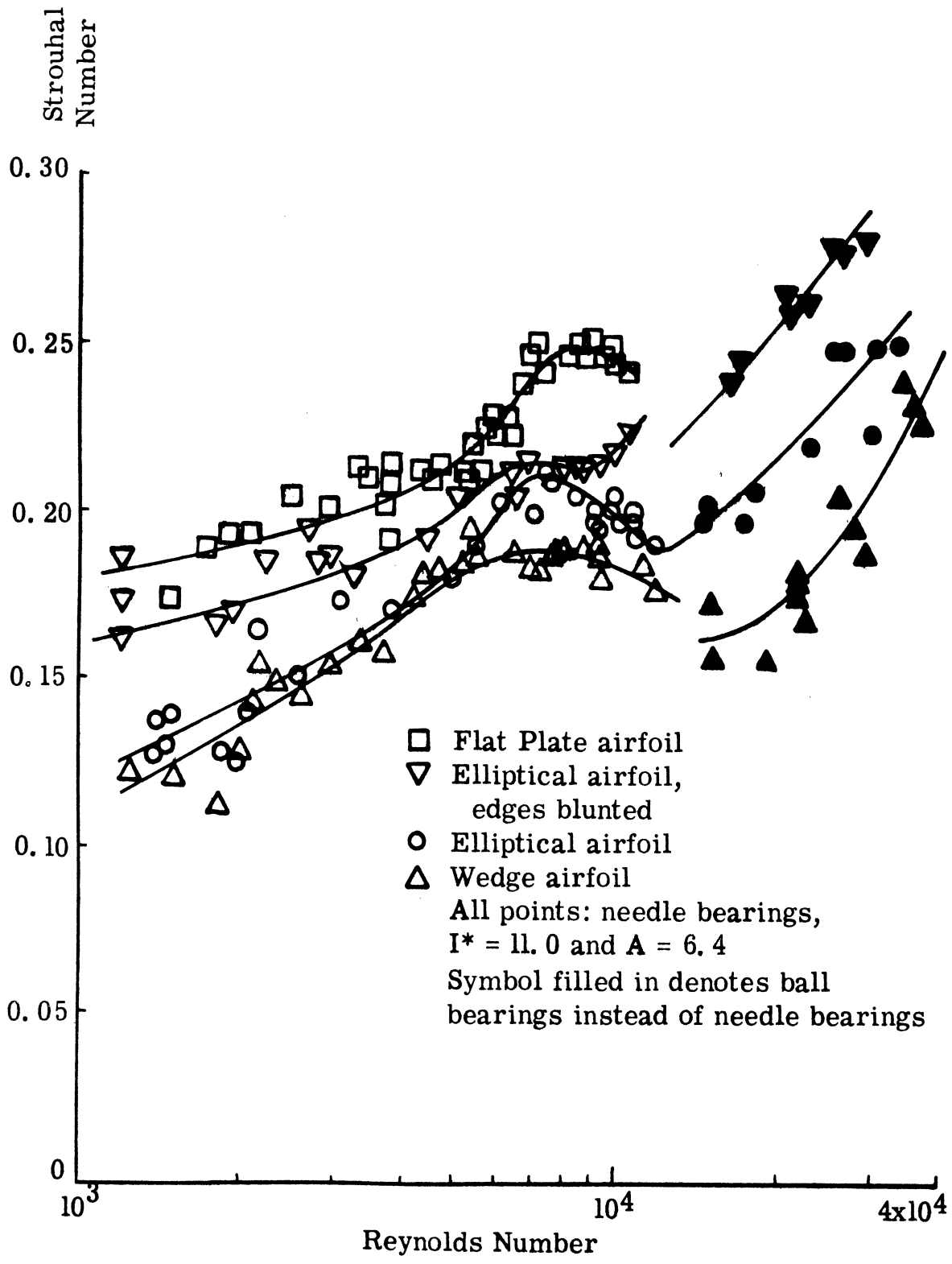

Figure 26. Strouhal Number vs Reynolds Number for Various Airfoils.

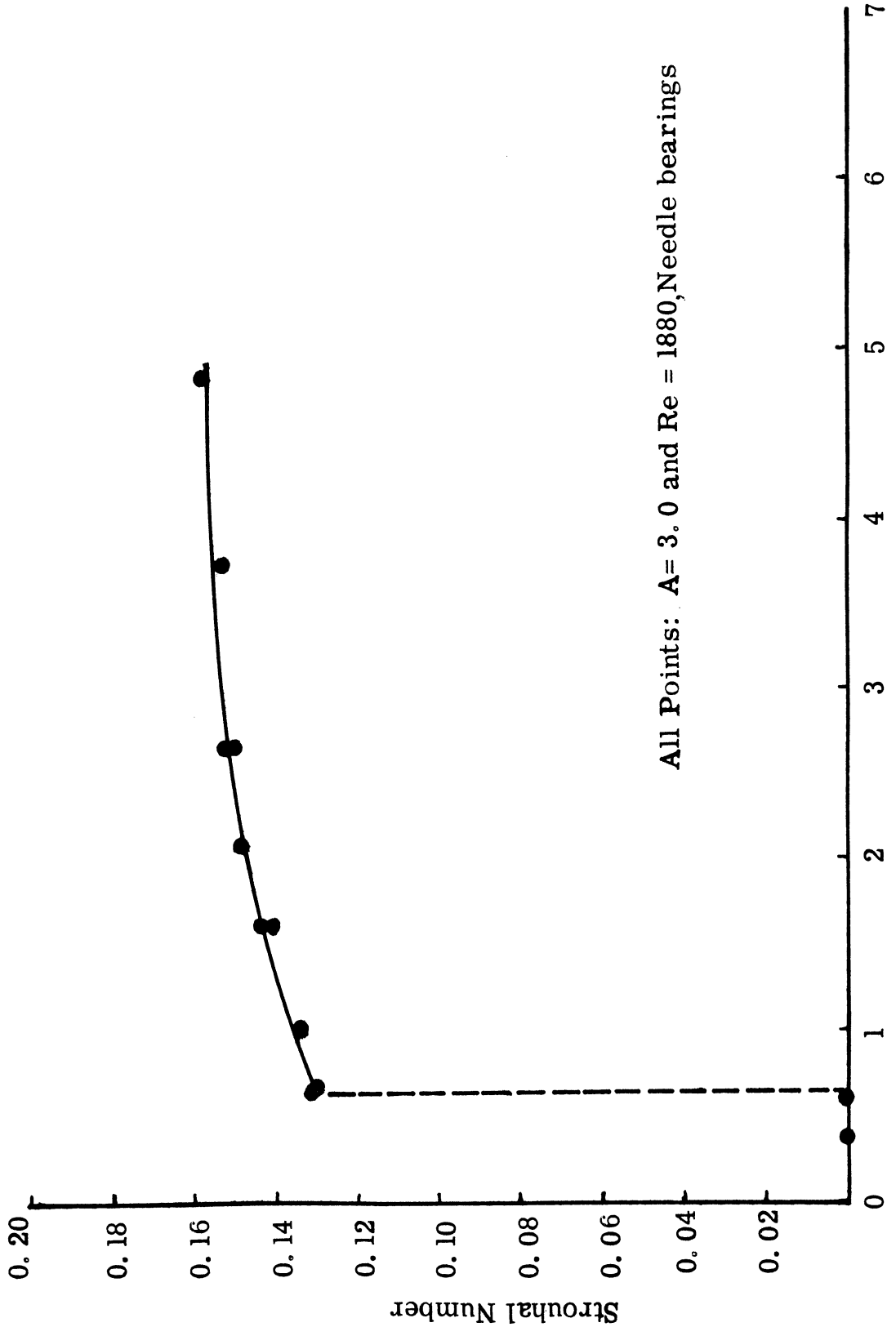

Figure 27. Influence of I* on Strouhal Number for Elliptical Airfoil.

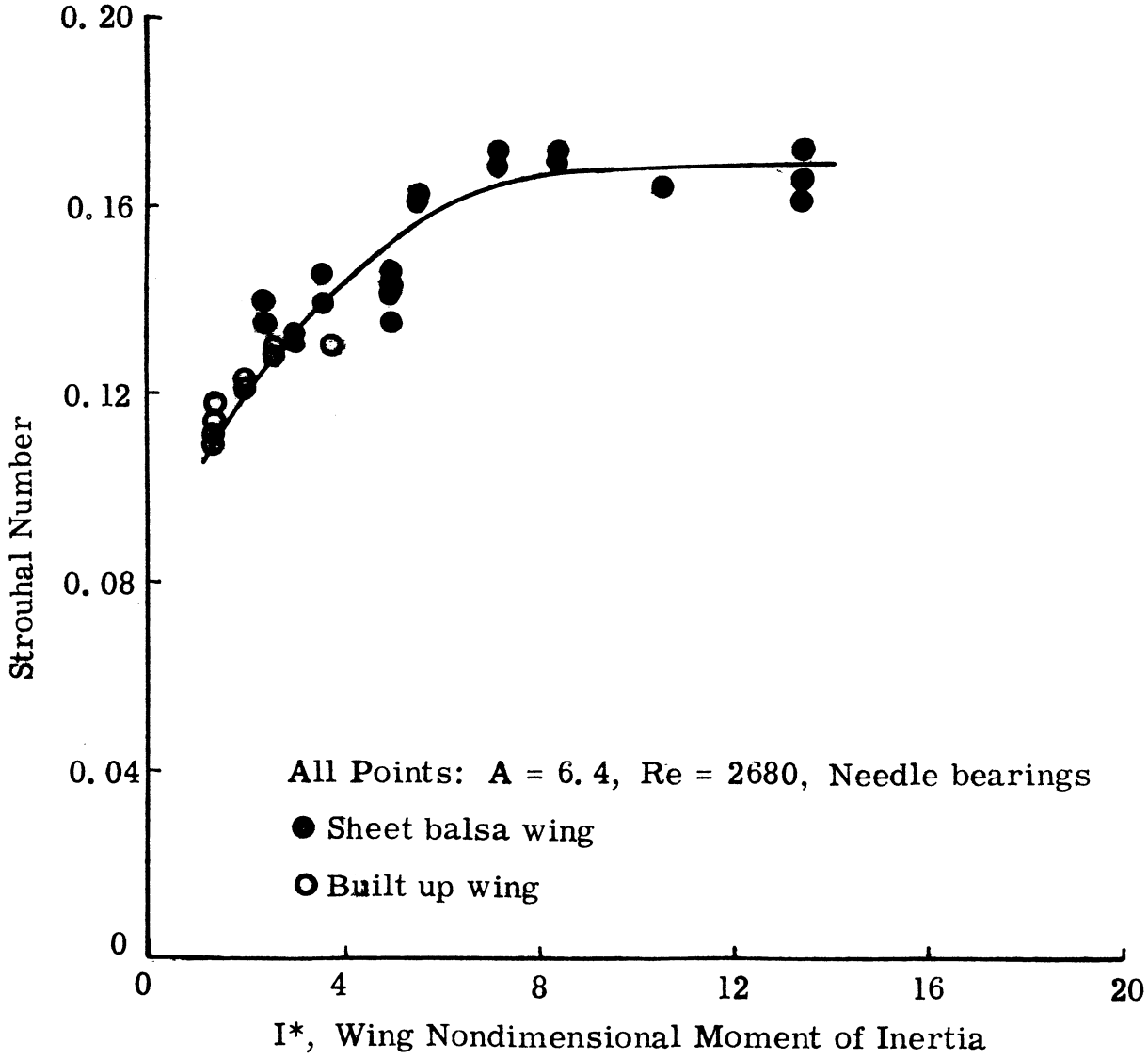

Figure 28. Influence of I* on Strouhal Number for Flat Plate Airfoil.

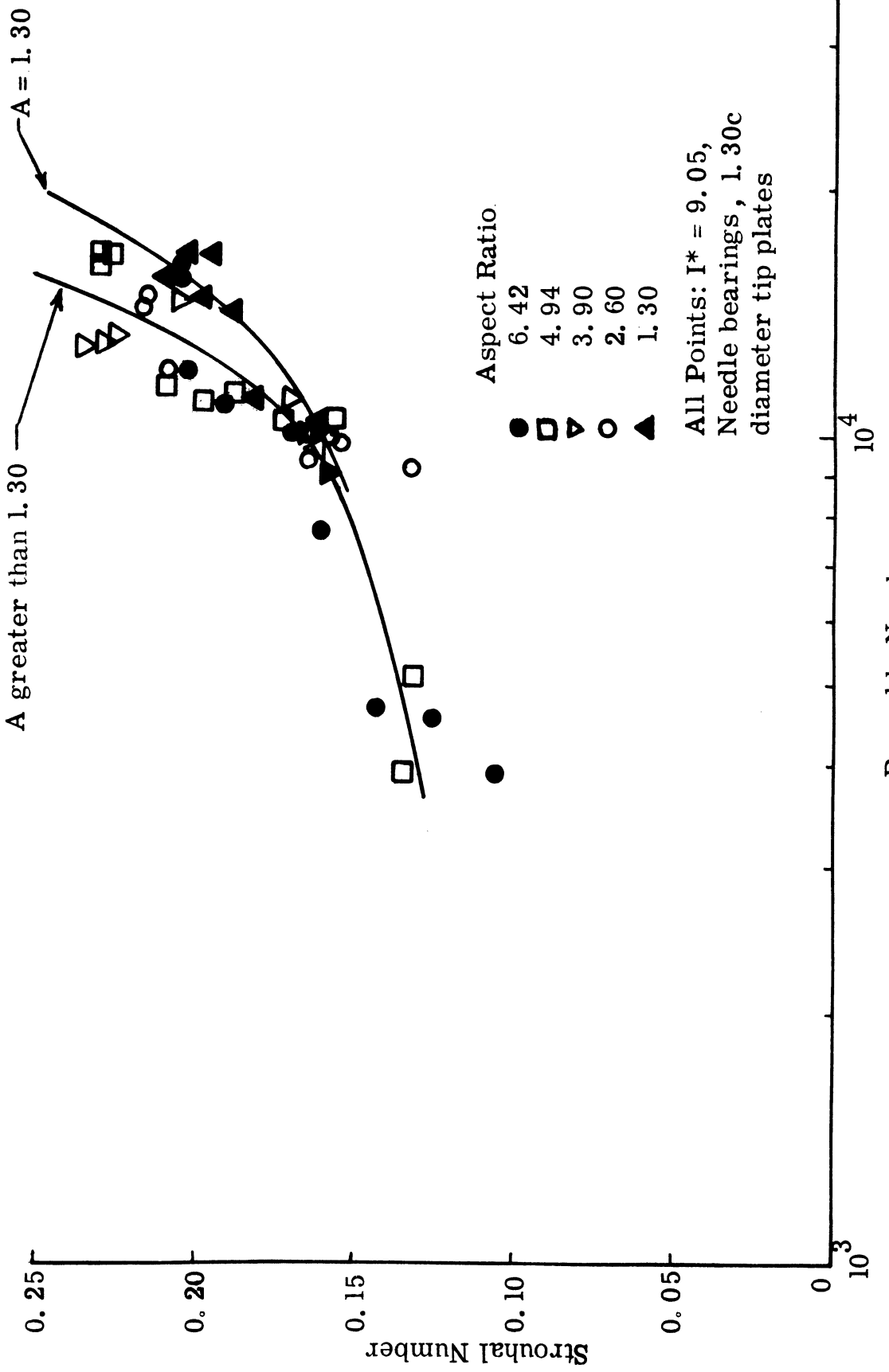

Figure 29. Influence of Aspect Ratio on Strouhal Number.

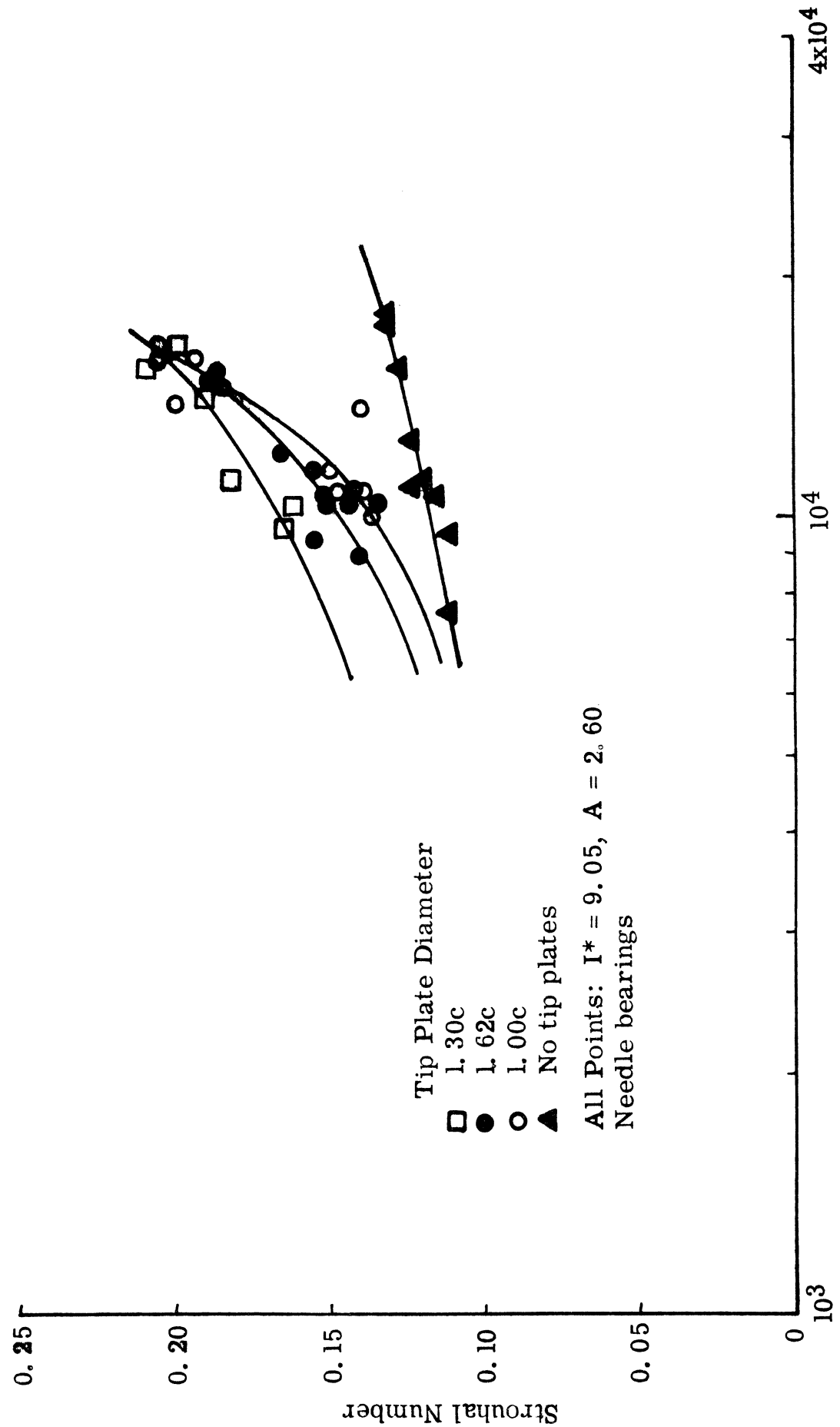

Figure 30. Influence of Tip Plate Diameter on Strouhal Number.

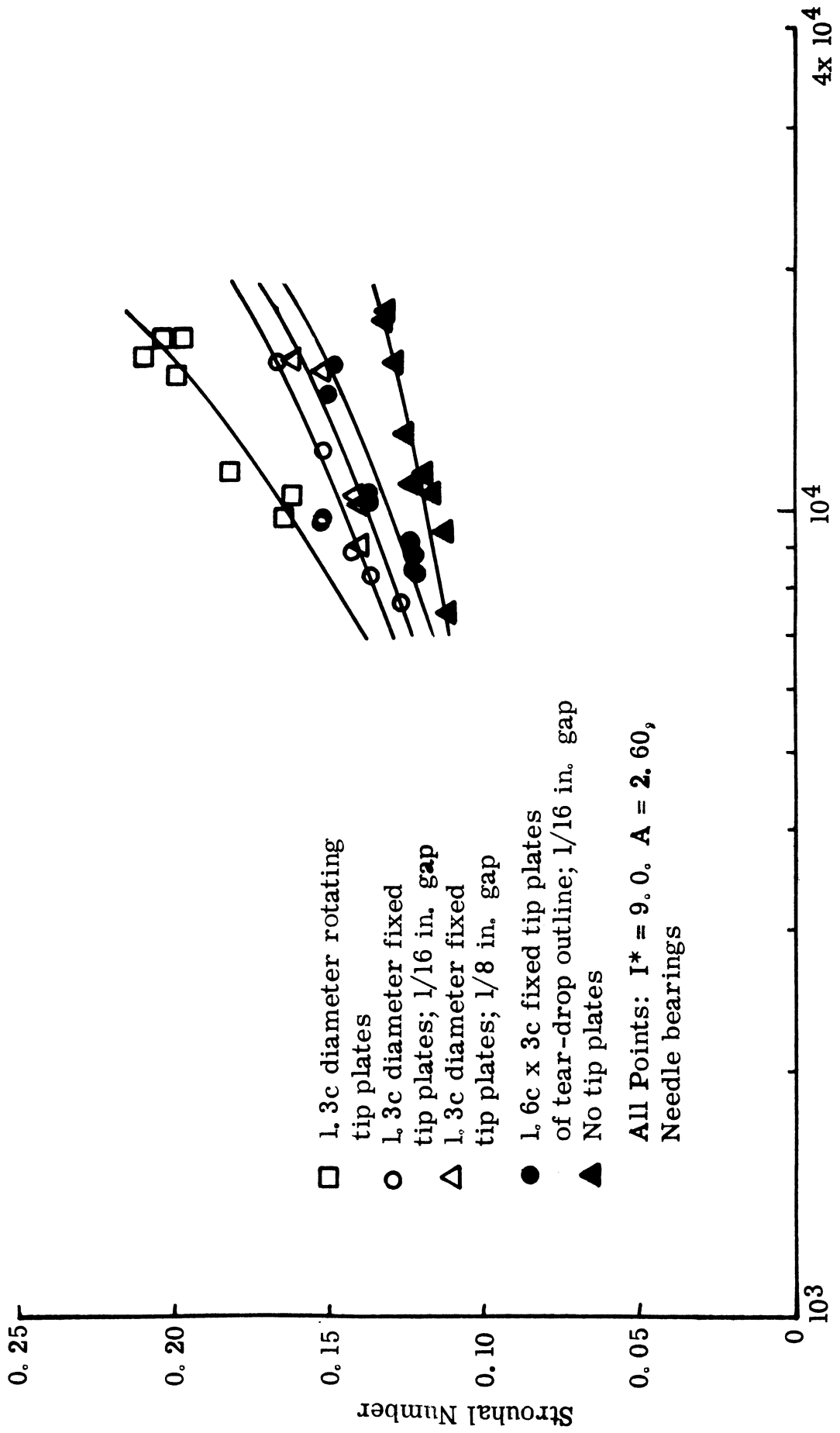

Figure 31. Influence of Tip Plate Configuration on Strouhal Number.

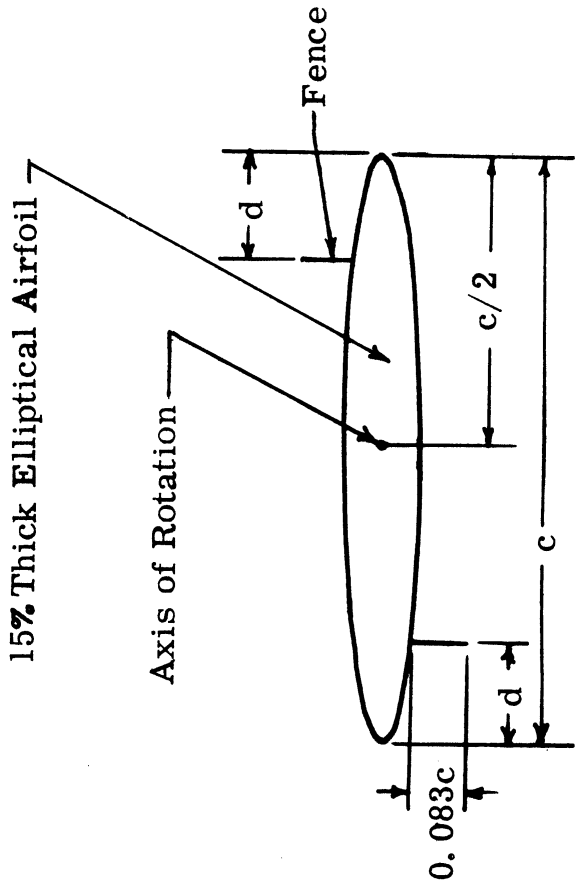

Figure 32. Nomenclature for Fence Tests.

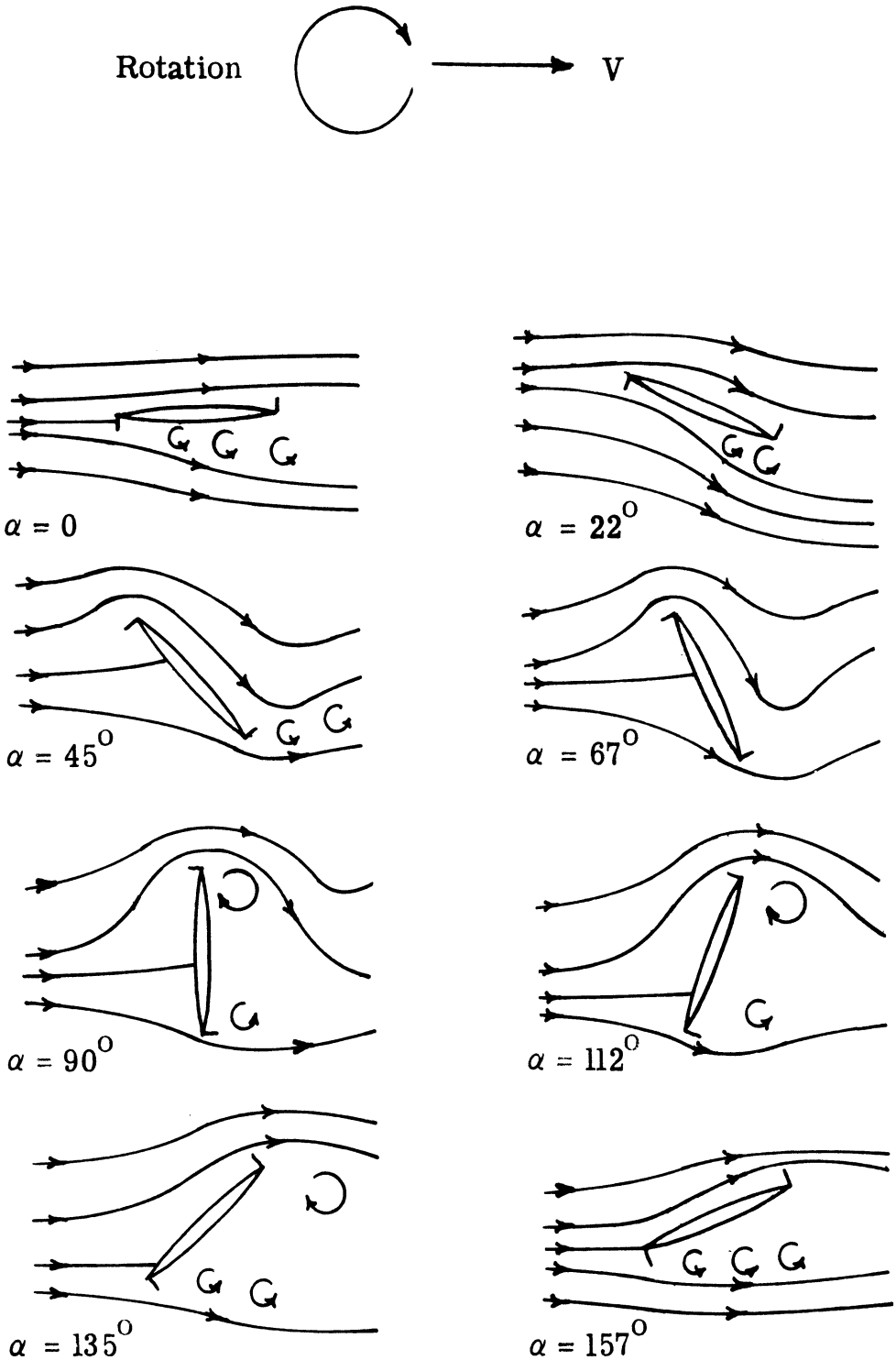

d/c = 0

Figure 33a. Flow Pattern over Autorotating Wing with Fences at Re = 10,000.

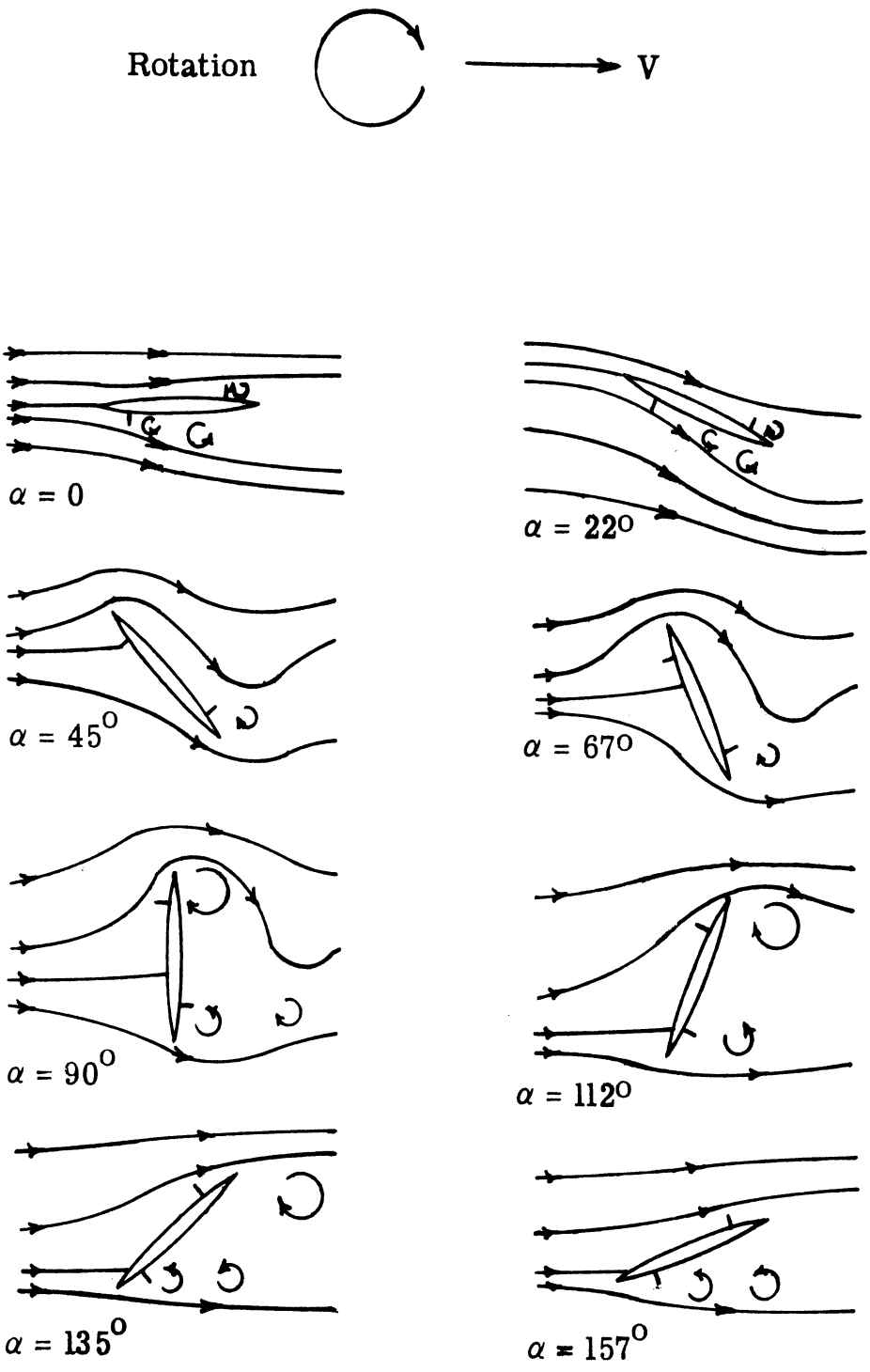

d/c = 0.25

Figure 33b. Flow Pattern Over Autorotating Wing with Fences at Re = 10,000.

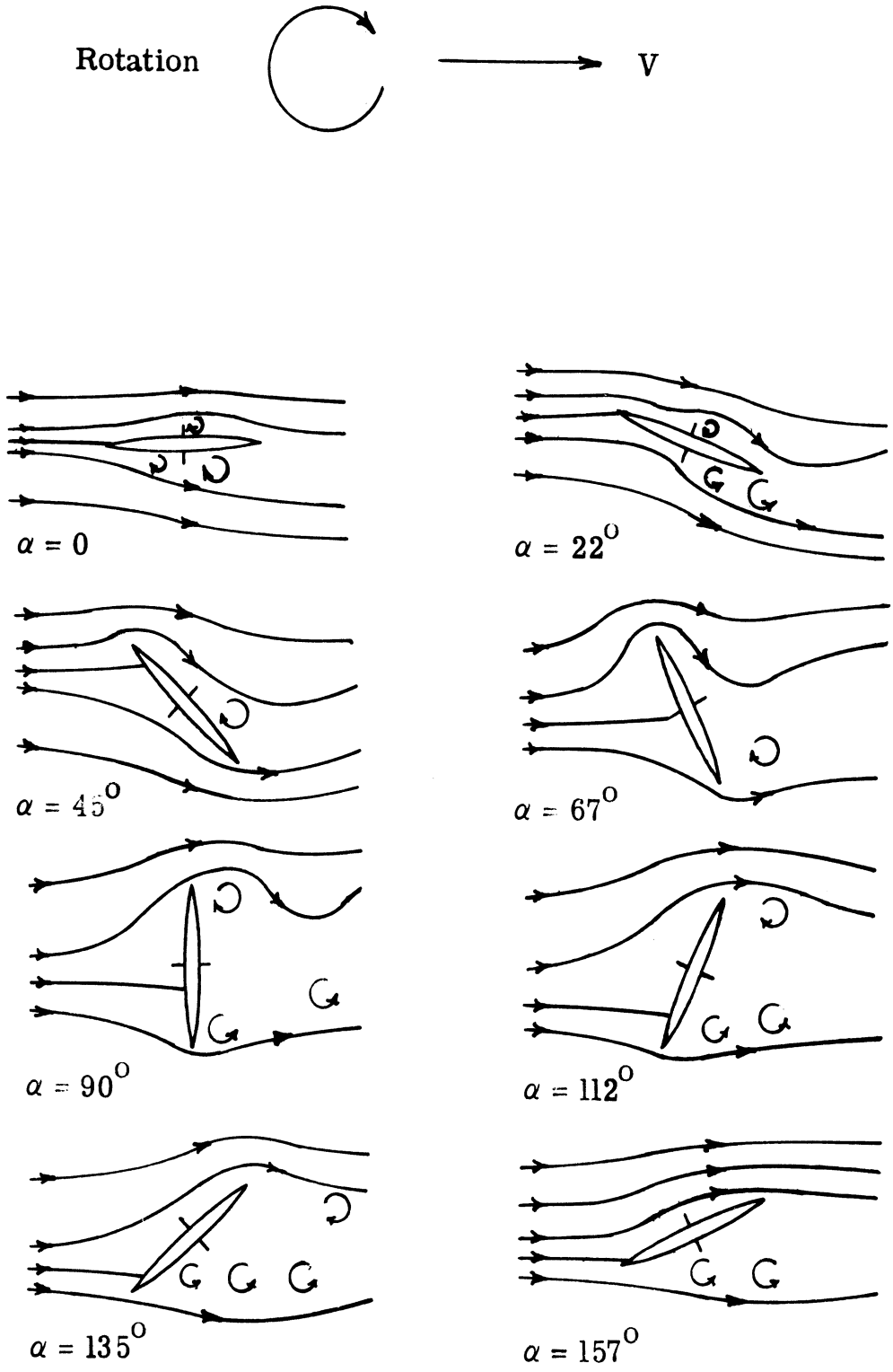

d/c = 0.5

Figure 33c. Flow Pattern Over Autorotating Wing with Fences at Re = 10,000.

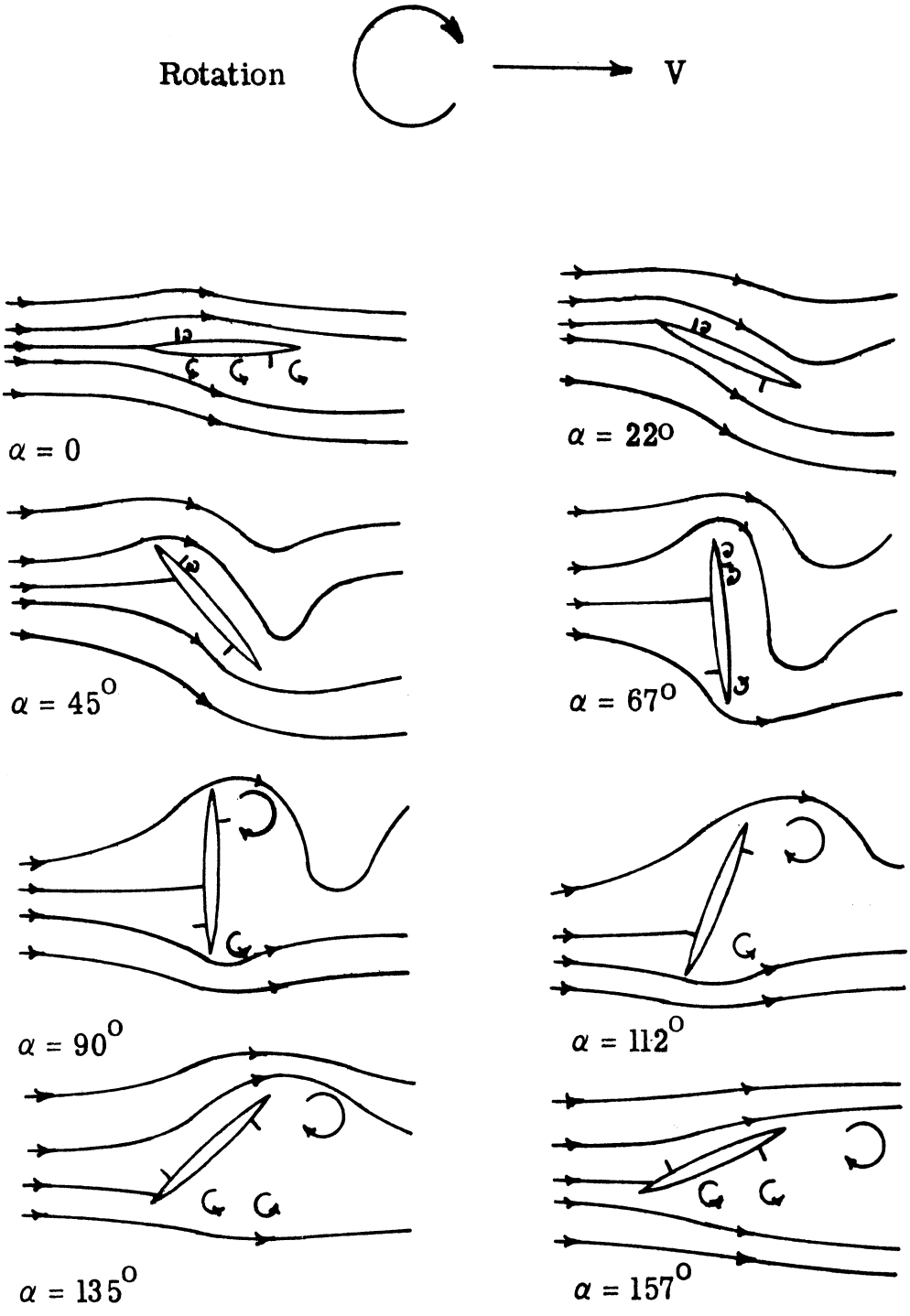

d/c = 0.75

Figure 33d. Flow Pattern Over Autorotating Wing with Fences at Re = 10,000.

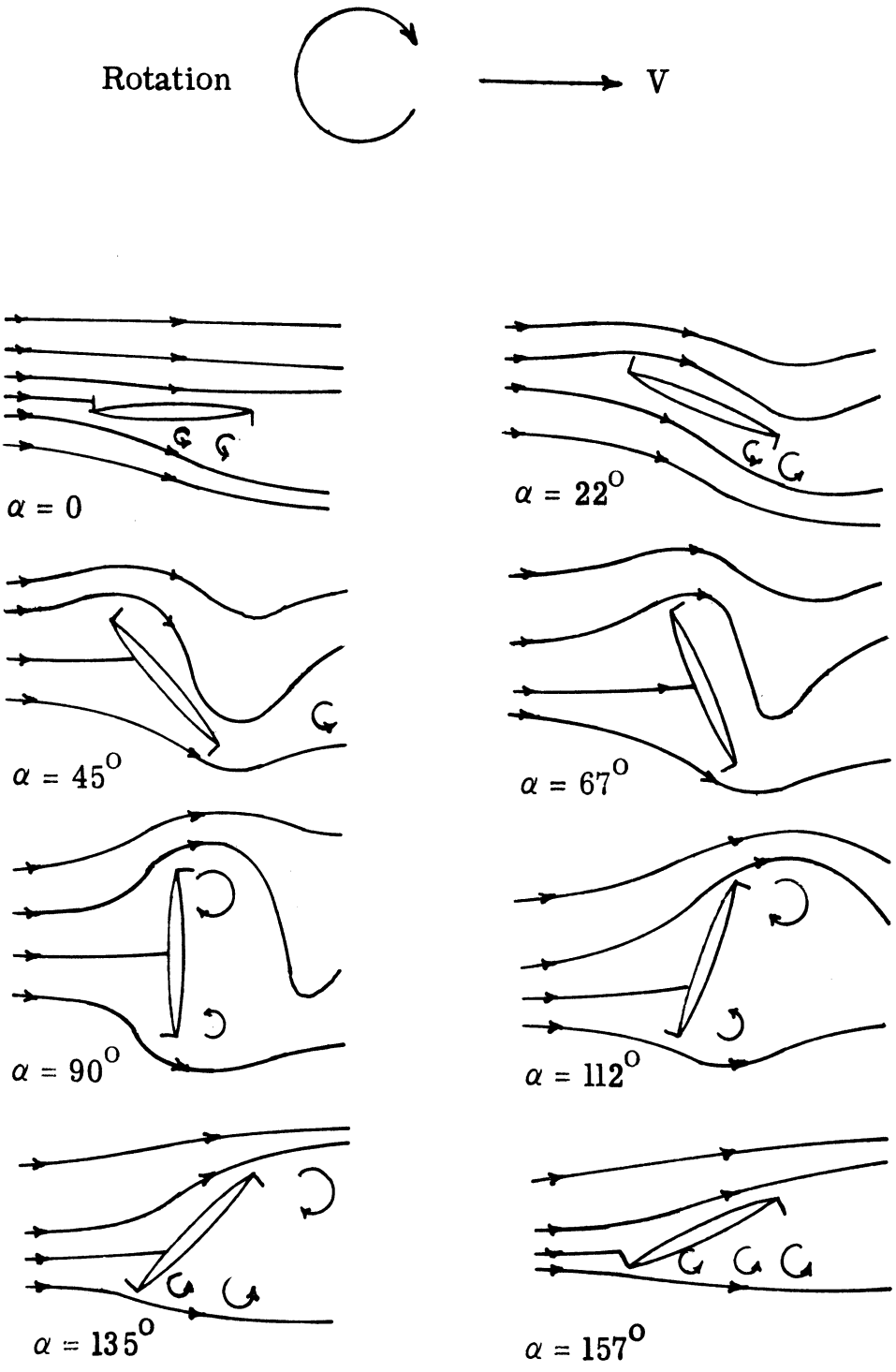

d/c = 1.0

Figure 33e. Flow Pattern over Autorotating Wing with Fences at Re = 10,000.

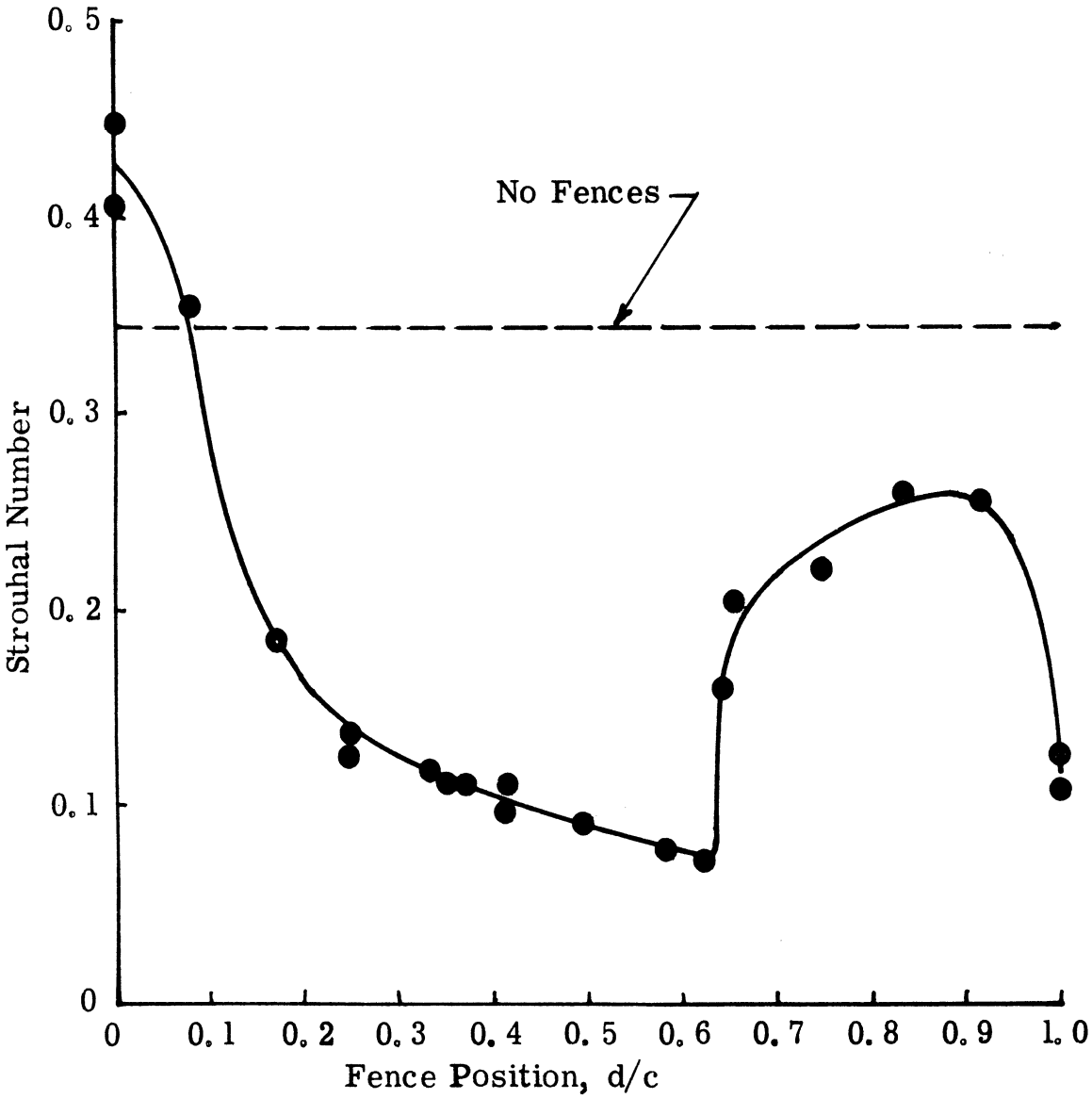

Figure 34. Influence of Fence Location on Strouhal Number at Re = 78,000.

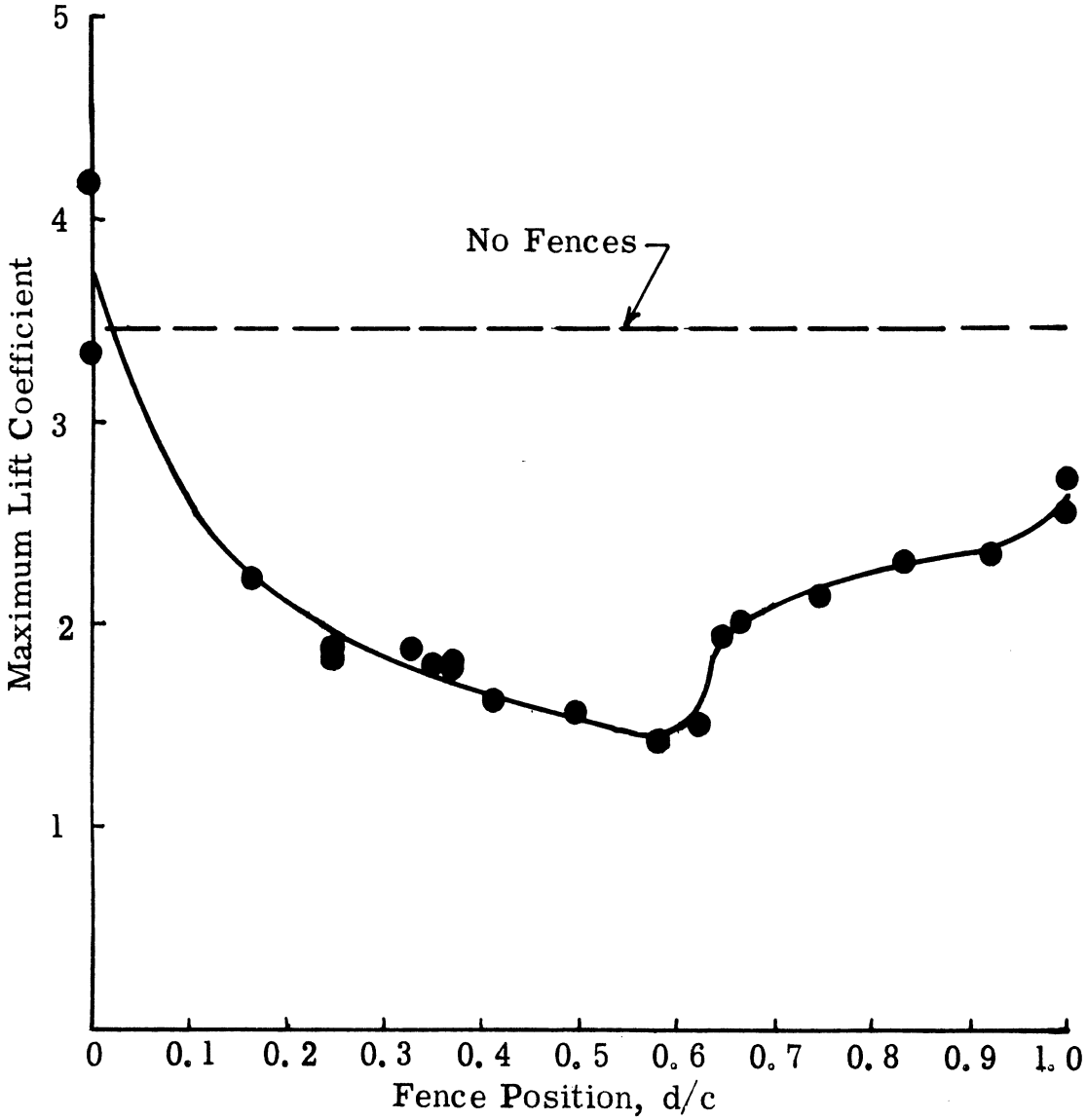

Figure 35. Influence of Fence Location on Maximum Lift Coefficient at Re = 78,000.

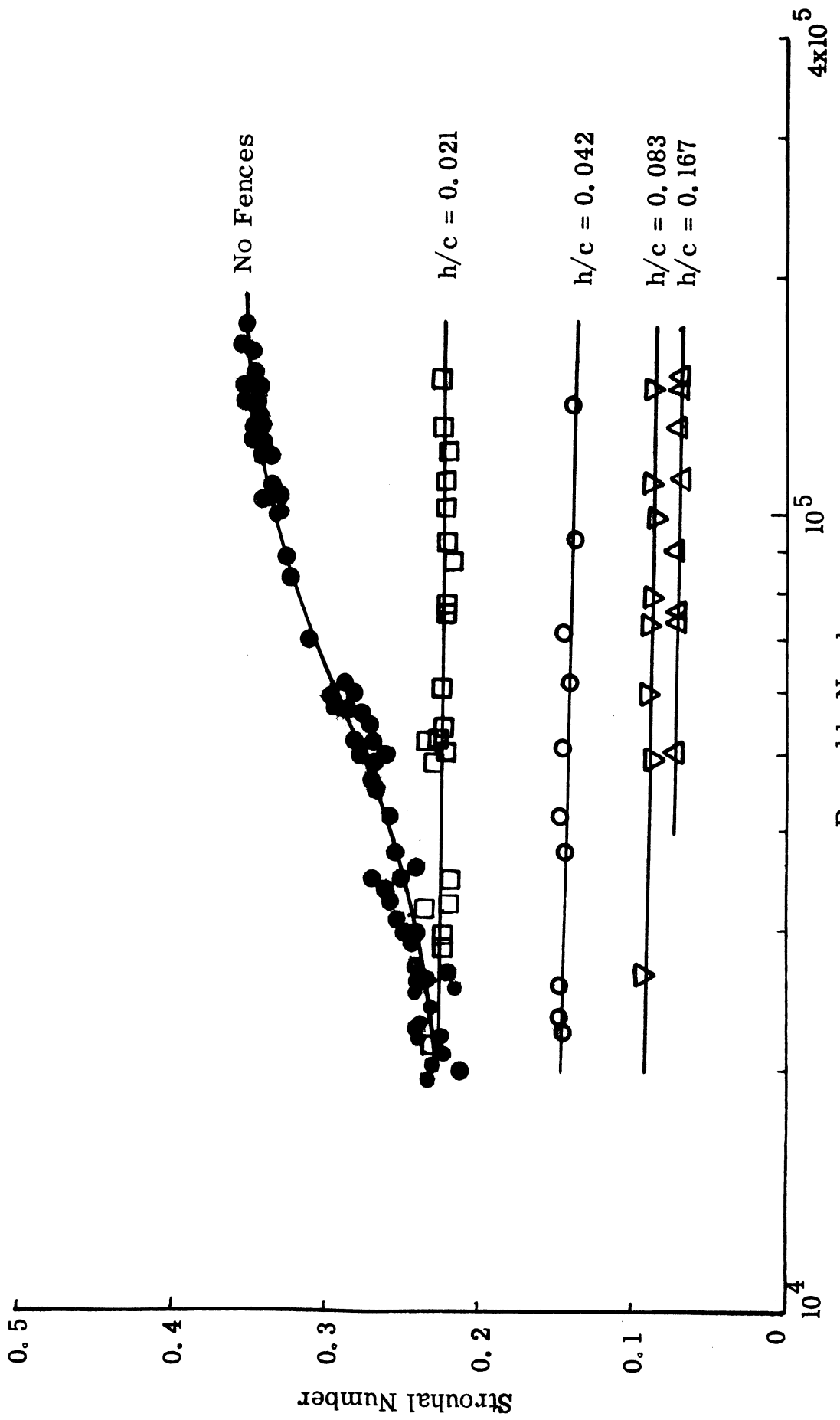

Figure 36. Influence of Height of Mid-Chord Fence on Strouhal Number.

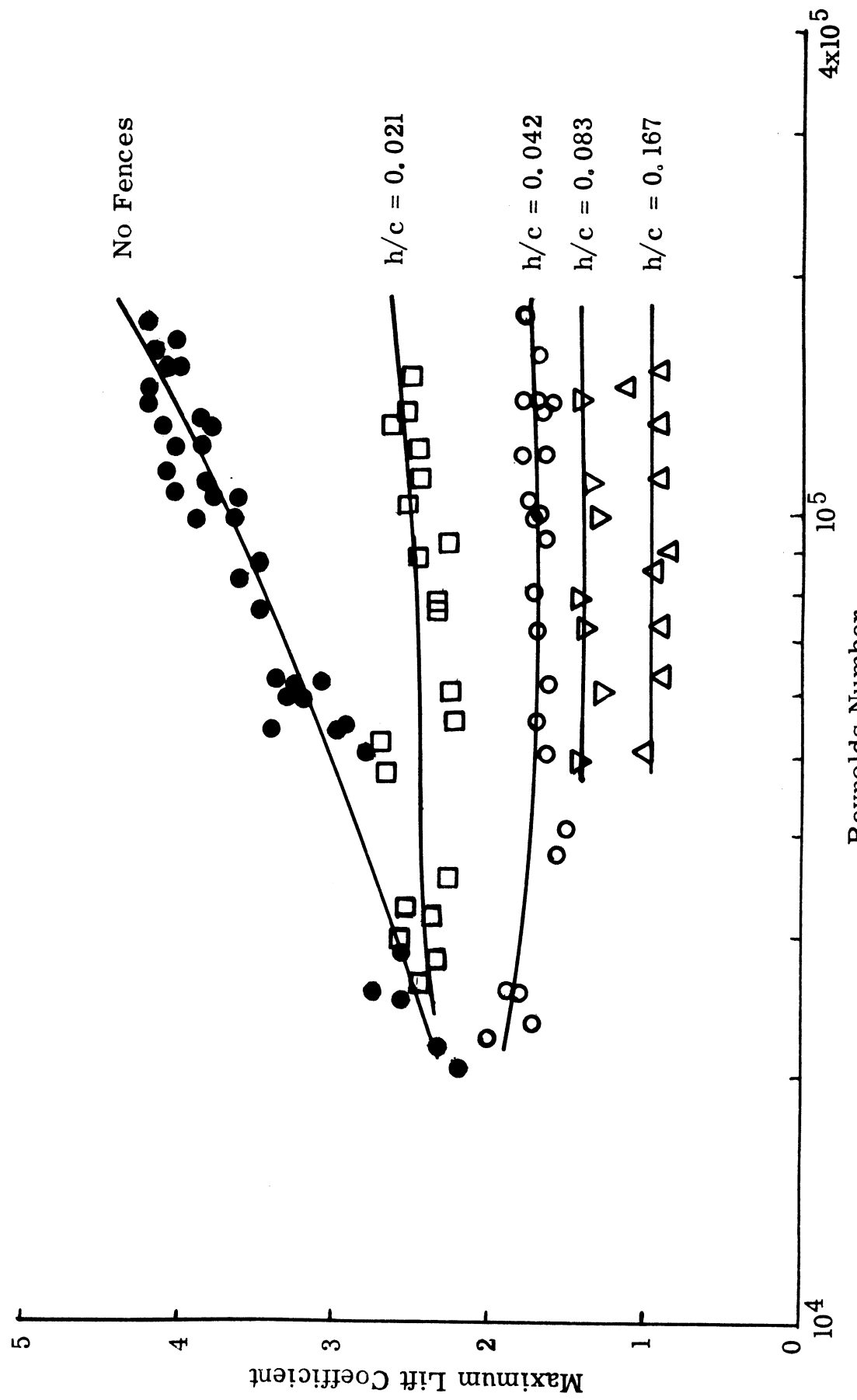

Figure 37. Influence of Height of Mid-Chord Fence on Maximum Lift Coefficient.

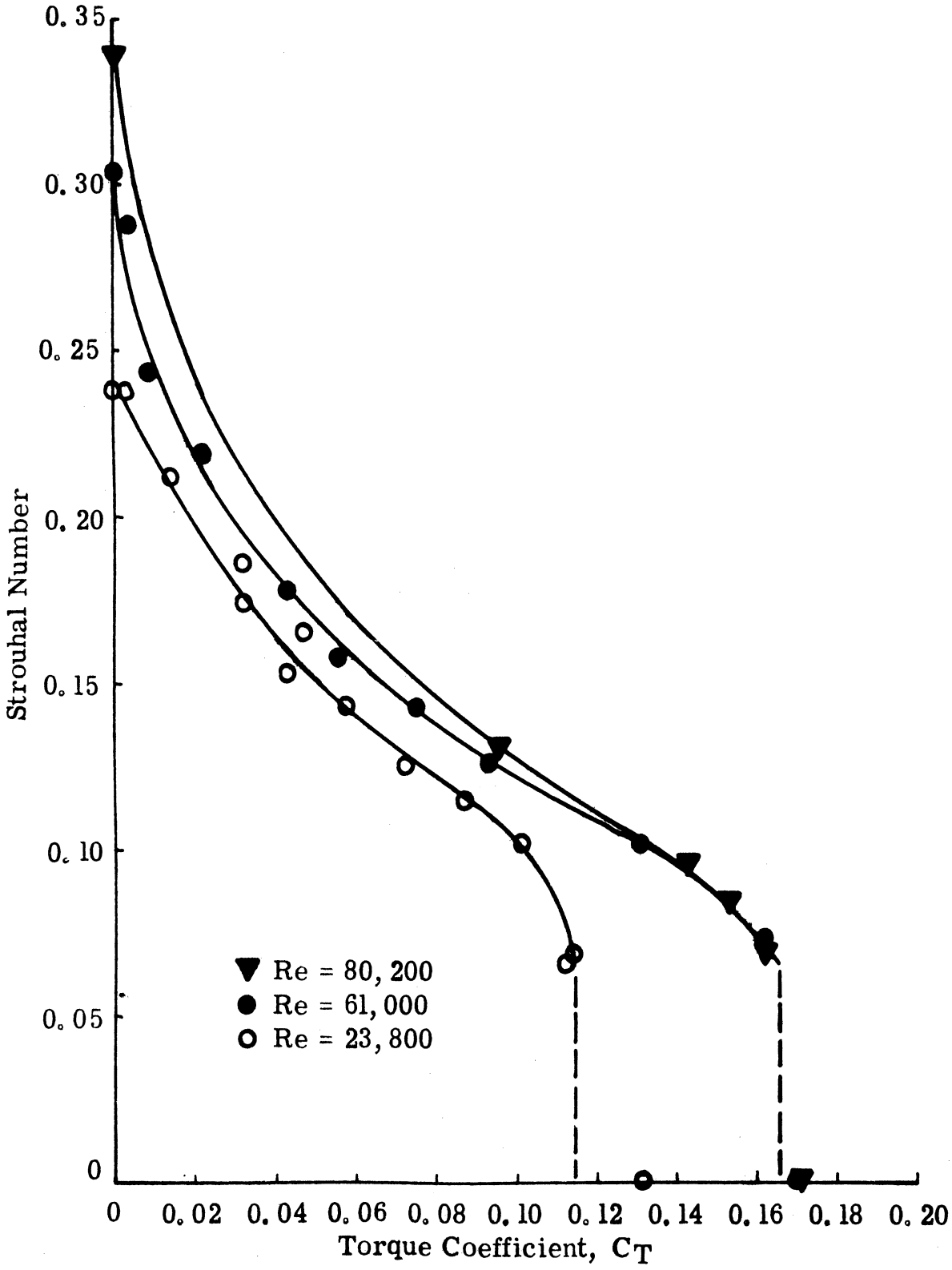

Figure 38. Influence of Retarding Torque on Strouhal Number.

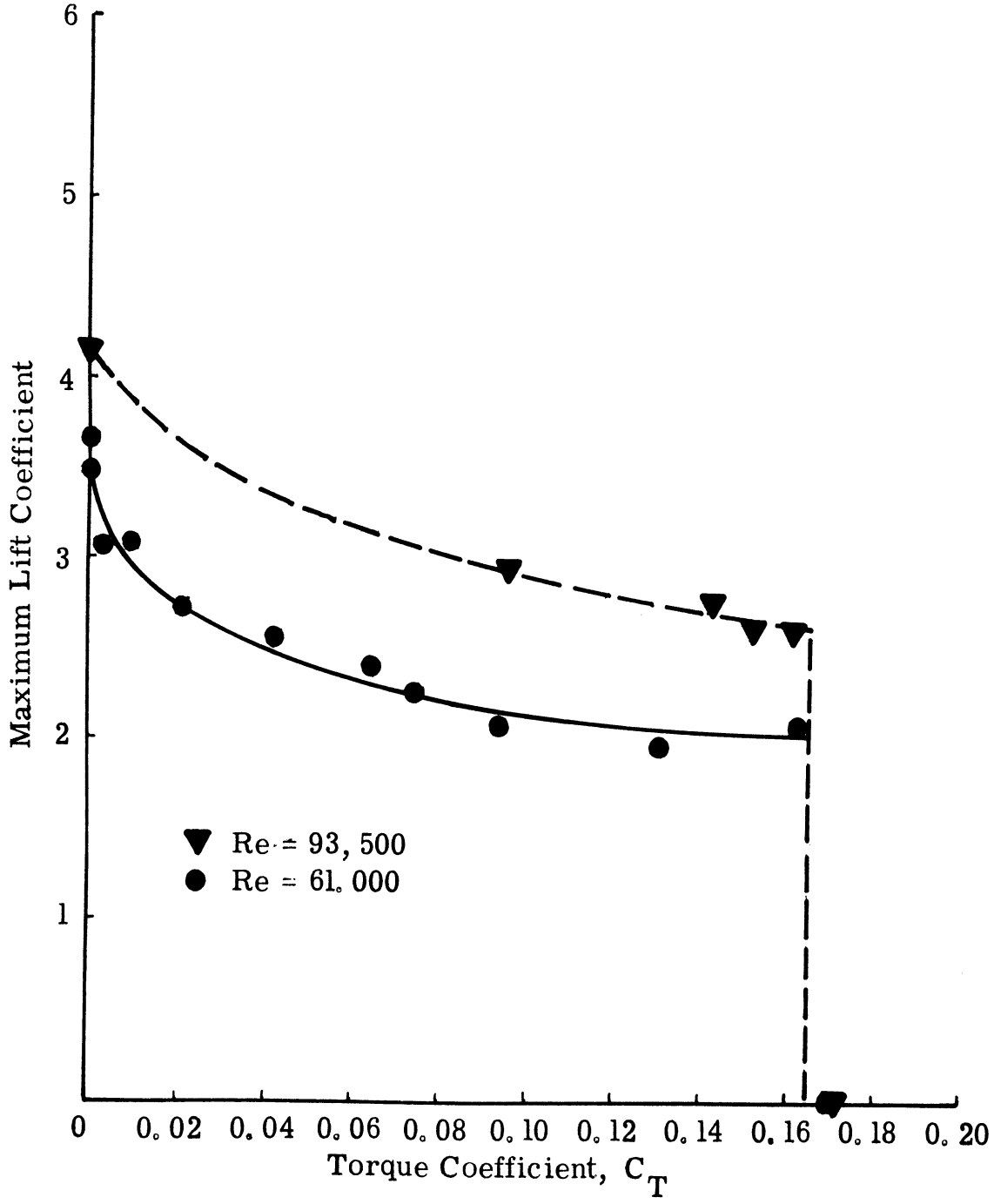

Figure 39. Influence of Retarding Torque on Maximum Lift Coefficient

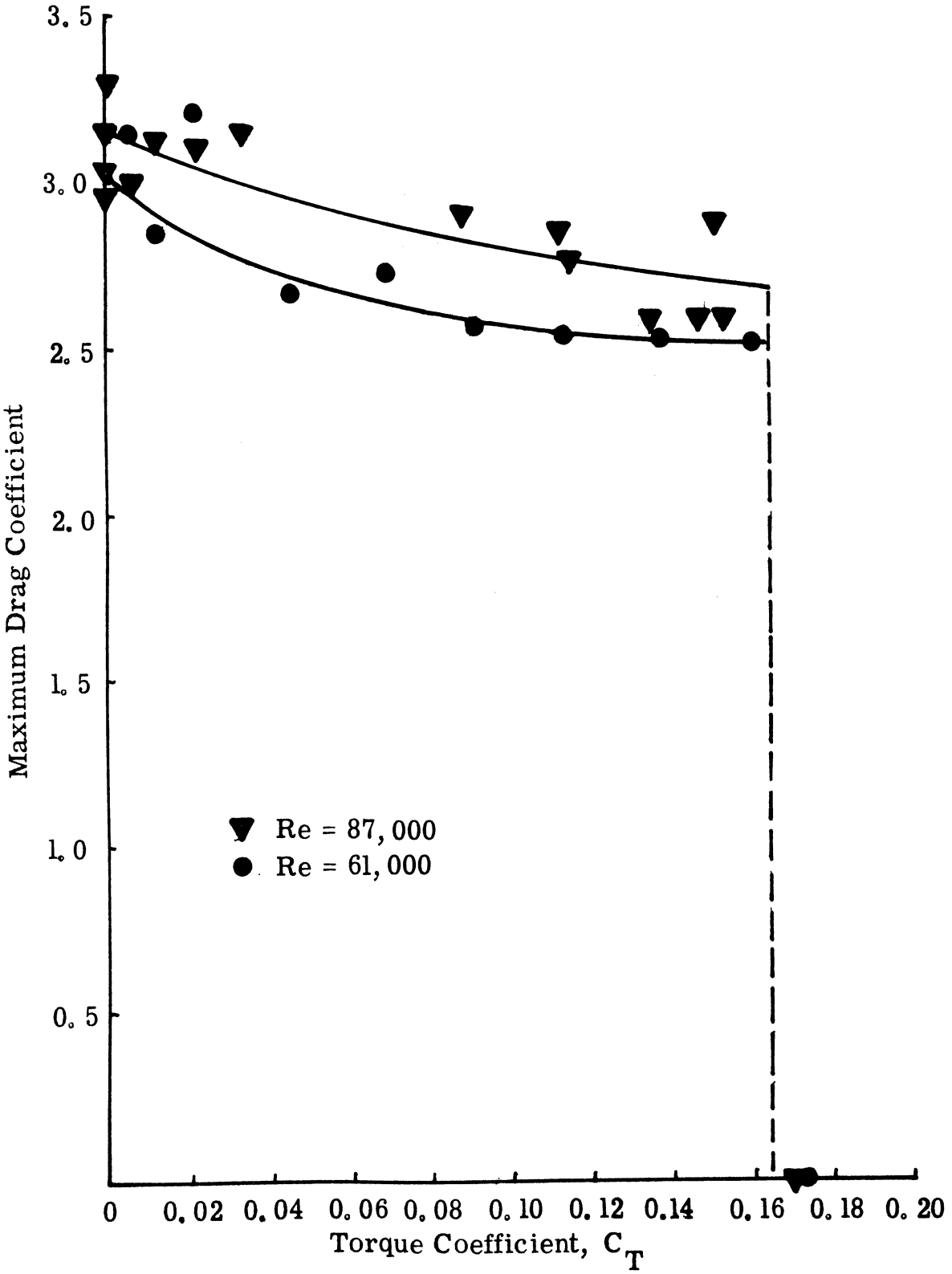

Figure 40. Influence of Retarding Torque on Maximum Drag Coefficient.

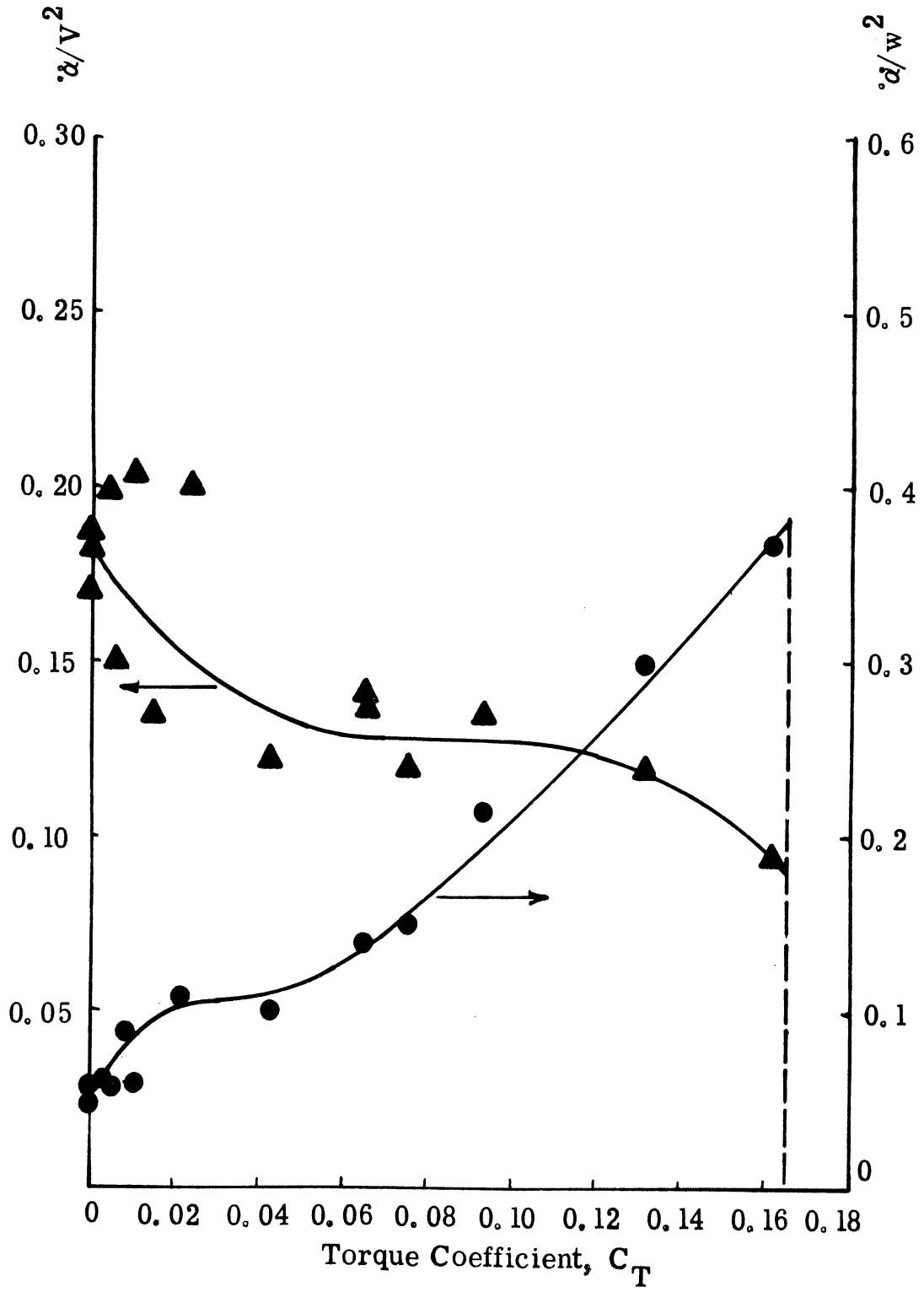

Figure 41. Influence of Retarding Torque on Maximum Angular Acceleration at Re = 61,000.

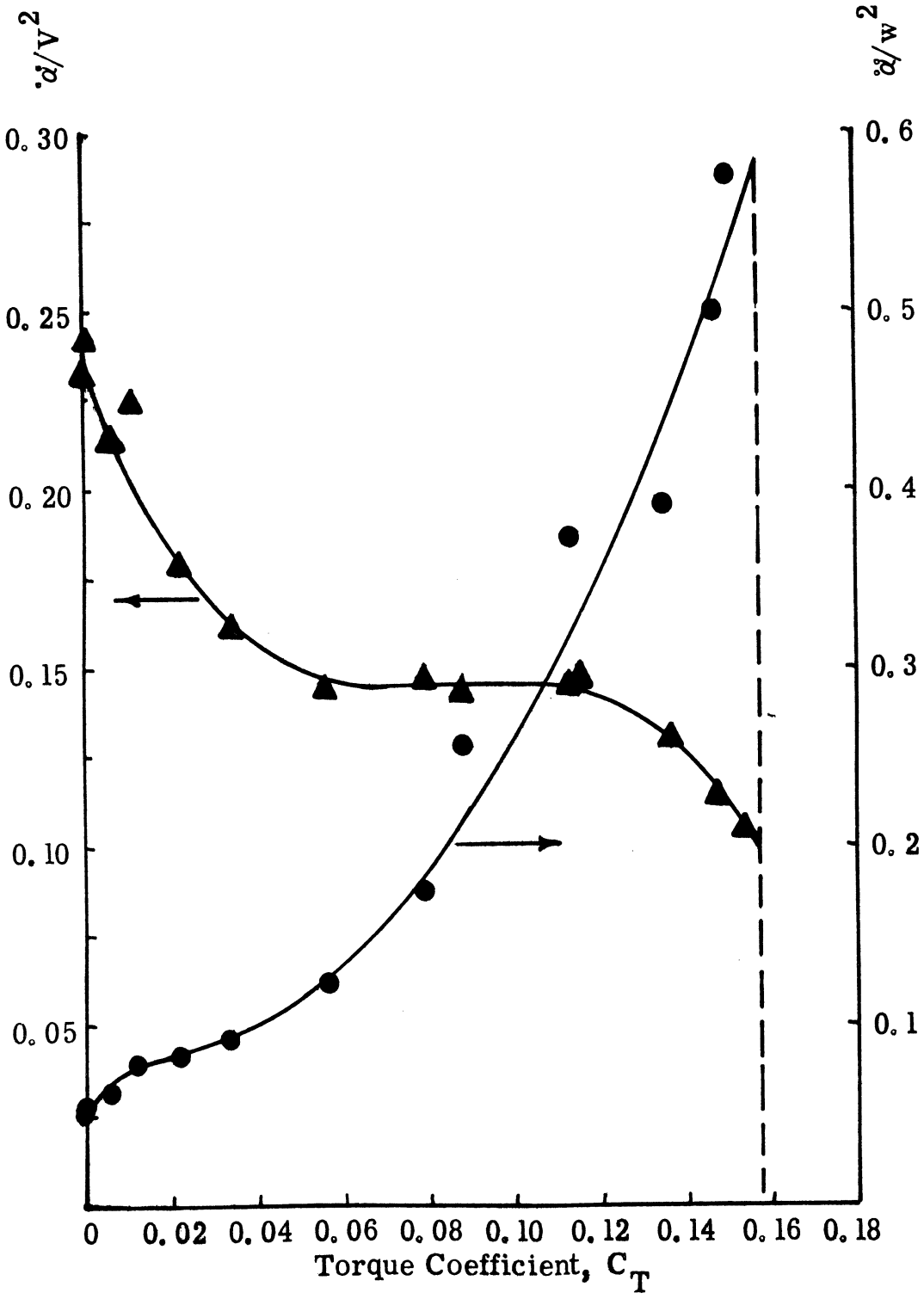

Figure 42. Influence of Retarding Torque on Maximum Angular Acceleration at Re = 87,000.

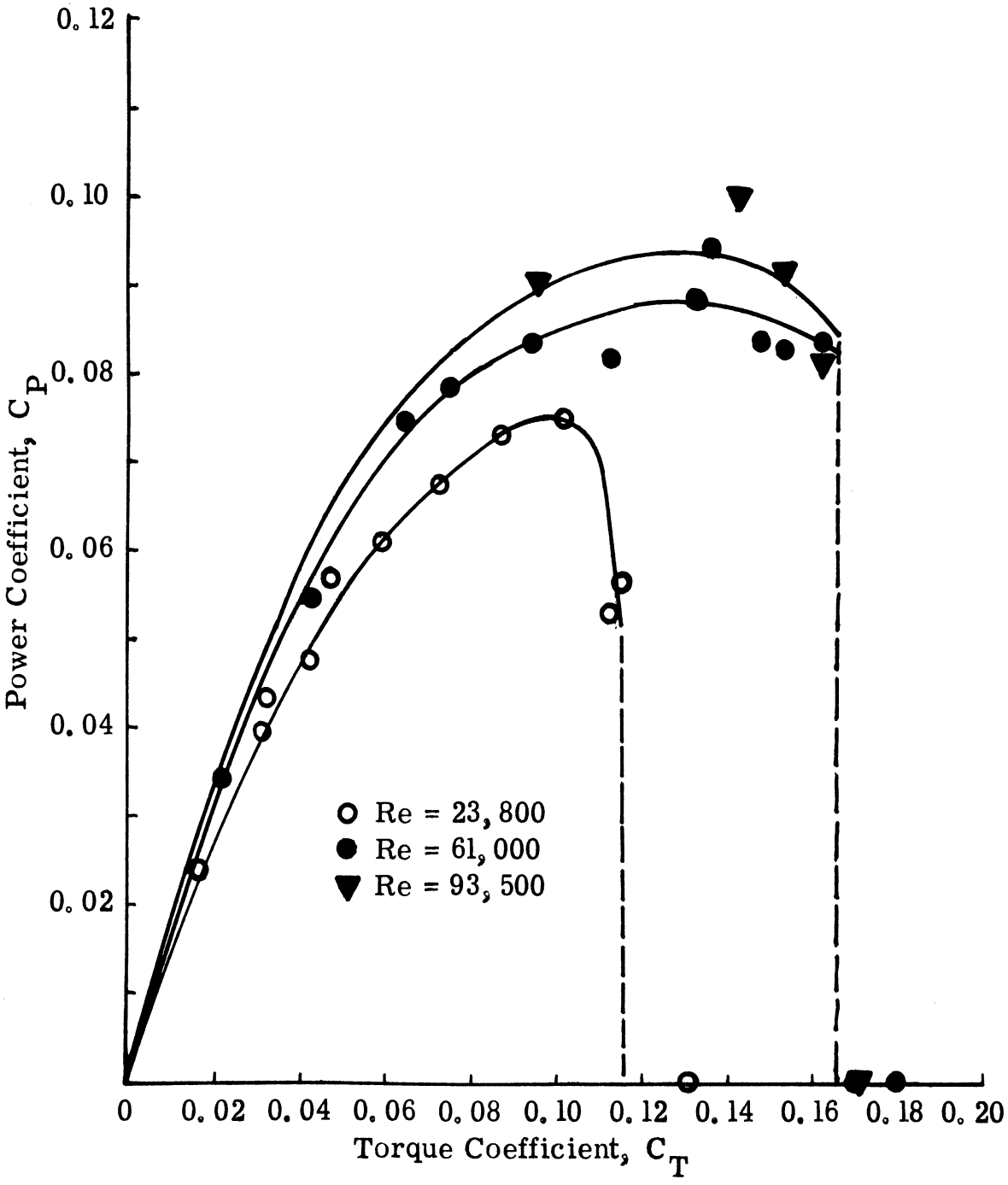

Figure 43. Power Output of Autorotating Wing.

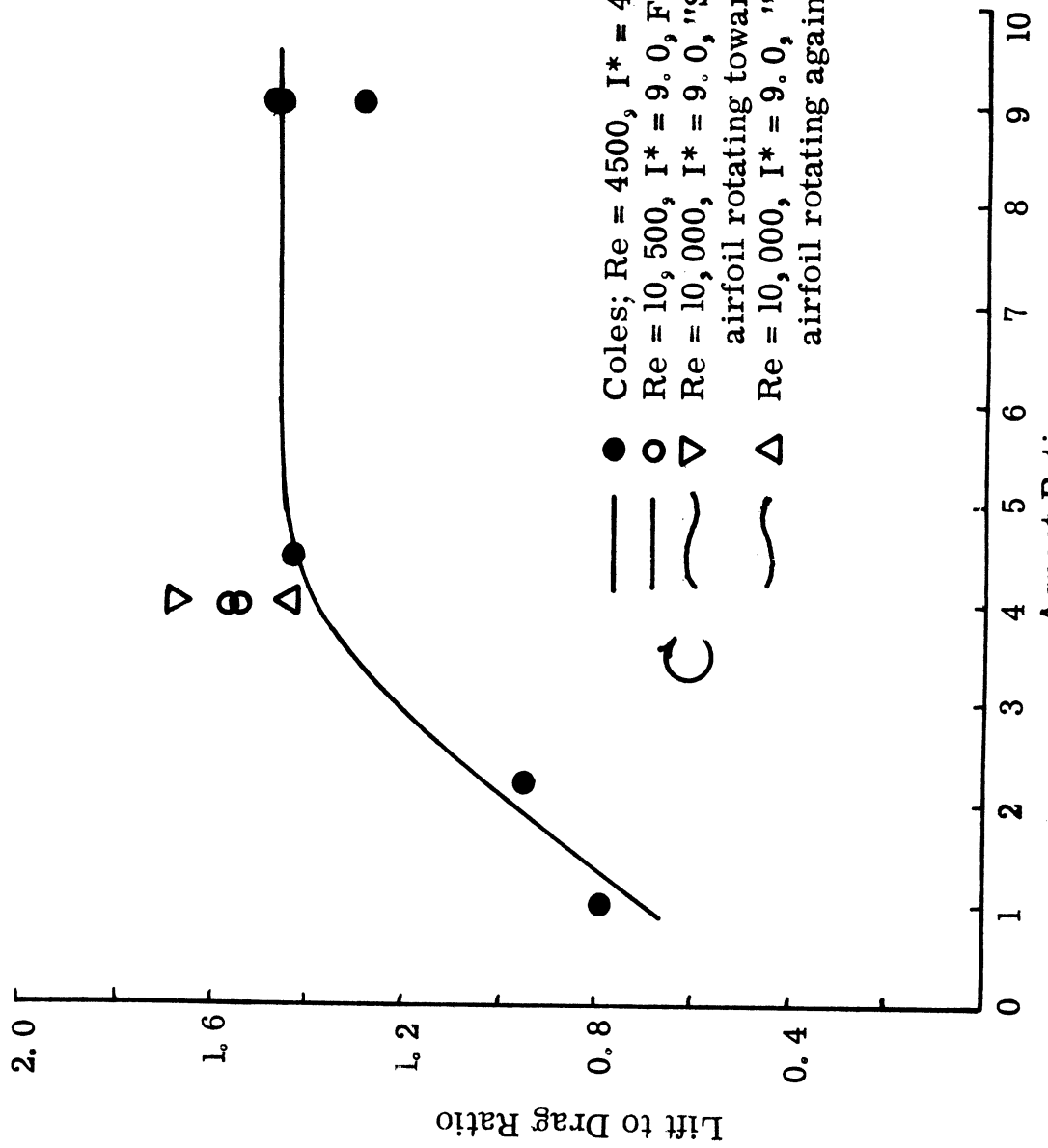

Figure 44. Lift to Drag Ratio for Falling Autorotating Wings.

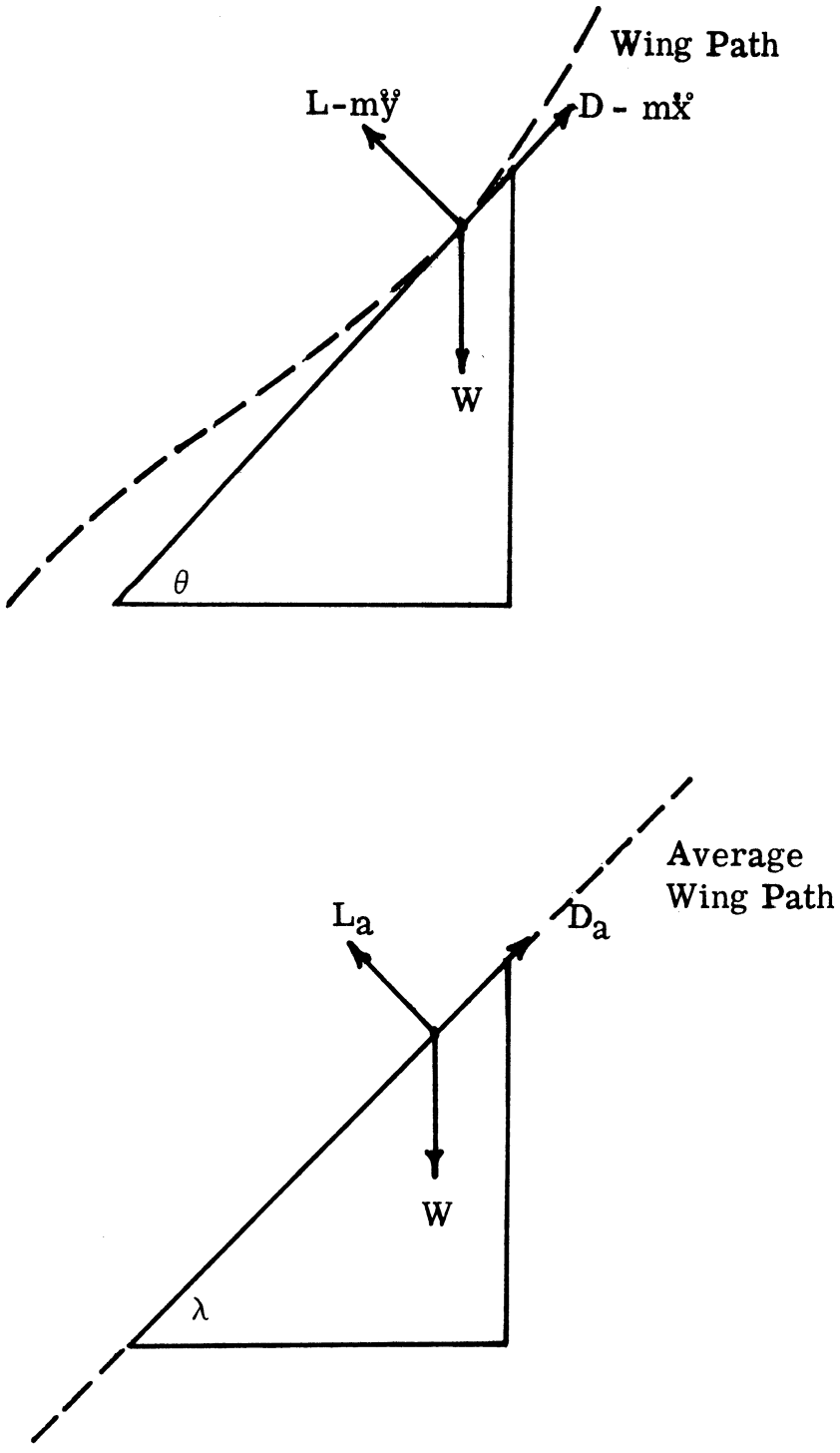

Figure 45. Forces Acting on a Falling Autorotating Wing.

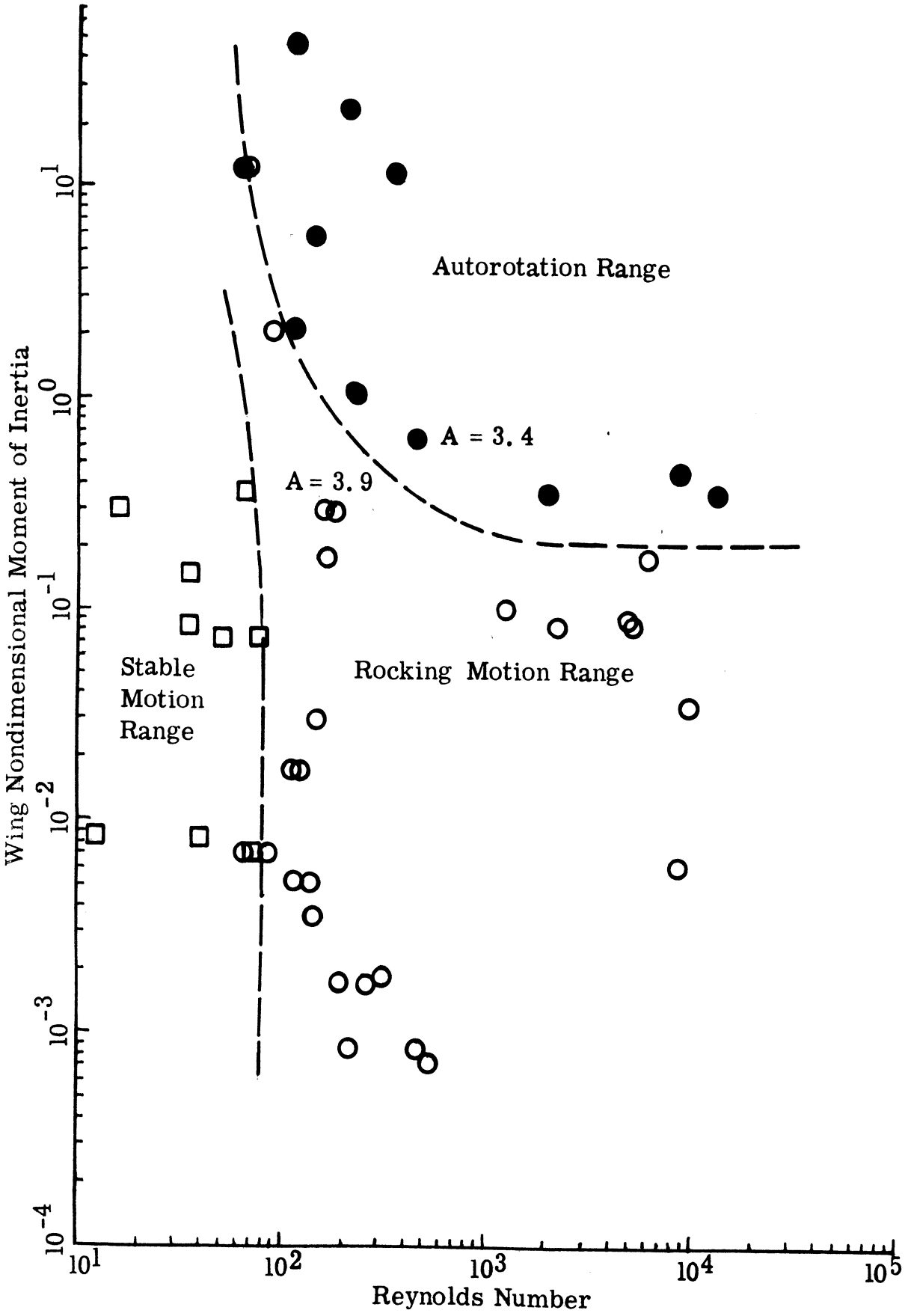

Figure 46. Range of I* and Reynolds Number for Various Types of Motion of a Falling Wing.

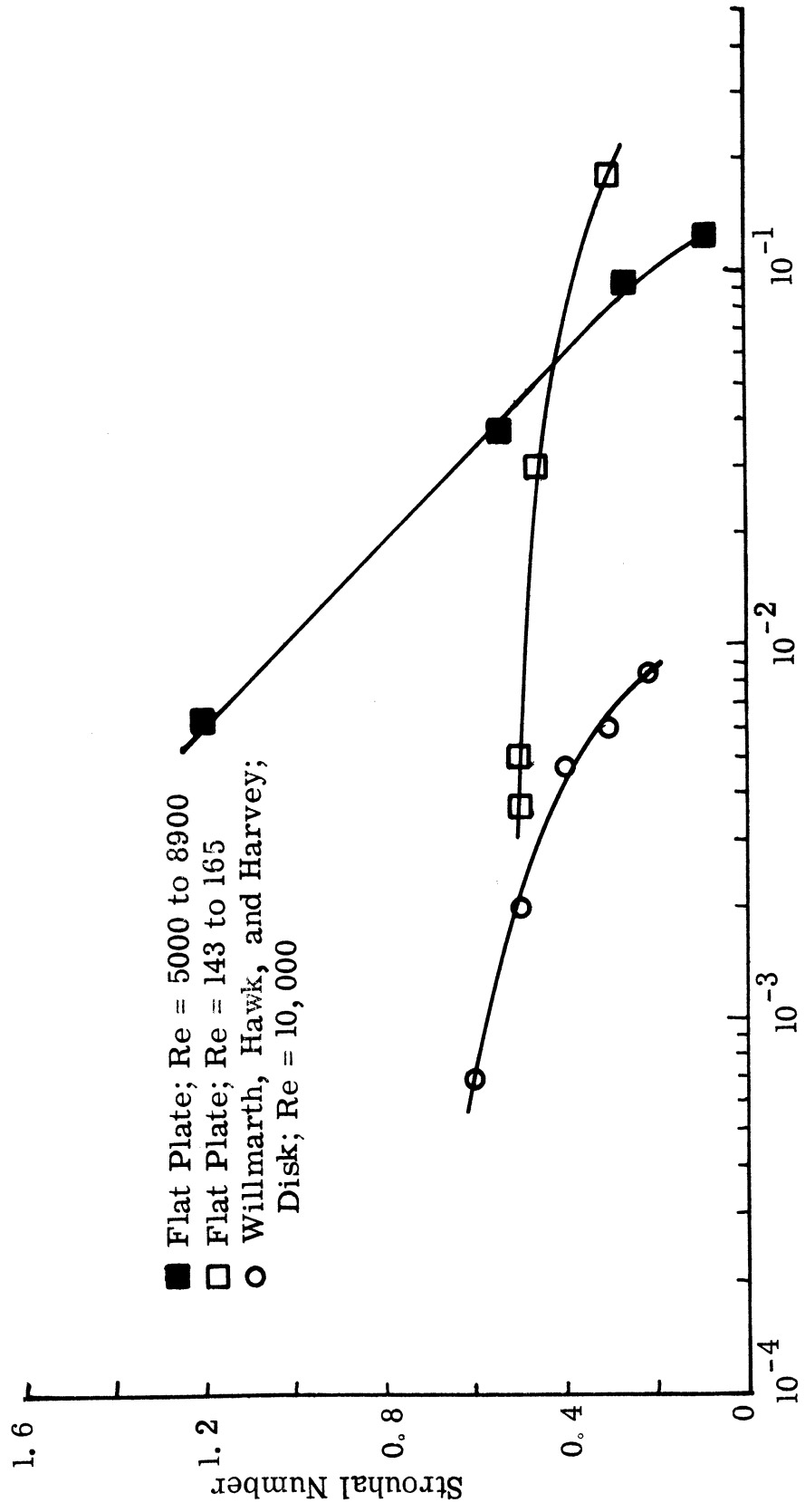

Figure 47. Strouhal Number vs I* for Falling Wing in Rocking Motion.

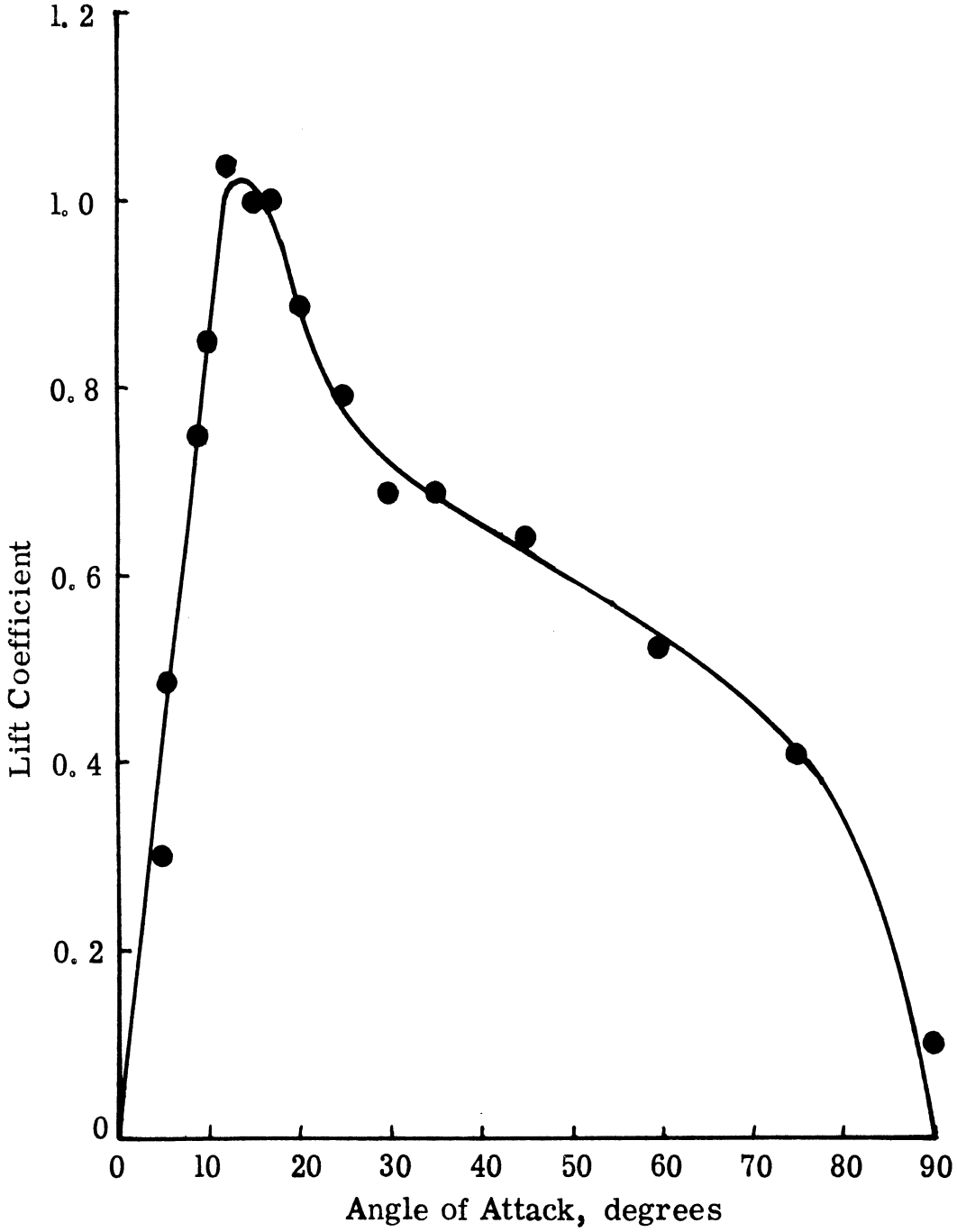

Figure 48. Static Lift Coefficient for 15% Thick Elliptical Airfoil at Re = 83,000.

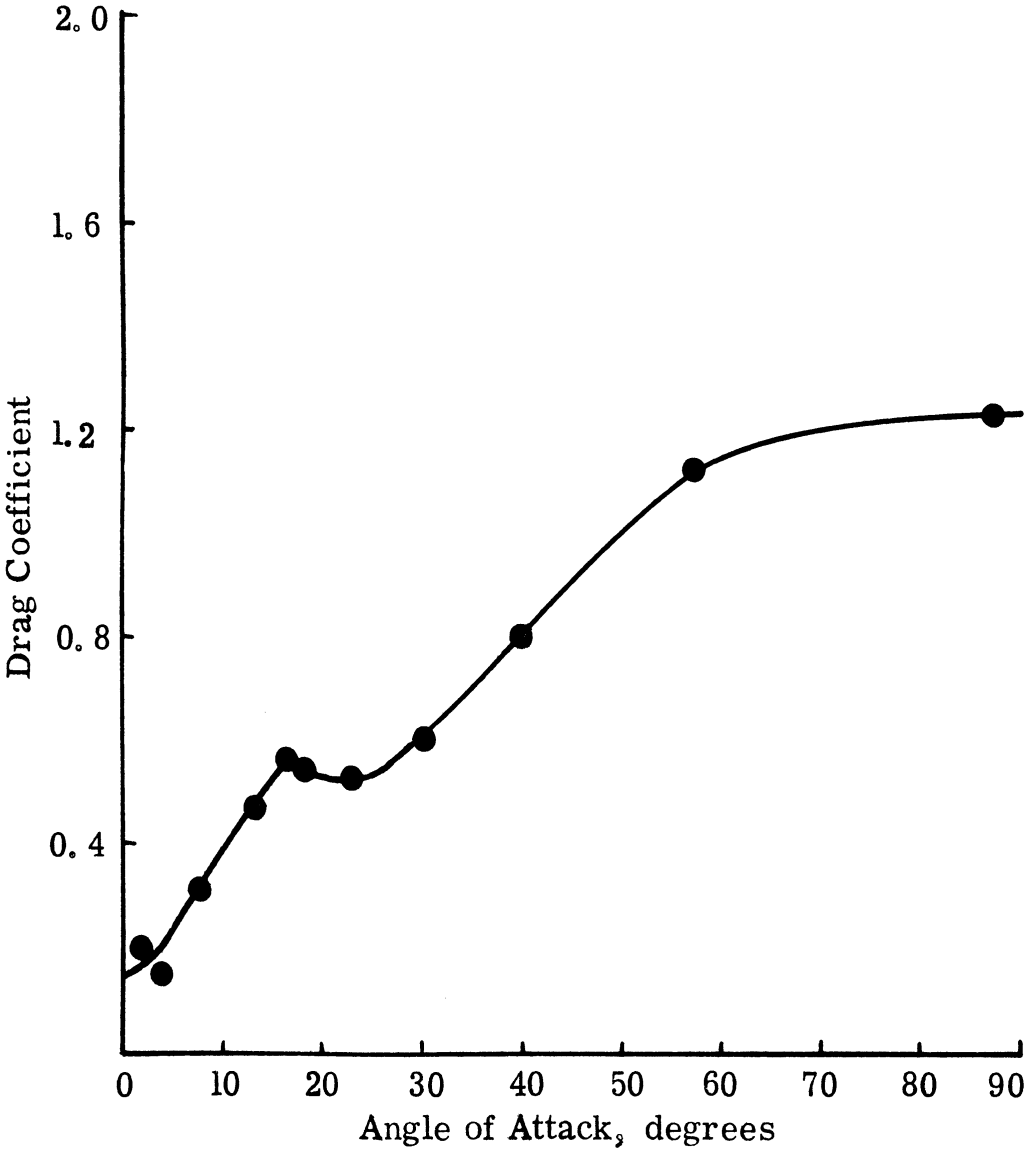

Figure 49. Static Drag Coefficient for 15% Thick Elliptical Airfoil at Re = 83,000.

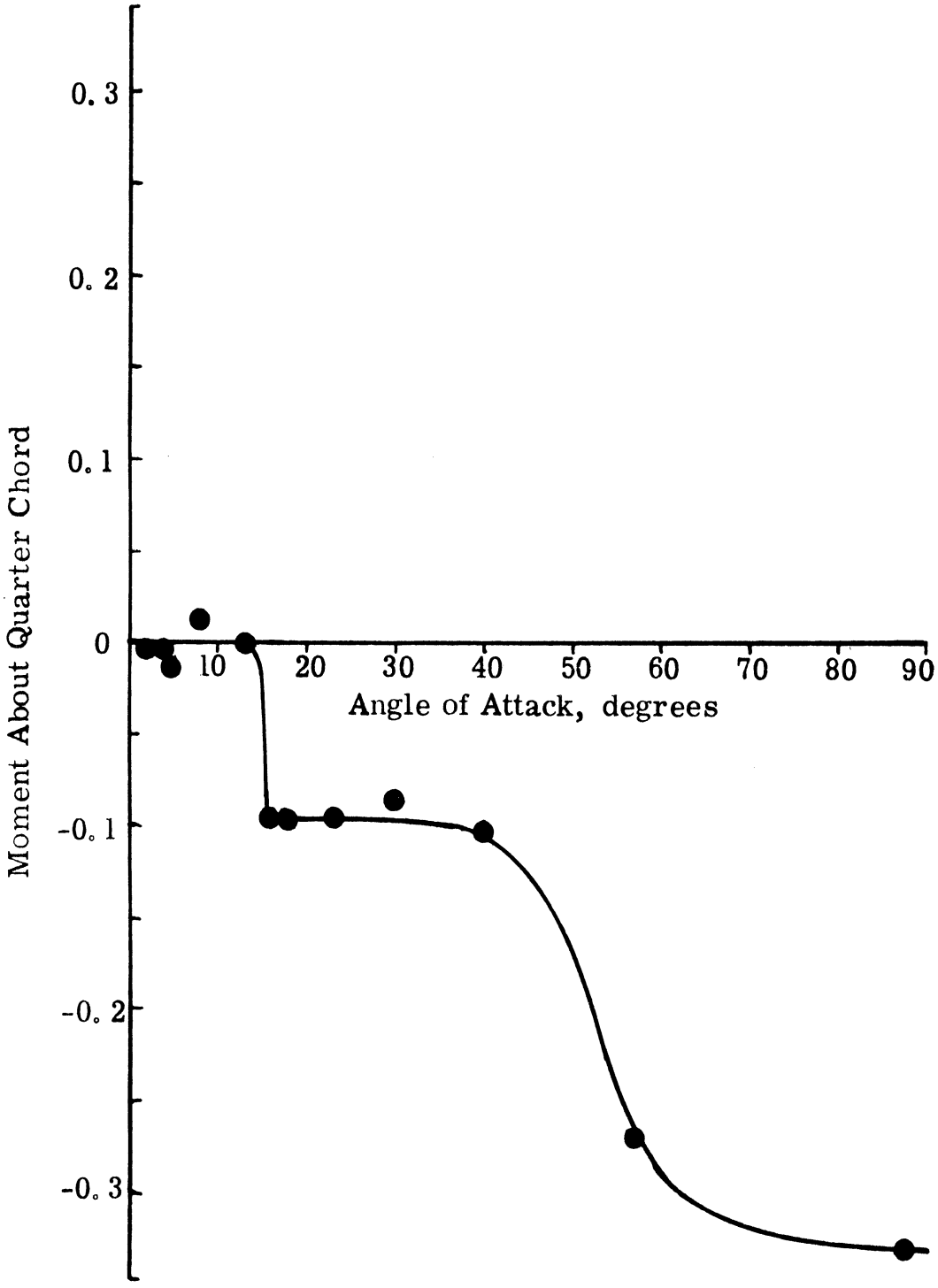

Figure 50. Static Pitching Moment for 15% Thick Elliptical Airfoil at Re = 83,000.

Unclassified

Security Classification

DOCUMENT CONTROL DATA - R & D

(Security classification of title, body of abstract and indexing annotation must be entered when the overall report is classified)

1. ORIGINATING ACTIVITY (Corporate author)
Department of Aerospace Engineering
The University of Michigan
Ann Arbor, Michigan 48104

2a. REPORT SECURITY CLASSIFICATION
Unclassified

2b. GROUP

3. REPORT TITLE

Autorotating Wings: An Experimental Investigation

4. DESCRIPTIVE NOTES (Type of report and inclusive dates)
Interim Technical Report

5. AUTHOR(S) (First name, middle initial, last name)

Edmund H. Smith

6. REPORT DATE	7a. TOTAL NO. OF PAGES	7b. NO. OF REFS
July 1970	140	21

8a. CONTRACT NO.
DAHC0-4-68C-0027

b. PROJECT NO.
5590-E

c.

d.

9a. ORIGINATOR'S REPORT NUMBER(S)
01954-2-T

9b. OTHER REPORT NO(S) (Any other numbers that may be assigned this report)

10. DISTRIBUTION STATEMENT

Distribution of this document is unlimited.

11. SUPPLEMENTARY NOTES

12. SPONSORING MILITARY ACTIVITY
Department of the Army
U. S. Army Research Office—Durham
Durham, North Carolina

13. ABSTRACT

The autorotation of a flat plate about its spanwise axis was experimentally studied. Most of the work was done with a model mounted on air bearings in a wind tunnel. The flow pattern differed from that over a static wing. The wing did not stall until it was almost perpendicular to the free stream. At Re = 240,000, the maximum lift coefficient was 4.50, with an average value of 2.20, while the maximum drag coefficient was 4.30 with an average value of 1.60. The angular acceleration was small; the wing rotated at an almost constant angular velocity. The wing nondimensional rotation rate approached an asymptotic limit at 0.35. Applying a driving torque to the wing increased the lift and drag, while a retarding torque reduced them. A variety of wing configurations were tested, with no major changes in the autorotation phenomenon. Freely falling wings were studied and behaved in a manner similar to the fixed axis wings for comparable Reynolds numbers.

DD FORM 1 NOV 68 1473

Unclassified

Security Classification

14. KEY WORDS	LINK A		LINK B		LINK C	
	ROLE	WT	ROLE	WT	ROLE	WT
Tumbling airfoil						
Unsteady aerodynamics						
Dynamic stall						